

IDEA League

MASTER OF SCIENCE IN APPLIED GEOPHYSICS
RESEARCH THESIS

**Measurements and numerical
simulations of the effects of inclination
and height of a GPR antenna above
ground**

Tobias Jakob Ganther

September 17, 2021

Measurements and numerical simulations of the effects of inclination and height of a GPR antenna above ground

MASTER OF SCIENCE THESIS

for the degree of Master of Science in Applied Geophysics
by

Tobias Jakob Ganther

September 17, 2021

IDEA LEAGUE
JOINT MASTER'S IN APPLIED GEOPHYSICS

Delft University of Technology, The Netherlands
ETH Zürich, Switzerland
RWTH Aachen, Germany

Dated: *September 17, 2021*

Supervisor(s):

Prof. Dr. Florian Wagner, Dr. Jan Igel

Dr. Norbert Klitzsch, M.Sc. Sam Stadler

Committee Members:

Prof. Dr. Florian Wagner, Dr. Jan Igel

Dr. Norbert Klitzsch, M.Sc. Sam Stadler

Associate Professor Gerrit Blacquière, PhD

Eidesstattliche Versicherung

Ganther, Tobias Jakob
Name, Vorname

354742
Matrikelnummer (freiwillige Angabe)

Ich versichere hiermit an Eides Statt, dass ich die vorliegende Arbeit/Bachelorarbeit/
Masterarbeit* mit dem Titel

Measurements and numerical simulations of the effects of inclination and height of a
GPR antenna above ground

selbstständig und ohne unzulässige fremde Hilfe erbracht habe. Ich habe keine anderen als die angegebenen Quellen und Hilfsmittel benutzt. Für den Fall, dass die Arbeit zusätzlich auf einem Datenträger eingereicht wird, erkläre ich, dass die schriftliche und die elektronische Form vollständig übereinstimmen. Die Arbeit hat in gleicher oder ähnlicher Form noch keiner Prüfungsbehörde vorgelegen.

Aachen, 17.09.2021

Ort, Datum

Unterschrift

*Nichtzutreffendes bitte streichen

Belehrung:

§ 156 StGB: Falsche Versicherung an Eides Statt

Wer vor einer zur Abnahme einer Versicherung an Eides Statt zuständigen Behörde eine solche Versicherung falsch abgibt oder unter Berufung auf eine solche Versicherung falsch aussagt, wird mit Freiheitsstrafe bis zu drei Jahren oder mit Geldstrafe bestraft.

§ 161 StGB: Fahrlässiger Falscheid; fahrlässige falsche Versicherung an Eides Statt

(1) Wenn eine der in den §§ 154 bis 156 bezeichneten Handlungen aus Fahrlässigkeit begangen worden ist, so tritt Freiheitsstrafe bis zu einem Jahr oder Geldstrafe ein.

(2) Straflosigkeit tritt ein, wenn der Täter die falsche Angabe rechtzeitig berichtigt. Die Vorschriften des § 158 Abs. 2 und 3 gelten entsprechend.

Die vorstehende Belehrung habe ich zur Kenntnis genommen:

Aachen, 17.09.2021
Ort, Datum

Unterschrift

Abstract

Landmines and Improvised Explosive Devices (IEDs) are among the most dangerous weapons found in (former) conflict areas. Many of them have only minimal or even no metal built in making it difficult to detect such devices via conventional metal detectors. Thus, alternative methods such as Ground Penetrating Radar (GPR) are deployed for this purpose. The field methodology of using GPR for the detection of buried objects generally includes varying degrees of inclination and height of the antenna in use. In this work, the influence of antenna inclination and height above ground is studied by using control studies with simple reflector geometries. The investigations shall provide more insights on the influence of these factors via measurements in controlled environments and numerical simulations. A comparison of the two is used to study the accuracy of numerical simulations of scenarios involving the detection of buried objects with GPR. The motivation hereby is the fact that gaining experimental data is generally very costly, time consuming and difficult to set up. Evaluations of the tested parameters showed the individual impact of each factor on the measured data. Height and inclination as well as exogenous factors, such as antenna orientation, subsurface structure and reflector geometry played a governing role influencing the measured data. The field measurements were successfully reproduced in numerical simulations. However, it is crucial to implement proper physical and geometrical parameters of the antenna, subsurface and reflector into the simulation environment to achieve realistic and reliable results. The findings of this thesis will be beneficial to implement more accurate numerical simulations in the future, which enables to study more complex, extensive and variable scenarios in a much faster, efficient and less costly manner.

Acknowledgements

First of all I would like to express my deepest gratitude towards my supervisor from LIAG Hannover, Sam Stadler. Through our long and extensive Skype conversations you guided me to the right direction and gave me valuable insights into the theoretical and practical aspects of my research. It was really pleasant working with you. I also thank Stephan Schennen for helping me with the setup of the inclined *gprMax* models that I used for my research. Furthermore, I thank Norbert Klitzsch and Professor Florian Wagner from RWTH Aachen for their continuous support and constructive feedback during our meetings and the institutes scientific discussions.

I am also grateful to all my friends and co-students who supported me throughout my studies in Delft, Zürich, and Aachen. Pursuing and finishing this Master program would not have been possible without them. Special thanks goes to Eddy Revelo Obando, who was always up for some bottles of beer, even during the darkest phases of the pandemic. I also thank Kuba, Eddy, Anna, Clara, Mathis for giving me valuable advises about academic writing.

Another special thanks goes to my former roommates and now friends Frank, Sarven and Tarik with whom I spent most of my time at ETH. They were always up for interesting conversations and of course some drinks when the geophysicists were 'busy' studying. I also thank my friends from Aachener Burschenschaft Teutonia and Hannoversche Burschenschaft Arminia for providing me shelter during my thesis. Without you, the already quite stressful time would have been even worse and especially even more lonely.

Moreover, I would like to thank my family. I very much appreciate the extensive support from my parents, my sister Minh, and my brother in law Felix. They always encouraged me, even during my lowest points. Last but not least, I would like to thank Ling Yan for our non-geophysical meetings and the time we spent together. You reminded me that there is also a life outside COVID-19 and geophysics.

Table of Contents

Abstract	vii
Acknowledgements	ix
Acronyms	xxi
1 Introduction	1
1-1 Explosive Ordnance, a global Problem	1
1-2 Geophysics in Explosive Ordnance Detection	2
1-3 Research Aim	3
2 Theoretical Background	5
2-1 Relevant Physical Properties	5
2-1-1 Magnetic Permeability	5
2-1-2 Electrical Conductivity	6
2-1-3 Dielectric Permittivity	6
2-2 Electrodynamics	8
2-2-1 Maxwell's Equations	8
2-2-2 EM Wave Velocity in Dielectric Media	8
2-2-3 Electromagnetic Wave Equation	9
2-2-4 Refraction of Electromagnetic Waves	12
2-3 Radiation Patterns	13
2-3-1 The Hertzian Dipole	13
2-3-2 Analytical Solutions of a Horizontally orientated Hertzian Dipole	13
2-4 The Finite Difference Time Domain (FDTD) Method	16
2-4-1 Basics of the FDTD Method	16
2-4-2 The Yee Algorithm	17
2-4-3 Numerical Stability and Dispersion	18
2-4-4 Absorbing Boundary Conditions and Perfectly Matched Layers	20

3 Methodology	21
3-1 Ground Penetrating Radar (GPR)	21
3-1-1 General Principle	21
3-1-2 Influencing Factors	23
3-1-3 GPR Data Processing	25
3-2 gprMax	26
3-2-1 General Information	26
3-2-2 gprMax Input Files and Modelling Setup	26
4 Field and Modelling Data Collection	29
4-1 Field Data Collection	29
4-1-1 Air Measurements	29
4-1-2 Measurements on Sand	31
4-2 gprMax Modelling Data Collection	32
4-2-1 Radiation Patterns	32
4-2-2 Air Measurements	34
4-2-3 Sand Measurements	34
5 Results and Discussion	37
5-1 Radiation Patterns	37
5-1-1 Far-Field Investigation	37
5-1-2 Hertzian Dipole Analytical Solutions	39
5-1-3 Hertzian Dipole: Comparison between Analytical and Numerical Solutions	41
Full Space	41
Half Space	41
5-1-4 Antenna Radiation Patterns	43
Full Space	43
Half Space	44
5-1-5 Influence of Subsurface	44
5-1-6 Influence of Elevation	45
5-2 Air Measurements	47
5-2-1 Part 1: Movement of the Reflector	47
5-2-2 Part 2: Effect of Antenna Inclination	48
5-3 Sand Measurements	49
5-3-1 Part 1: Horizontal Measurements at various Elevations	49
Main Features	49
Influence of Antenna Orientation	51
Influence of Antenna Elevation	53
5-3-2 Part 2: Measurements at various Inclinations	55
Influence of Inclination Angle	55
Influence of Inclination Direction	55

6 Conclusion and Outlook	59
Bibliography	61
A Additional Radiation Patterns	67
A-1 Far Field Patterns	67
A-2 Hertzian Dipole Patterns	69
A-3 Antenna Patterns	70
B Additional Radargrams	71
B-1 Horizontal Measurements	71
B-2 Inclination Measurements	73
C Envelope Plots	77
D Cross-Correlation Plots	81
E Field Setup and Data Processing	87
E-1 ReflexW Processing Flowchart	87
E-2 Photos of Field Measurements	88
F Additional Facts about Explosive Devises	89
F-1 Unexploded Ordnance (UXO) and Explosive Remnants of War (ERW)	89
F-2 Landmines	89
F-3 Improvised Explosive Devices (IED)	91

List of Figures

1-1	Annual Landmine and ERW related casualties between 1999 and 2018 [ICBL-CMC, 2019].	2
2-1	An Electromagnetic Wave consisting of electric and magnetic oscillating fields [Tesfamariam, 2013].	11
2-2	Left: Refraction at the interface between two media of different Refractive Indices, Right: Critical Refraction.	13
2-3	Left: E-Plane and H-Plane of a horizontal Hertzian Dipole oriented along the Y-axis after [Diamanti and Annan, 2013], right: Coordinate system for the geometry of an antenna over interface [Smith, 1984].	14
2-4	Single FDTD Yee cell showing electric (red) and magnetic (green) field components [Warren et al., 2016].	19
2-5	Sketch of the Leap-Frog time integration scheme [Wu et al., 2018].	19
3-1	Diagram of the setup for a GPR survey [GeoSci, 2018b].	22
3-2	Left: Common offset mode, Right: Common midpoint (CMP) mode [Meng et al., 2019].	23
3-3	GPR antenna orientations, after [Porsani et al., 2010].	23
3-4	Raypath signals measured by a receiver for a 2-layer Earth: 1 = Air Wave; 2 = Direct Wave; 3 = Reflected Wave; 4 = Air Refracted Wave [GeoSci, 2018b]. . .	24
3-5	Minimal example of a <i>gprMax</i> input script for a 3D model of a buried cylinder buried in a half space and the implementation of a 1.5GHz GSSI antenna.	27
4-1	Bowtie GSSI antenna [Warren, 2009].	30
4-2	Foamed Polystyrene measurement setup, Left: Reflector moved, Right: Inclinations changed.	30
4-3	Measurement setup of the measurements on sand.	31
4-4	Sketch of the radiation rattern's measurement setup.	33
4-5	FDTD mesh of geometry of a GSSI 1.5 GHz antenna [Warren, 2009].	34

4-6	Sketch of the air measurements, Left: Reflector moved horizontally, Right: Reflector moved in constant radius.	35
4-7	Sketch of the horizontal sand measurement <i>gprMax</i> modelling Setups Left: No elevation, Right: With elevation.	35
4-8	Sketch of the inclined <i>gprMax</i> sand measurements. Left: Inline, Right: Crossline.	36
5-1	Antenna radiation patterns for far-field investigations in full space.	38
5-2	Antenna radiation patterns for far-field investigations in half space.	38
5-3	Analytical solutions at $h = 0$ cm for different ϵ_r values.	39
5-4	Analytical solutions at $\epsilon_r = 4$ for different heights h (top: 2 cm, middle: 7 cm, bottom: 15 cm).	40
5-5	Radiation Patterns of the Hertzian Dipole in full space.	41
5-6	Radiation patterns of the Hertzian Dipole on a half space, $\epsilon_r = 4$	42
5-7	Radiation patterns of the Hertzian Dipole on a half space, $\epsilon_r = 16$	42
5-8	H-Plane radiation patterns of the 2D TM (left) and 3D TEM Model (right).	43
5-9	Radiation patterns of the 1.5 GHz GSSI antenna in full space.	44
5-10	Radiation patterns of the 1.5 GHz GSSI antenna for $\epsilon_r = 4$ and $\epsilon_r = 16$ ($h = 0$).	45
5-11	Radiation patterns of the Hertzian Dipole for $\epsilon_r = 4$ and $\epsilon_r = 16$ ($h = 0$).	45
5-12	Radiation patterns of the Hertzian Dipole at various elevations (2, 7 and 15cm).	46
5-13	Radiation patterns of the antenna at various elevations (2, 7 and 15 cm).	46
5-14	Radargrams where the reflector was shifted, Left: Field data, Right: Synthetic data.	47
5-15	Polar plots showing amplitudes at various inclinations from field and synthetic data.	48
5-16	Field data radrogram showing main features.	50
5-17	Envelopes of synthetic (left) and field data (right) of the horizontal Broadside-Perpendicular measurements ($h = 0$ cm).	51
5-18	Broadside-Perpendicular (left) and Parallel (right), $h = 0$ cm, field data.	52
5-19	Broadside-Perpendicular (left) and Parallel (right), $h = 0$ cm , synthetic data.	52
5-20	Field data of horizontal measurements at 0 cm (left) and 13 cm (right).	54
5-21	Field data of the 30° inclination measurements, Left: Inline, Right: Crossline.	56
5-22	Envelopes of the 30° Inline measurements (Broadside-Perpendicular), Left: Field data, Right: Synthetic data.	56
5-23	Envelopes of the 30° Crossline Measurements (Broadside-Perpendicular), Left: Field data, Right: Synthetic data.	57
A-1	Antenna radiation patterns for far-field investigations in half space ($\epsilon_r = 16$).	67
A-2	Antenna radiation patterns for far-field investigations in half space (top: $\epsilon_r = 1$, middle: $\epsilon_r = 4$, bottom: $\epsilon_r = 16$).	68
A-3	Hertzian Dipole (elevated), $\epsilon_r = 16$ (top: 2 cm, middle: 7 cm, bottom: 15 cm).	69
A-4	Antenna patterns (elevated), $\epsilon_r = 16$ (top: 2 cm, middle: 7 cm, bottom: 15 cm).	70
B-1	Broadside-Perpendicular (left) and Parallel (right), $h = 8$ cm, field data.	71

B-2	Broadside-Perpendicular (left) and Parallel (right), $h = 8$ cm, synthetic data.	71
B-3	Broadside-Perpendicular (left) and Parallel (right), $h = 13$ cm, field data.	72
B-4	Broadside-Perpendicular (left) and Parallel (right), $h = 13$ cm, synthetic data.	72
B-5	Broadside-Perpendicular (left) and Parallel (right), 15° , Crossline, field data.	73
B-6	Broadside-Perpendicular (left) and Parallel (right), 15° , Crossline, synthetic data.	73
B-7	Broadside-Perpendicular (left) and Parallel (right), 30° , Crossline, field data.	74
B-8	Broadside-Perpendicular (left) and Parallel (right), 30° , Crossline, synthetic data.	74
B-9	Broadside-Perpendicular (left) and Parallel (right), 15° , Inline, field data.	75
B-10	Broadside-Perpendicular (left) and Parallel (right), 15° , Inline, synthetic data.	75
B-11	Broadside-Perpendicular (left) and Parallel (right), 30° , Inline, field data.	76
B-12	Broadside-Perpendicular (left) and Parallel (right), 30° , Inline, synthetic data.	76
C-1	Envelopes of field (left) and synthetic data (right) of the horizontal Broadside-Parallel measurements ($h = 0$ cm).	77
C-2	Envelopes of field (left) and synthetic data (right) of the horizontal Broadside-Perpendicular measurements ($h = 8$ cm).	77
C-3	Envelopes of field (left) and synthetic data (right) of the horizontal Broadside-Parallel measurements ($h = 8$ cm).	78
C-4	Envelopes of field (left) and synthetic data (right) of the horizontal Broadside-Perpendicular measurements ($h = 13$ cm).	78
C-5	Envelopes of field (left) and synthetic data (right) of the horizontal Broadside-Parallel measurements ($h = 13$ cm).	78
C-6	Envelopes of the 15° Inline measurements (Broadside-Perpendicular), Left: Field data, Right: Synthetic data.	79
C-7	Envelopes of the 15° Inline measurements (Broadside-Parallel), Left: Field data, Right: Synthetic data.	79
C-8	Envelopes of the 30° Inline measurements (Broadside-Parallel), Left: Field data, Right: Synthetic data.	79
C-9	Envelopes of the 15° Crossline measurements (Broadside-Perpendicular), Left: Field data, Right: Synthetic data.	80
C-10	Envelopes of the 15° Crossline measurements (Broadside-Parallel), Left: Field data, Right: Synthetic data.	80
C-11	Envelopes of the 30° Crossline measurements (Broadside-Parallel), Left: Field data, Right: Synthetic data.	80
D-1	Cross-Correlations, horizontal measurement ($h = 0$ cm), Broadside-Perpendicular, Left: Field data, Right: Synthetic data.	81
D-2	Cross-Correlations, horizontal Measurement ($h = 0$ cm), Broadside-Parallel, Left: Field data, Right: Synthetic data.	81
D-3	Cross-Correlations, horizontal measurement ($h = 8$ cm), Broadside-Perpendicular, Left: Field data, Right: Synthetic data.	82
D-4	Cross-Correlations, horizontal measurement ($h = 8$ cm), Broadside-Parallel, Left: Field data, Right: Synthetic data.	82

D-5	Cross-Correlations, horizontal measurement ($h = 13 \text{ cm}$), Broadside-Perpendicular, Left: Field data, Right: Synthetic data.	82
D-6	Cross-Correlations, horizontal measurement ($h = 13 \text{ cm}$), Broadside-Parallel, Left: Field data, Right: Synthetic data.	83
D-7	Cross-Correlation, Inclination: 15° Inline, Broadside-Perpendicular, Left: Field data, Right: Synthetic data.	83
D-8	Cross-Correlation, Inclination: 15° Inline, Broadside-Parallel, Left: Field data, Right: Synthetic data.	83
D-9	Cross-Correlation, Inclination: 30° Inline, Broadside-Perpendicular, Left: Field data, Right: Synthetic data.	84
D-10	Cross-Correlation, Inclination: 30° Inline, Broadside-Parallel, Left: Field data, Right: Synthetic data.	84
D-11	Cross-Correlation, Inclination: 15° Crossline, Broadside-Perpendicular, Left: Field data, Right: Synthetic data.	84
D-12	Cross-Correlation, Inclination: 15° Crossline, Broadside-Parallel, Left: Field data, Right: Synthetic data.	85
D-13	Cross-Correlation, Inclination: 30° Crossline, Broadside-Perpendicular, Left: Field data, Right: Synthetic data.	85
D-14	Cross-Correlation, Inclination: 30° Crossline, Broadside-Parallel, Left: Field data, Right: Synthetic data.	85
E-1	Flowchart of the general GPR data processing steps for field and synthetic data.	87
E-2	Photo of the air measurements field setup.	88
E-3	Photo of the air measurements field setup.	88
F-1	Explosive Remnants of War in post revolution Libya [Foounen, 2018].	90
F-1	Left: Yugoslavian PMA-2 landmine with low metal content [LIAG, 2013], Right: Chinese Type 59 anti-tank mine [Smith, 2007].	90
F-2	Typical metallic and non-metallic Improvised Explosive Devices (IEDs) [LIAG, 2021]	91

List of Tables

2-1	Typical Magnetic Permeability and Electrical Conductivity values of commonly used metals [BSSA, 2021, Chung, 2001, Okman, 2005, O'Neill, 2017, Muhammad and Umar, 2013, Walsh, 1991].	6
2-2	Typical ϵ_r , velocity and penetration depth values for rocks and other geologically relevant materials [GeoSci, 2018c].	9
4-1	Listing of the inclined measurements (Inline = Inclination parallel to measurement direction, Crossline = Inclination perpendicular to measurement direction).	31
4-2	Listing of the horizontal measurements.	32
4-3	Radiation pattern model parameters.	33
4-4	Model parameters of the <i>gprMax</i> simulations on sand.	36
5-1	Amplitude proportions between antenna orientations for horizontal measurements.	52
5-2	Amplitude proportions between antenna elevations for horizontal measurements.	53
5-3	Summarized results of the horizontal and elevation measurements.	54
5-4	Summarized results of the inclination measurements.	57

Acronyms

ICBL-CMC International Campaign to Ban Landmines – Cluster Munition Coalition

ERW Explosive Remnants of War

EMI Electromagnetic Induction

GPR Ground Penetrating Radar

FDTD Finite Difference Time Domain

EOD Explosive Ordnance Disposal

IED Improvised Explosive Device

UXO Unexploded Ordnance

TNT Trinitrotoluol

VTK Visualization ToolKit

LIAG Leibniz Institute for Applied Geophysics

EM Electromagnetic

IEEE Institute of Electrical and Electronics Engineers

CFL Courant Friedrich Lewy

ABC Absorbing Boundary Condition

PML Perfectly Matched Layer

Tx Transmitter Antenna

Rx Receiver Antenna

CMP Common Midpoint

DC Direct Current

TE Transverse Electric

TM Transverse Magnetic

TEM Transverse Electromagnetic

CFS Complex Frequency Shifted

Chapter 1

Introduction

1-1 Explosive Ordnance, a global Problem

In modern warfare, the extensive use of explosives has become very common in most conflict regions. Since the invention of explosive materials such as gunpowder and Trinitrotoluol ([TNT](#)), the array of explosive weapons has been extended continuously ranging from grenades, bombs and shells to landmines and even nuclear weapons [[Kovac, 2001](#)]. During and after conflicts, problems arise from undetonated explosives. All types of explosives which failed to detonate during combat are summarized under the term Unexploded Ordnance ([UXO](#)). Furthermore, the term Explosive Remnants of War ([ERW](#)) includes [UXO](#) and abandoned explosive ordnance [[ICBL-CMC, 2020](#)]. In addition to [ERW](#), landmines and so-called [IEDs](#) pose the major threat to the health and safety of the local population. Moreover, serious economical problems arise from the limitation of land used caused by the contamination with explosives [[Cirillo et al., 2001](#), [Kara and Gebrehiwot, 2009](#)]. Depending on the weapons used during wars, the composition of explosive ordnance varies significantly.

Landmines and [IEDs](#) are the most dangerous types of explosives which are often found in conflict areas. Both, landmines and [IEDs](#) are commonly deployed near the surface. They are responsible for most casualties inflicted in (former) conflict areas where civilians represent the majority of casualties. More details about landmines and [IEDs](#) can be found in Chapter F. Since 1999, the annual casualties are monitored by the International Campaign to Ban Landmines – Cluster Munition Coalition ([ICBL-CMC](#)). Figure 1-1 shows the annual casualty number related to landmines (including [IEDs](#)) and [ERW](#). Between 1999 and 2018 the annual casualty number related to landmines exceeded at least 3400 people worldwide [[ICBL-CMC, 2019](#)]. Thus, it becomes evident that contaminated areas need to be cleared of every type of explosive ordnance to minimize the risk of human and material casualties.

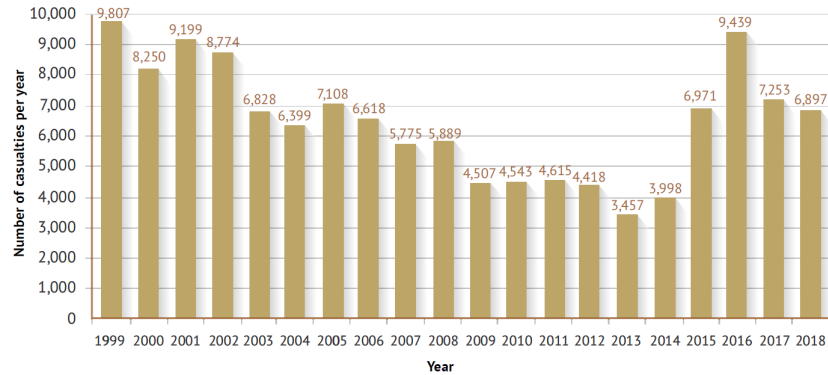


Figure 1-1: Annual Landmine and ERW related casualties between 1999 and 2018 [ICBL-CMC, 2019].

1-2 Geophysics in Explosive Ordnance Detection

Various geophysical techniques are used in the detection of landmines, IEDs and ERW. Frequently used techniques are the magnetic method, Electromagnetic Induction (EMI) and Ground Penetrating Radar (GPR). The magnetic method is a relatively easy and inexpensive tool to apply for subsurface exploration tasks involving horizontal magnetic property variations. These variations cause anomalies in the Earth's normal magnetic field that can be mapped [Knödel et al., 2007]. The method is a widely applied method in the identification of aircraft bombs from WWII (on- and offshore). However, the magnetic method is not susceptible to non-ferrous targets [Billings, 2004]. Therefore, non-ferrous ordnance, such as plastic landmines and IEDs cannot be detected. This fact severely limits the applicability of the magnetic method.

In EMI, a transmitter coil induces a time varying primary magnetic field which in response induces Eddy Currents in conductive targets. Subsequently, the Eddy Currents produce a secondary magnetic field which is measured by a receiver coil. EMI measurements can be performed in the time domain or in the frequency domain. The time domain method uses a finite pulse primary field which is subsequently shut down and a induced secondary field is measured. The field's rate of decay contains the relevant information about the subsurface [Knödel et al., 2007]. Frequency domain EMI uses a periodic continuous signal which is permanently measured by the receiver coil. The measured amplitude and phase provide the relevant information [Pasion, 2007]. Both methods are used in the detection of UXO, landmines and IEDs. Standard metal detectors, which are used in landmine and Improvised Explosive Device (IED) detection, work according to the principle of EMI [Guelle et al., 2003]. However, EMI based detectors can only measure a signal if the target of interest contains sufficient amount of metallic elements. But as previously mentioned, many explosive devices are made of minimally or even non-metallic materials and are therefore not detectable via metal detectors. Moreover, metal detectors measure metallic object which are often not related to explosives. This leads to a high number of false alarms, especially in urban environments [Cirillo et al., 2001].

Lastly, GPR is used for explosive ordnance detection [Takahashi et al., 2011, Brunzell, 1999, Cirillo et al., 2001]. In GPR, radar pulses are emitted to image the subsurface and identify

contrasts in electrical properties. The measured signals which are in time domain can be used to determine velocity variations of reflected and transmitted electromagnetic waves. Subsequently, an image of the subsurface with real depths can be attained based on a subsurface velocity model via migration. Such images in the time domain as well as with real spatial extension after migration can be used for landmine and IED detection.

The major drawback of GPR is its strong wave attenuation in the ground, especially in clay rich soils. GPR signals are attenuated by Intrinsic (absorption) and scattering attenuation. Intrinsic attenuation depends on the measured frequencies as well as the soil's dielectric and electric parameters. It is one major governing factor influencing the sensing depth and image resolution of GPR [Loewer et al., 2015]. Scattering attenuation is caused by non-uniformities yielding a deviation of GPR waves from its original trajectory. Scattering attenuation is governed by the wavelength of the signal and the size of the scatter object. Therefore, the use of GPR is mostly confined to shallow subsurface investigations [Knödel et al., 2007]. However, most landmines and IEDs are buried within the first 20 cm of soil [ICBLC-MC, 2020] which is well in range of GPR. Furthermore, GPR is capable of detecting explosives with low to no metal content because GPR identifies contrast in the electric and dielectric properties which are not necessarily related to the presence of metal. [Cirillo et al., 2001]. The geophysical technique is therefore a major research topic for the detection of explosive ordnance in the shallow subsurface as a promising alternative to EMI and magnetic measurements. In landmine and IED detection for humanitarian and military Explosive Ordnance Disposal (EOD) operations in (former) conflict areas, GPR plays a major role [Takahashi et al., 2011].

1-3 Research Aim

Because of the wide array of problems related to the presence of explosive ordnance, there is a need for time- and cost-efficient methods to clear contaminated areas from, landmines, IEDs and ERW. The cost of landmine and IED clearing is very high compared to its production [Kara and Gebrehiwot, 2009]. The established methods used in landmine and IED detection (mostly EMI-based) struggle to detect explosives with low metal content. Their reliance on the presence of metals make these methods very inefficient [Das, 2006]. Therefore, novel methods need to be introduced and established. The problem of the increasing use of low metal content explosives has led to an increased use of GPR sensors which do not rely on the presence of metal [Daniels, 2006]. However, GPR signatures vary depending on soil composition, the explosive device's material, its geometry and position in the subsurface [Lopera and Milisavljevic, 2007, Takahashi et al., 2011]. In addition, the GPR system in use is relevant as well. The Counter-IED project series, which is run by the Leibniz Institute for Applied Geophysics (LIAG), aims to determine these unknown dependencies in the detection of buried explosive devices. This thesis is part of the Counter-IED III project, whose main research focuses (among others) on the influence of antenna coupling to the subsurface.

Moreover, numerical simulations are becoming increasingly relevant for GPR detection. They are required to study the behaviour of systems where no analytical solutions are provided due to their complexity, e.g., a GPR antenna. Numerical modelling yields the advantage that direct field measurements are not required making it possible to produce realistic synthetic GPR data for various scenarios in an efficient and cost-effective manner. However, the applied

model requires proper input data about the environment which ought to be investigated to produce realistic results.

There are various software available for simulating electromagnetic wave propagation. One of these is the state-of-the-art Finite Difference Time Domain (**FDTD**) based open source software *gprMax*. It was originally developed in 1996 by Antonis Giannopoulos when **FDTD** modelling of **GPR** was still in the fledgling stages. In 2015 Craig Warren re-developed *gprMax* from scratch resulting in the software in its current state. Giannopoulos and Warren continue to work on, and supervise ongoing developments to *gprMax*. Moreover, *gprMax* functions as a platform for the development and implementation of various user libraries serving various purposes such as 3D antenna models, antenna patterns or parameters for various materials. [Stadler and Igel, 2018] for example developed a 3D antenna model for the 400MHz GSSI antenna. A 3D model for the 1.5 GHz GSSI antenna was also continuously developed and improved as shown in [Warren and Giannopoulos, 2011] and [Giannakis et al., 2019]. Not only the development of *gprMax* is still ongoing but also the development of various user libraries which makes *gprMax* a highly reliable and versatile modelling tool for **GPR** simulations.

It is known that the radiation characteristics of antennas are important for the detectability of a buried object [Warren, 2009]. By increasing the elevation, the directivity increases. Changing inclinations also affects radiation characteristics. These effects affect the investigations negatively. This thesis focuses on the investigations of varying degrees of inclination and heights of the antenna in use. These factors are common practical aspects of using **GPR** to detect shallowly buried explosives. This is for instance a result of safety precautions or the effect of vegetation and surface topography. However, studies about the detectability of buried objects via **GPR** generally do not include these two factors. This thesis shall provide more insights on the influence of antenna inclination and height via measurements in controlled environments and numerical simulations. A comparison of the two is used to study the accuracy of numerical simulations of scenarios involving the detection of buried objects with **GPR**. The motivation hereby is the fact that gaining experimental data is generally very costly, time consuming and difficult to set up. Assuring accurate numerical simulations will provide the future option to study complex, extensive and variable scenarios in a much faster, efficient and less costly manner.

This thesis is composed of two main research foci. The first part focuses on the investigation of radiation characteristics. To study radiation characteristics, far-field investigations are carried out. Numerical *gprMax* simulations are performed over half spaces whose media have varying electrical and dielectric properties. As sources, an infinitesimal Hertzian Dipole and a 1.5 GHz GSSI antenna model are used to identify variations between both sources. Furthermore, the height of the sources above the interface is varied to investigate their impact on the radiation patterns. The simulation's results are subsequently compared to analytical solutions. In the second part of the thesis, the influence of varying degrees of inclination is investigated. Measurements were performed in two antenna configurations, namely Broadside-Parallel and Broadside-Perpendicular configuration. The antennas were aligned horizontally as well as in multiple angles of inclination. Moreover, the antenna was inclined parallel and perpendicular to the measurement direction. Lastly, measurements were performed with varying antenna elevation above ground. The field measurement's models were implemented into *gprMax*. The results acquired by *gprMax* simulations are subsequently compared to the field measurements quantitatively and qualitatively.

Chapter 2

Theoretical Background

In this Chapter, all for this work relevant theoretical background information are provided. In the first Section 2-1, relevant physical properties are introduced which need to be addressed in both, analytical solutions and the modelling setup. Subsequently, in Section 2-2 the relevant physical principles of electromagnetism are introduced, namely the Maxwell's equations, the Electromagnetic Wave Equation and Snell's law. After that, in Section 2-3, the fundamentals of antenna radiation patterns are described and analytical solutions for antenna patterns on and above an interface provided. Lastly, the main principles of the FDTD method are introduced in Section 2-4.

2-1 Relevant Physical Properties

The magnetic permeability, electrical conductivity and dielectric permittivity are the main governing factors for electromagnetic wave propagation. Typical values for geological materials as well as materials used in explosive devices are given in Table 2-1 and Table 2-2. The aforementioned properties are explained in more detail in the following Sections below.

2-1-1 Magnetic Permeability

The magnetic permeability μ [H/m] is a property that describes how the magnetization of a material is affected by an external magnetic field applied to it. The magnetic permeability is often represented as relative permeability μ_r [-] which is the ratio between the permeability of a specific medium μ and the permeability of free space [Olhoeft, 1998]:

$$\mu_r = \frac{\mu}{\mu_0}, \quad (2-1)$$

where μ_0 represents the magnetic permeability in free space which is $\approx 4\pi \cdot 10^{-7}$ H/m.

Ferromagnetic materials with $\mu_r \gg 1$, have significant influence on the Electromagnetic (EM) wave propagation and attenuation [Jol, 2009]. The magnetic permeability of most materials found in the earth's crust can be assumed as ≈ 1 and have little influence on GPR performance [Olhoeft, 2003]. Even metals such as austenitic stainless steel, the most common steel alloy [ISSF, 2021] is not ferromagnetic and has a relative permeability of ≈ 1 [BSSA, 2021]. Also copper, which is a common material used in landmines and IEDs in form of cables is not ferromagnetic. Therefore, it can be assumed that the magnetic permeability is mostly a major constant factor in GPR surveys. In Table 2-1, the relative permeabilities of commonly found materials are provided.

Table 2-1: Typical Magnetic Permeability and Electrical Conductivity values of commonly used metals [BSSA, 2021, Chung, 2001, Okman, 2005, O'Neill, 2017, Muhammad and Umar, 2013, Walsh, 1991].

Material	σ [S/m]	μ_r [-]
Aluminium	35×10^6	1
Copper	60×10^6	1
Lead	5.3×10^6	1
Tin	8.7×10^6	1
Brass	15.9×10^6	1
Austenitic Stainless Steel	1.5×10^6	1
Carbon Stainless Steel	7×10^6	100
Iron	10.1×10^6	5000

2-1-2 Electrical Conductivity

The electrical conductivity σ [S/m] quantifies to what extent a material is capable of inducing a current when it is applied to an electrical field [Daniels, 2004]. There are high variations for different materials commonly found in the subsurface. Typical conductivity values for geological targets are in the range between 0.01 mS/m and 1 S/m [GeoSci, 2018c].

In GPR surveys, the electrical conductivity is a governing factor in the attenuation of EM waves. In media with higher electrical conductivities, EM waves tend to attenuate faster [Olhoeft, 2003]. Therefore, in GPR surveys one must take into account that the expected depth of penetration decreases in clay and water rich environments where electrical conductivity is expected to increase.

2-1-3 Dielectric Permittivity

The dielectric permittivity ϵ [F/m] is a physical property which characterizes the degree of electrical polarization a material experiences under the influence of an external electric field. It is defined as the ratio between the electric field E [V/m] within a material and the corresponding electric displacement D [C/m²] [Olhoeft, 1998], [GeoSci, 2018a]:

$$\epsilon = \frac{D}{E}. \quad (2-2)$$

The extent of the separation of the electrical charges within a material is represented by the electric polarization P [C/m²] yielding the following equation:

$$D = \epsilon_0 E + P, \quad (2-3)$$

where ϵ_0 represents the permittivity of free space which is $\approx 8.85 \cdot 10^{-12}$ F/m. When exposed to an electric field, bounded electrical charges of opposing sign will try to separate from one another [GeoSci, 2018a].

Permittivity is commonly expressed in the form of relative permittivity. The relative permittivity, ϵ_r [-] is the ratio of its absolute permittivity ϵ [F/m] to that of free space ϵ_0 [F/m]:

$$\epsilon_r = \frac{\epsilon}{\epsilon_0}. \quad (2-4)$$

Fully described, relative permittivity ϵ_r [-] is defined as the frequency-dependent complex permittivity with real and imaginary components [Daniels, 2004]:

$$\epsilon_r = \epsilon'_r - j\epsilon''_r, \quad (2-5)$$

where ϵ'_r [-] and ϵ''_r [-] are the real and imaginary parts of the permittivity, respectively.

The real part ϵ'_r is also known as the storage component. It is a measure of the ability of the medium to be polarized under an electric field. The complex part ϵ''_r is a measure related to losses of the material associated with the electrical conductivity σ [S/m] and the frequency f [1/s] [Daniels, 2004].

The losses in a material are described as phase angle difference between D and E . The magnitude of loss of a material is commonly quantified in terms of the value of its dissipation factor (or loss tangent):

$$\tan \theta = \frac{\epsilon''_r}{\epsilon'_r}, \quad (2-6)$$

where θ denotes the phase angle between D and E . This value is high for lossy, conductive materials [Chen et al., 2004].

Although the permittivity of a material shows dependency on f and σ , it has been shown that commonly found subsurface materials with very low σ and typically higher GPR frequencies (in the range of higher MHz to lower GHz) show only little variations in permittivity [Daniels, 2004]. The solid constituents of most commonly found soils and anthropogenic materials have an ϵ_r between 2 and 9. The measured values of ϵ_r for soils and building materials lie mostly in the range between 4 and 40 [Jol, 2009, Takahashi et al., 2011, Daniels, 2004]. However, the range of permittivity of subsurface materials can vary heavily. For example, the presence of water is a major governing factor influencing permittivity. Fluids contribute the majority of a formations σ due to solved ions commonly present in water [Olhoeft, 2003]. Typical permittivities of geologic materials are shown in Table 2-2.

2-2 Electrodynamics

GPR involves the propagation of EM waves, thus being part of EM methods. This Section aims to introduce the fundamentals of electrodynamics and their physical laws which are relevant for GPR. This Section is not designated to provide a complete derivation of all equations and relationships. More detailed descriptions are provided in the referenced literature.

2-2-1 Maxwell's Equations

GPR makes use of electromagnetic waves which are described by the Maxwell's equations. They are first order partial differential equations which express the relations between the fundamental electromagnetic field quantities and their dependence on their sources [Glisson, 1989]:

$$\text{Maxwell-Faraday equation: } \nabla \times E = -\frac{\partial B}{\partial t}, \quad (2-7)$$

$$\text{Ampère's law: } \nabla \times H = \frac{\partial D}{\partial t} + J_c + J_s, \quad (2-8)$$

$$\text{Gauss's law for magnetism: } \nabla \cdot B = 0, \quad (2-9)$$

$$\text{Gauss's law for Electric Fields: } \nabla \cdot D = q_v, \quad (2-10)$$

where t is time [s], q_v the volume electric charge density [C/m^3], J_c the critical current density [A/m^2], J_s the surface current density [A/m], E the electric field strength [V/m], H the magnetic field strength [A/m], D the Electric Displacement [C/m^2] and B the Magnetic Flux Density [T]. $\nabla \times$ represents the curl differential operator while $\nabla \cdot$ represents the divergence differential operator.

In Maxwell's equations, the field vectors are assumed to be single-valued bounded, and continuous functions of position and time. The Maxwell-Faraday equation states that a time-varying magnetic field induces a spatially-varying, non-conservative electric field. Ampère's law states that electric currents and changing electric fields lead to a circulating magnetic field. Gauss's law for magnetic fields states that the total magnetic flux leaving a closed surface must equal zero while according to Gauss's law for electric fields, the total electric flux leaving a closed surface is proportional to the charge enclosed by the surface.

2-2-2 EM Wave Velocity in Dielectric Media

The propagation of EM waves is governed by the major physical parameters which were introduced in Section 2-1. In free space, an EM wave travels at the speed of light c :

$$c = \sqrt{\frac{1}{\mu_0 \epsilon_0}}. \quad (2-11)$$

The dielectric permittivity of a material governs the velocity of propagation of EM waves through the medium. The propagation velocity v within a dielectric material is as follows [Olhoeft, 1998]:

$$v = \sqrt{\frac{1}{\mu\epsilon}}, \quad (2-12)$$

where ϵ represents the dielectric permittivity [F/m] and μ the magnetic permeability [H/m] of the medium.

Moreover, eq. 2-12 can be rewritten in terms of the speed of light c [m/s], μ_r [-] and ϵ_r [-]:

$$v = \sqrt{\frac{c}{\mu_r\epsilon_r}}. \quad (2-13)$$

However, μ_r is constant for most subsurface media and can therefore be set at $\mu_r = 1$ for low loss media. Therefore, the relative dielectric permittivity ϵ_r is the primary diagnostic physical property in GPR surveys as already pointed out in Section 2-1. Typical EM velocity values for common geological materials are shown in Table 2-2 below.

Table 2-2: Typical ϵ_r , velocity and penetration depth values for rocks and other geologically relevant materials [GeoSci, 2018c].

Material	ϵ_r [-]	Velocity [m/ns]	Penetration Depth [m]
Air	1	0.3	∞
Fresh Water	80	0.033	285
Sea Water	80	0.01	< 0.1
Ice	3 - 4	0.16	3000
Dry Sand	3 - 5	0.15	3200
Saturated Sand	20-30	0.06	145
Limestone	4 - 8	0.12	30
Shales	5 - 15	0.09	1
Silts	5 - 30	0.07	1.3
Clays	5 - 40	0.06	0.2
Granite	4 - 6	0.13	65
Anhydrite	3 - 4	0.13	55

2-2-3 Electromagnetic Wave Equation

The Maxwell equations describe the relation between the electric and the magnetic field. The equations are coupled. However, the equations can be decoupled by raising their order. This leads to an uncoupled partial differential equation of second order, the Electromagnetic Wave Equation [Balanis, 1989]. The Electromagnetic Wave Equation is commonly used for the description of waves as they occur in GPR. It is imperative to have a basic knowledge of wave characteristics for the application of GPR.

Firstly, Gauss's law for electric fields and Ampère's law can alternatively be expressed in terms of B and E . The alternate expressions in eq. 2-14 and 2-15 are equivalent to the expressions in eq. 2-8 and 2-10:

$$\text{Ampère's law: } \nabla \times B = \mu(J + \epsilon \frac{\partial E}{\partial t}), \quad (2-14)$$

$$\text{Gauss's law for Electric Fields: } \nabla \cdot E = \frac{\rho}{\epsilon}, \quad (2-15)$$

where E [V/m] is the electric field strength, B [T] the magnetic flux density, J [C/m³] the charge density, ρ [A/m²] is the current density, ϵ [F/m] is the dielectric permittivity, and μ [H/m] is the magnetic permeability of the medium.

In the following part of this Section, the derivation of the 3D Wave Equation from Maxwell's Equations is shown. It can be assumed that there are no free charges or currents. Thus, according to this assumption, $\rho = 0$ and $J = 0$. This assumption simplifies eq. (2-14) and (2-15) to:

$$\nabla \times B = \mu\epsilon \frac{\partial E}{\partial t}, \quad (2-16)$$

$$\nabla \cdot E = 0. \quad (2-17)$$

After this simplification, the curl operator $\nabla \times$ of eq. (2-7) is solved and the order of differentiation on the right-hand side changed:

$$\nabla \times [\nabla \times E] = -\frac{\partial}{\partial t}[\nabla \times B]. \quad (2-18)$$

In the following operation, eq. (2-14) is inserted substituting $\nabla \times B$:

$$\nabla \times [\nabla \times E] = -\frac{\partial}{\partial t}[\mu\epsilon \frac{\partial E}{\partial t}] = -\mu\epsilon \frac{\partial^2 E}{\partial t^2}. \quad (2-19)$$

Now, the left hand side of eq. (2-19) can be rewritten according to the mathematical fact that for a vector field, the curl of the curl vector identity is defined by:

$$\nabla \times [\nabla \times V] = \nabla[\nabla \cdot V] - \nabla^2 V, \quad (2-20)$$

which yields the rewritten form of eq. (2-19):

$$\nabla[\nabla \cdot E] - \nabla^2 E = -\mu\epsilon \frac{\partial^2 E}{\partial t^2}. \quad (2-21)$$

In a final step, the acquired equation can be simplified by the previously made assumption that no free charges are present (see eq. 2-17) which yields the final wave equation in 3D:

$$\nabla^2 E = \mu\epsilon \frac{\partial^2 E}{\partial t^2}. \quad (2-22)$$

A wave equation for the magnetic field, can also be derived using a very similar approach. The result has the same form:

$$\nabla^2 B = \mu\epsilon \frac{\partial^2 B}{\partial t^2}. \quad (2-23)$$

Lastly, permittivity and permeability can be replaced by the wave velocity v_{ph} according to the relation given in eq. (2-12). Now, the final equations for the electromagnetic wave equation for the electric and magnetic field are acquired:

$$[v_{ph}^2 \nabla^2 - \frac{\partial^2}{\partial t^2}]E = 0, \quad (2-24)$$

$$[v_{ph}^2 \nabla^2 - \frac{\partial^2}{\partial t^2}]B = 0. \quad (2-25)$$

The derived wave equations show that time-varying electric and magnetic field (Figure 2-1) induce each other. Moreover, both fields are always perpendicular. **EM** waves propagate linearly through a medium until they meet the interface between two media. They are characterized by their wavelength λ [m] and frequency f [1/s].

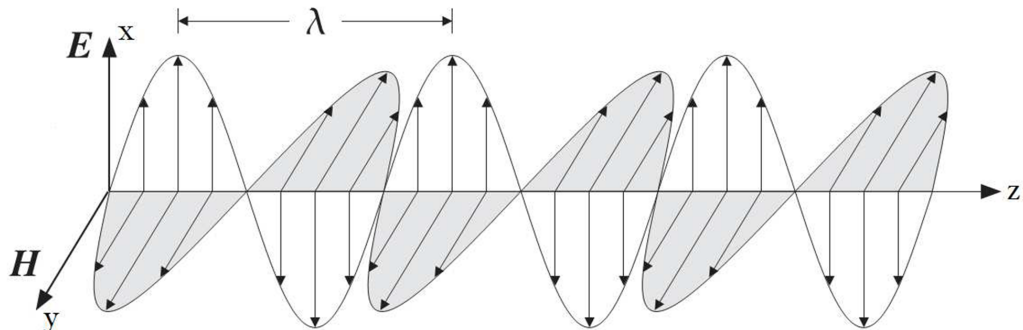


Figure 2-1: An Electromagnetic Wave consisting of electric and magnetic oscillating fields [Tefamariam, 2013].

Moreover, the frequency f [1/s] and wavelength λ [m] are connected to the **EM** wave's velocity v [m/s] as follows [Olhoeft, 1998]:

$$v = \lambda f. \quad (2-26)$$

At an interface, **EM** waves can be reflected, refracted or scattered. The aforementioned factors λ , f and v are the major governing factors regarding the reflection and refraction of electromagnetic waves at interfaces as shown in the following Section.

2-2-4 Refraction of Electromagnetic Waves

When an **EM** wave meets the interface of two media with different electrical properties, a portion of its energy is scattered back and the rest is transmitted into the lower medium. Understanding the geometrical principles of **EM** wave propagation is relevant to describe **EM** wave behaviour at interfaces with different (di-) electrical properties. Figure 2-2 shows the geometrical relations on the interface of two media. The angles of incident θ_1 and θ_2 are related to the velocities v_1 [m/s] and v_2 [m/s] and refraction indices n_1 [-] and n_2 [-] by Snell's Law [Annan, 2009]:

$$\frac{\sin \theta_1}{\sin \theta_2} = \frac{v_2}{v_1} = \frac{n_1}{n_2}. \quad (2-27)$$

Reflections parallel to the interface are called critical reflection. The critical angle θ_{crit} can be calculated via *Snell's Law* by using the refraction indices of the media:

$$\sin \theta_{crit} = \frac{n_2}{n_1}, \quad (2-28)$$

where a refraction index n [-] can be described as the factor between the speed of light c [m/s] and the **EM** Waves velocity v [m/s] in the respective media:

$$n = \frac{c}{v}. \quad (2-29)$$

Furthermore, n can be expressed by using the complex relative permittivity:

$$n = \sqrt{\epsilon_r} = \sqrt{\epsilon'_r - i\epsilon''_r}. \quad (2-30)$$

If a lossless medium is assumed, the refraction index is simply governed by the real part of the relative permittivity of both media. However, in most cases, an air-ground interface is assumed. Therefore as $n_{air} = 1$, the critical refraction angle θ_{crit} solely depends on the refraction index of the ground n_{ground} :

$$\theta_{crit} = \arcsin \frac{1}{n_{ground}}. \quad (2-31)$$

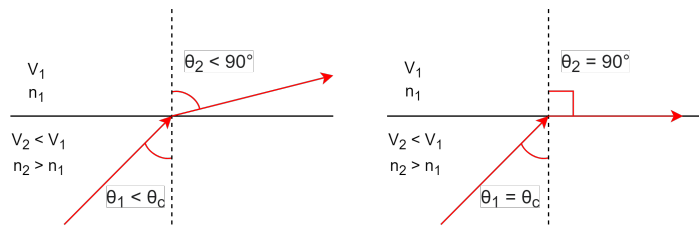


Figure 2-2: Left: Refraction at the interface between two media of different Refractive Indices, Right: Critical Refraction.

2-3 Radiation Patterns

In GPR, electromagnetic waves are produced by antennas which have, depending on their construction and the electrical and dielectric properties of surrounding environment, distinct variations of their radiation characteristics. In radiation patterns, the directional dependence of the strength of the electromagnetic waves radiating from the source is depicted. According to the Institute of Electrical and Electronics Engineers (IEEE) Standard Definitions of Terms for Antennas, a radiation pattern of an antenna is defined as the spatial distribution of an electromagnetic's field characterizing quantity that is generated by an antenna [IEEE, 1983]. The calculation and measurement of radiation patterns are mostly done at far distances where antennas are positioned far away from the receiver. Such fields are called far-fields and the resulting patterns are called far-field pattern. They are usually normalized to its maximum.

Radiation patterns determine how well a target can be detected. Therefore, the knowledge of radiation characteristics is crucial for the use of GPR. Improved results may be obtained in the application of GPR by taking radiation patterns into account. One of the most commonly used antenna models is the Hertzian Dipole. Moreover, analytical solutions of an Hertzian Dipole positioned on and above a material halfspace do exist. In the following Sections, the main qualities of the Hertzian Dipole as well as its analytical solutions are presented.

2-3-1 The Hertzian Dipole

The Hertzian Dipole is one of the simplest radiation sources used to describe radiation characteristics. It is a linear antenna whose length is assumed to be infinitesimally small. Therefore, it is much shorter than the wavelength in free space. As an infinitesimally small segment of a conductor, the dipole is carrying a radio-frequency current along its entire length [Greiner, 1998]. Due to its lack of spatial extent, the Hertzian Dipole is only a theoretical construction. The theoretical construction of a Hertzian Dipole can be used as the basis for analytical or numerical calculations.

2-3-2 Analytical Solutions of a Horizontally orientated Hertzian Dipole

Analytical solutions derived for infinitesimal dipoles are based on Maxwell's equations. In landmine and IED detection, antennas are held above the interface for safety reasons. Therefore, analytical solutions for horizontally orientated dipoles positioned above the interface are required. These solutions are derived in [Smith, 1984]. The field of a general antenna over

an half-space is expressed as a spectrum of plane waves. The integrals representing the field are evaluated asymptotically to obtain the far- or “geometrical optics” field of the antenna. This field is subsequently used to define quantities that describe the directive properties of the antenna including directivity [Smith, 1984].

First, the spherical polar coordinates for the dipole type antenna must be defined. For a horizontally orientated dipole antennas, the vertical plane containing the antenna is called E-Plane for the electric field and the vertical plane perpendicular to the antenna axis is called H-Plane for the magnetic field [Diamanti et al., 2012]. Figure 2-3 shows a typical dipole, the E- and H-Planes and the spherical polar angles θ and ϕ in the Cartesian coordinate system which is used for the following equations. Moreover, the coordinate reference system which is introduced to describe the location of a horizontal electric dipole on a dielectric half space as shown in Figure 2-3 also needs to take into account the position of the antenna above ground (see right side of Figure 2-3). In essence, two rectangular coordinate systems are used. A general antenna is located at a height h [m] above the planar interface separating the homogeneous material half spaces (Regions 1 and 2). Based on the offset between antenna and origin of the coordinate system, new polar angles θ' and ϕ' are introduced whose origin is located at the antenna center. Moreover, δ^+ [m] and δ^- [m] account for the vertical spatial extension of the antenna.

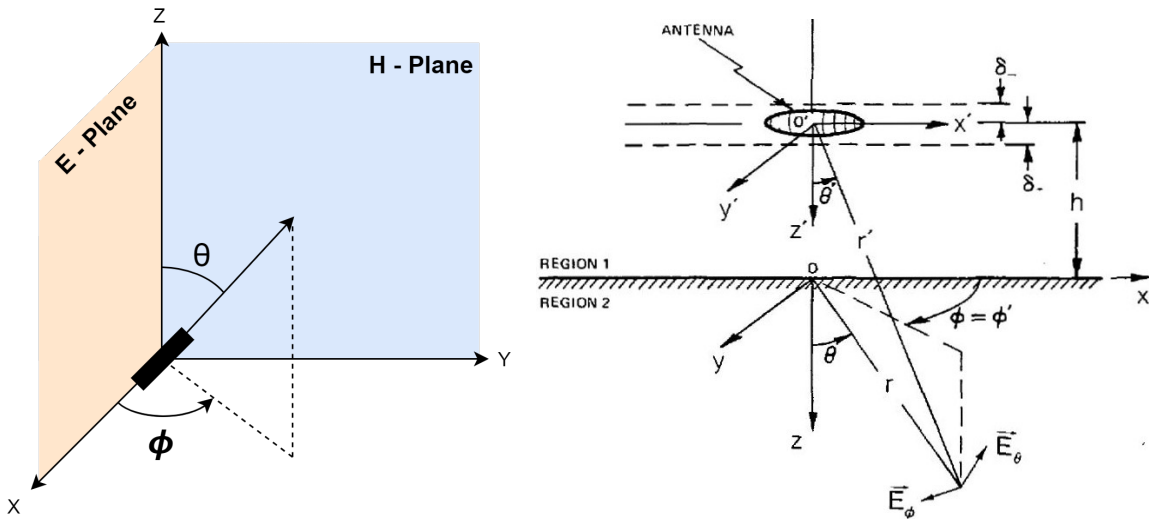


Figure 2-3: Left: E-Plane and H-Plane of a horizontal Hertzian Dipole oriented along the Y-axis after [Diamanti and Annan, 2013], right: Coordinate system for the geometry of an antenna over interface [Smith, 1984].

Analytical solutions of the E-field at different heights h above the interface depending on the elevation θ and azimuthal angle ϕ are:

$$E_{1\theta}^r = -\omega^2 \mu_0 p \sin \phi |\cos \theta| e^{jk_1 h |\cos \theta|} [1 - R_{\parallel}(K_{s1}) e^{-j2k_1 h |\cos \theta|}] e^{-jk_1 r} / 4\pi r, \quad (2-32)$$

$$E_{1\phi}^r = \omega^2 \mu_0 p \cos \phi e^{jk_1 h |\cos \theta|} [1 + R_{\perp}(K_{s1}) e^{-j2k_1 h |\cos \theta|}] e^{-jk_1 r} / 4\pi r, \quad (2-33)$$

$$E_{2\theta}^r = \omega^2 \mu_0 k_{21} p \sin \phi |\cos \theta| e^{-jk_1 h \sqrt{1-k_{21}^2 \sin^2 \theta}} T_{\parallel}(K_{s2}) e^{-jk_2 r} / 4\pi r, \quad (2-34)$$

$$E_{2\phi}^r = \omega^2 \mu_0 k_{21} p \cos \phi |\cos \theta| e^{-jk_1 h \sqrt{1-k_{21}^2 \sin^2 \theta}} T_{\perp}(K_{s2}) e^{-jk_2 r} / 4\pi r \sqrt{1 - k_{21}^2 \sin^2 \theta}, \quad (2-35)$$

where μ_0 [H/m] denotes the magnetic permeability in free space. The electric moment p [Cm] for an electrically short linear element of current I [A], length Δl [m] and radial frequency ω [rad/s] is approximately:

$$p = -\frac{jI\Delta l}{\omega}. \quad (2-36)$$

The reflection and transmission coefficients R_{\parallel} [-] and R_{\perp} [-], T_{\parallel} [-] and T_{\perp} [-] evaluated at the transverse propagation numbers K_{s1} and K_{s2} respectively, are the Fresnel coefficients:

$$R_{\parallel}(K_{s1}) = \frac{k_{21}^2 |\cos \theta| - \sqrt{k_{21}^2 - \sin^2 \theta}}{k_{21}^2 |\cos \theta| + \sqrt{k_{21}^2 - \sin^2 \theta}}, \quad (2-37)$$

$$R_{\perp}(K_{s1}) = \frac{|\cos \theta| - \sqrt{k_{21}^2 - \sin^2 \theta}}{|\cos \theta| + \sqrt{k_{21}^2 - \sin^2 \theta}}, \quad (2-38)$$

$$T_{\parallel}(K_{s2}) = \frac{2k_{12}\sqrt{k_{12}^2 - \sin^2 \theta}}{k_{12}^2 |\cos \theta| + \sqrt{k_{12}^2 - \sin^2 \theta}}, \quad (2-39)$$

$$T_{\perp}(K_{s2}) = \frac{2\sqrt{k_{12}^2 - \sin^2 \theta}}{|\cos \theta| + \sqrt{k_{12}^2 - \sin^2 \theta}}, \quad (2-40)$$

(2-41)

where k_{12} [-] is the quotient of the wavenumbers k_n [1/m] in the observed media n :

$$k_{12} = \frac{1}{k_{21}} = \frac{k_1}{k_2}. \quad (2-42)$$

The wavenumber of free space k_0 [1/m] equals the quotient of the radial frequency ω [rad/s] and the speed of light in free space c [m/s]. In medium 1, which is always air as upper half space, the wavenumber of free space can be assumed because the velocity of EM waves is approximately equal to the velocity in free space:

$$k_0 = k_1 = \frac{\omega}{c}. \quad (2-43)$$

In the second medium, which represents the subsurface, the relative permittivity ϵ_r [-] must be taken into account for the calculation of k_2 :

$$k_2 = k_0 \sqrt{\epsilon_r(\text{soil})}. \quad (2-44)$$

The E-field solutions need to be transformed into the Poynting vector for direct comparison between numerical and analytical solutions. The Poynting P^r [W/m²] vector represents the directional energy flux of an electromagnetic field [Poynting, 1884]. The E-field E_Θ [V/m] can be transformed into the Poynting vector by incorporating the impedances Z_n [Ω] of the respective medium [Poljak and Cvetković, 2019]:

$$P^r = \frac{E_\theta^2}{Z_n} \quad \text{where} \quad Z_n = \sqrt{\frac{\mu_n}{\epsilon_n}}. \quad (2-45)$$

The impedances Z_n are acquired via the medias permeability μ_n [H/m] and permittivity ϵ_n [F/m]. Thus, because μ_n is assumed to remain constant, only ϵ_n governs Z_n . Moreover, as illustrated in previous Sections, major governing factors such as v , λ and θ_{crit} directly depend on ϵ as well. Thus, ϵ is the major governing factor of the analytical solutions under the assumption of a lossless and magnetically constant subsurface.

2-4 The Finite Difference Time Domain (FDTD) Method

Numerical simulations are an important tool in the world of engineering and science. It allows testing and analyzing systems and designs without the need to perform physical experiments. Radiation characteristics of antennas for example include the realm of experiments. In the wide field of modelling methods, the FDTD method is one of the most established ones. Moreover, the FDTD method is one of the the most popular method for simulating the propagation of electromagnetic waves based on the full solution of Maxwell's equations making this method especially appealing for GPR applications. Furthermore, it is in general a major tool for a broad range of scientific and engineering applications. The main reason of the success of the FDTD method is its operational simplicity [Kunz and Luebbers, 1993]. The following Section aims to introduce the FDTD method and the aspects relevant to GPR simulations. The underlying theory and ideas are presented, as well as key elements such as boundary conditions. The FDTD based open source software *gprMax* developed by [Warren et al., 2016] is used for all numerical simulations performed in this thesis.

2-4-1 Basics of the FDTD Method

The FDTD approach for the numerical solution of Maxwell's equations is to discretize in both, space, and time. Therefore, to solve an electromagnetic problem in FDTD, the Maxwell equations are temporally and spatially discretized by using a grid which is composed of Yee cells [Yee, 1966]. FDTD produces results in the time domain, which can be transformed to the frequency domain via Fourier transformation. The whole frequency spectrum of an electromagnetic signal can be obtained with only one simulation [Lazzi et al., 1998].

The method, originated by Kane Yee in 1966, is based on the discretization of the partial derivatives in Maxwell's equations using central differencing [Giannopoulos, 2012]. A FDTD algorithm substitutes first and second order partial derivatives with finite difference approximations via the application of Taylor series expansion. The central difference approximation

provides an approximation for the value of the derivative at a point midway between, thus central to each adjoining pair of points in the data.

A Taylor series expansion of an arbitrary function f about the points $x \pm \Delta\frac{x}{2}$ is performed as shown below [Gedney, 2011]:

$$f(x + \frac{\delta x}{2}) = f(x) + \frac{\partial f(x)}{\partial x} \frac{\Delta x}{2} \frac{1}{1!} + \frac{\partial^2 f(x)}{\partial x^2} \left(\frac{\Delta x}{2}\right)^2 \frac{1}{2!} + \frac{\partial^3 f(x)}{\partial x^3} \left(\frac{\Delta x}{2}\right)^3 \frac{1}{3!} + \dots \quad (2-46)$$

$$f(x - \frac{\delta x}{2}) = f(x) - \frac{\partial f(x)}{\partial x} \frac{\Delta x}{2} \frac{1}{1!} + \frac{\partial^2 f(x)}{\partial x^2} \left(\frac{\Delta x}{2}\right)^2 \frac{1}{2!} - \frac{\partial^3 f(x)}{\partial x^3} \left(\frac{\Delta x}{2}\right)^3 \frac{1}{3!} + \dots \quad (2-47)$$

where Δx is assumed to be small. Subsequently, the two expansions are subtracted and the results normalized by Δx , leading to:

$$\frac{f(x + \frac{\delta x}{2}) - f(x - \frac{\delta x}{2})}{\Delta x} = \frac{\partial f(x)}{\partial x} + \Delta x^2 \frac{\partial^3 f(x)}{\partial x^3} \frac{1}{24} \dots \quad (2-48)$$

Note that the terms with even-order derivatives cancel. Rearranging terms, the first-order derivative with respect to x can be expressed as:

$$\frac{\partial f(x)}{\partial x} \approx \frac{f(x + \frac{\delta x}{2}) - f(x - \frac{\delta x}{2})}{\Delta x} + O(\Delta x^2). \quad (2-49)$$

This is the “central difference” approximation of the first-order derivative [Hildebrand, 1968]. The trailing term on the right hand side represents the leading order error in the approximation. The error will decay as x^2 with decreasing x . The approximation is thus said to be “second-order accurate” [Gedney, 2011]. Due to this second-order accuracy, this method gives a truncation error of second order which in conclusion provides a higher accuracy.

2-4-2 The Yee Algorithm

The Yee algorithm is the backbone of every FDTD software. It involves a robust representation of Maxwell’s equations by spatially and temporally sampling the electric and magnetic field vector components. [Yee, 1966] proposed spatially staggering the vector components of the E-field and H-field in a rectangular Cartesian coordinate system which results in the so-called Yee cell. A graphical illustration of a Yee cell for the 3D case is shown in Figure 2-4. The E-components are placed in the middle of the edges and the H-components in the center of the faces. Every E-component is surrounded by four circulating H-components, and vice versa. This Yee cell based scheme, has proven to be very robust, and builds the core of many FDTD softwares.

Moreover, the Yee algorithm applies a so-called leapfrog scheme in time domain. The general working principle is shown in Figure 2-5. For a particular time step the E-field is computed in the entire model space using the previously computed H-values. Then the H-values for

the current time step are computed to update the H-field based on the E-values that were previously computed. The entire process is repeated for the entire predefined amount of time steps. Leapfrog time stepping is fully explicit and employs central differences. The scheme has two major advantages. Firstly, the equations do not need to be run simultaneously. Secondly, the scheme yields a dissipation-free numerical wave propagation [Taflove and Brodwin, 1975].

Yee provides a direct solution for Maxwell's time dependent curl eq. 2-7 and 2-8. There is no need to explicitly enforce the Gaussian laws as they are a direct consequence of the aforementioned curl equations. Thus, the Electromagnetic Wave Equation does not need to be solved as well. In the end, using this approach means eq. 2-7 and 2-8 can be decomposed into six coupled, scalar partial differential equations which are the basis of the FDTD numerical algorithm for electromagnetic wave interactions with general 3D-objects [Yee, 1966]. These equations are subsequently discretized in both space and time and applied in each FDTD cell for the iterative leapfrog calculations of the E- and H-field [Warren, 2009]:

$$\frac{\partial E_x}{\partial t} = \frac{1}{\epsilon} \left(\frac{\partial H_z}{\partial y} - \frac{\partial H_y}{\partial z} - J_{sx} - \sigma E_x \right), \quad (2-50)$$

$$\frac{\partial E_y}{\partial t} = \frac{1}{\epsilon} \left(\frac{\partial H_x}{\partial z} - \frac{\partial H_z}{\partial x} - J_{sy} - \sigma E_y \right), \quad (2-51)$$

$$\frac{\partial E_z}{\partial t} = \frac{1}{\epsilon} \left(\frac{\partial H_y}{\partial x} - \frac{\partial H_x}{\partial y} - J_{sz} - \sigma E_z \right), \quad (2-52)$$

(2-53)

$$\frac{\partial H_x}{\partial t} = \frac{1}{\mu} \left(\frac{\partial E_y}{\partial z} - \frac{\partial E_z}{\partial y} - M_{sx} - \sigma^* H_x \right), \quad (2-54)$$

$$\frac{\partial H_y}{\partial t} = \frac{1}{\mu} \left(\frac{\partial E_z}{\partial x} - \frac{\partial E_x}{\partial z} - M_{sy} - \sigma^* H_y \right), \quad (2-55)$$

$$\frac{\partial H_z}{\partial t} = \frac{1}{\mu} \left(\frac{\partial E_x}{\partial y} - \frac{\partial E_y}{\partial x} - M_{sz} - \sigma^* H_z \right), \quad (2-56)$$

where σ^* denotes equivalent magnetic loss [Ω/m], σ [S/m] the electrical conductivity, M_s [V/m^2] impressed (source) magnetic current density and J_s [A/m^2] impressed (source) electric current density.

2-4-3 Numerical Stability and Dispersion

The spatial discretization is of utmost importance since a smaller discretization enables the FDTD model to achieve a more realistic representation of the modelled problem. Moreover, discretization steps are always finite since computational resources are limited. In conclusion, a FDTD model represents a discretized version of the real problem that is of limited size [Taflove, 1995].

Numerical stability describes a numerical solution that produces a bounded result given a bounded input [Taflove, 1995]. Stability is ensured in 3D when the spatial discretization steps Δx , Δy , Δz [m] and the time discretization Δt [s] are chosen to satisfy the Courant Friedrich Lewy (CFL) criterion [Yee, 1966, Warren et al., 2016]:

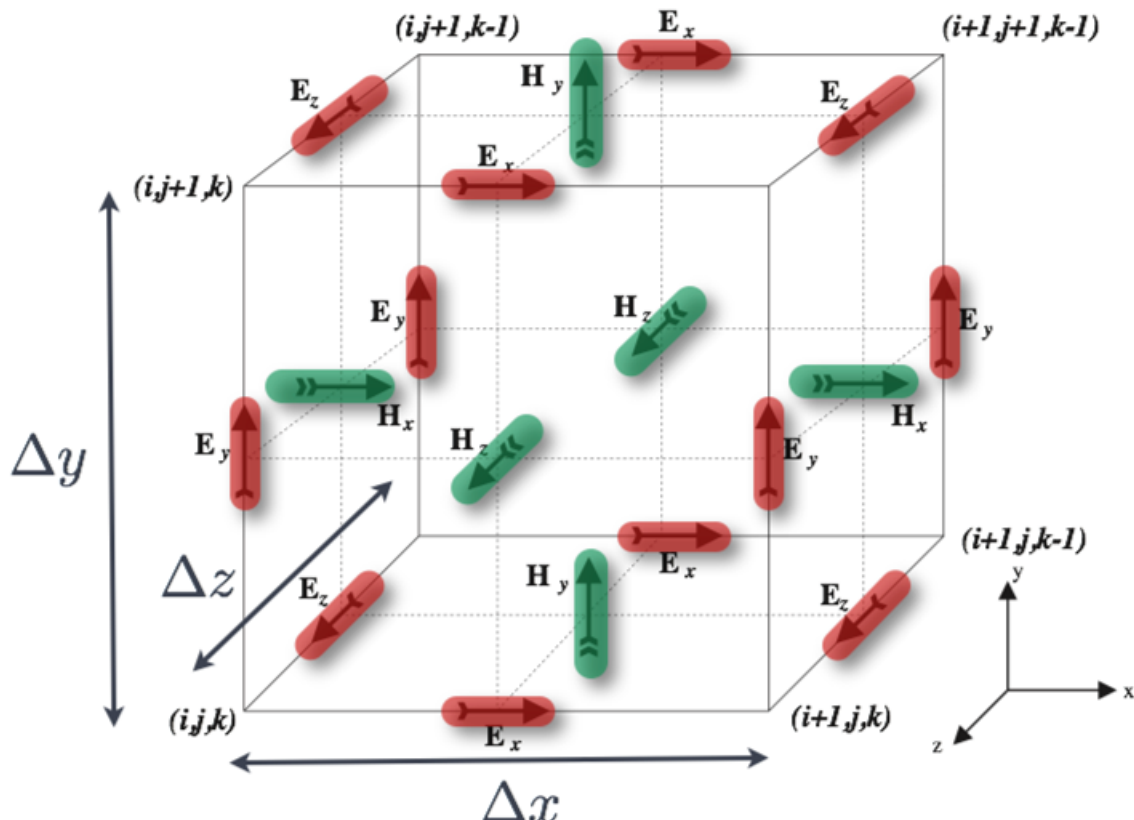


Figure 2-4: Single FDTD Yee cell showing electric (red) and magnetic (green) field components [Warren et al., 2016].

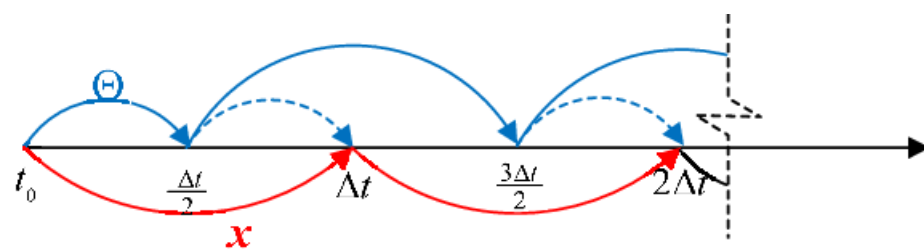


Figure 2-5: Sketch of the Leap-Frog time integration scheme [Wu et al., 2018].

$$\Delta t \leq \frac{1}{c\sqrt{\frac{1}{\Delta x^2} + \frac{1}{\Delta y^2} + \frac{1}{\Delta z^2}}}. \quad (2-57)$$

The **CFL** criterion says that the distance of any information travelling during Δt within the mesh has to be lower than the distance between mesh elements. Thus, the information from an arbitrary cell must not propagate further than its immediate neighbors for each time step.

Another important factor which influences the spatial discretization is the errors associated with numerically induced dispersion. The accumulation of numerical dispersion errors needs to be controlled by choosing a sufficiently fine spatial discretization which is also important to meet the **CFL** criterion as shown in eq. 2-57. The spatial discretization is chosen with respect to the smallest relevant wavelength present. It is generally considered appropriate to consider that the discretization step Δl [m] should be at least ten times smaller than the smallest wavelength λ [m] of the propagating electromagnetic fields to keep the dispersion error minimal:

$$\Delta l = \frac{\lambda}{10}. \quad (2-58)$$

There is no specific guideline for choosing the right spatial discretization for a given problem. In general, it depends on the required accuracy, the frequency content of the source pulse and the size of the targets [Warren et al., 2016].

2-4-4 Absorbing Boundary Conditions and Perfectly Matched Layers

Due to the finite extent of computational resources, the extend of modelling spaces need to be spatially limited. The truncation of the computational domain at a finite distance from sources and targets is one of the most challenging problems in modelling. An approximate condition, a so-called Absorbing Boundary Condition (**ABC**) is applied at a sufficient distance from the source to truncate and therefore limit the computational space. The role of this **ABC** is to absorb any waves impinging on it and simulating an unbounded space. The computational space limited by the **ABCs** should contain all important features of the model [Warren et al., 2016].

Perfectly Matched Layers (**PMLs**) resemble an extra group of **ABC**. Perfectly Matched Layer (**PML**) **ABCs** that are used by the **FDTD** software *gprMax* [Giannopoulos, 2012]. The main difference between standard **ABCs** and **PMLs** is that **PMLs** implement multiple additional layers with a material that absorbs incoming electromagnetic plane waves at any angle. This additional layer gives **PMLs** an advantage over standard **ABCs** which produce high reflection coefficients for small incidence angles. Various groups of **PMLs** exist. A variant of the Complex Frequency Shifted **PMLs** are being implemented in *gprMax* [Warren et al., 2016].

Chapter 3

Methodology

In this Chapter, the fundamentals of [GPR](#) as well as the applied [FDTD](#) software *gprMax* are introduced. A detailed understanding of the main principles of field measurements as well as the modelling software is important to develop a proper field and modeling setup which is in consequence crucial to attain accurate data for the following processing and evaluation.

3-1 Ground Penetrating Radar (GPR)

[GPR](#) is a non-destructive geophysical technique, which uses reflections of transmitted electromagnetic waves in order to investigate structures in the subsurface. It is one of the methods which has been extensively researched as a means to improve the efficiency of landmine and [IED](#) detection. In this Section, background information and the working principles of [GPR](#) are introduced.

3-1-1 General Principle

In [GPR](#), [EM](#) waves in the upper MHz to lower GHz range are emitted into the subsurface. The general field setup is shown in Figure 3-1. In order to produce [EM](#) waves, a signal generator is used as a source. The source produces high-frequency pulses which are sent from a Transmitter Antenna ([Tx](#)) into the ground. The upper part of high frequency antennas are often shielded to focus the radiation of energy into the ground [Annan, 2009]. In the subsurface, the waves propagate with a velocity, which is reduced compared to air velocity and under the influence of attenuation depending on the subsurface's (di-) electrical and parameters. At electromagnetic impedance contrasts, which are related to dielectric variations, the [EM](#) waves are reflected back to the surface and subsequently recorded by a Receiver Antenna ([Rx](#)). The received signals are sent and stored in a control unit. Traces are recorded in a predefined time window after each incremental step along the survey line [Loewer, 2018]. Each single trace resembles an A-Scan. A 2-D profile can be attained by lining up traces resulting into a 2D profile that is called B-Scan [Benedetto et al., 2016].

GPR systems primarily consist of a data collection unit, a transmitting antenna and a receiving antenna. Antennas can simultaneously function as transmitter and receiver. In most commercially available systems, the receiver antenna is installed directly next to the transmitter antenna in one casing. The separation of the two antennas is often fixed.

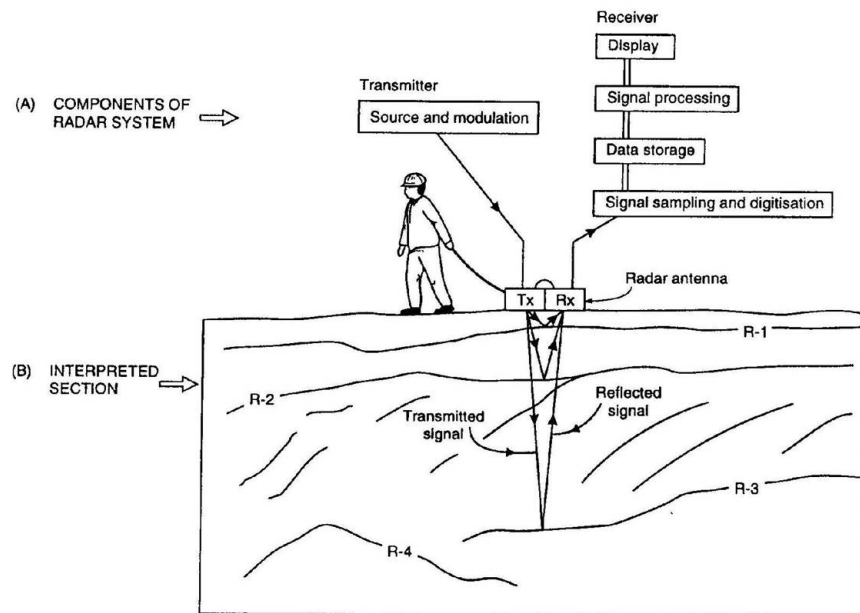


Figure 3-1: Diagram of the setup for a GPR survey [GeoSci, 2018b].

GPR can be applied in several surveying modes depending on how the Tx and Rx antennas move and the spacing between the antennas set during the survey. Figure 3-2 shows the most common survey modes used for GPR measurements. In the Common Offset method, Tx and Rx are moved simultaneously along the survey direction where the offset between the antennas is kept constant. In Common Midpoint (CMP) measurements, Tx and Rx are both moved away at the same distance from a common reference point in opposite direction [Meng et al., 2019]. Most conventional GPR systems use the Common Offset method. The antenna system is simply moved over the area of interest without the need of rearranging antennas. Therefore, the Common Offset method is a very efficient approach to quickly obtain information about the near-subsurface structure. Because of these practical reasons, the Common Offset method is used for landmine and IED detection where wider areas are investigated.

GPR systems are either ground-coupled or air-coupled, i.e. the antennas are positioned directly on the interface or above the interface with air in between. In order to achieve sufficient ground coupling, the GPR antennas are located within a preferably small distance to the ground surface. The signal from ground-coupled antennas does not travel through air and thus, the majority of the energy from the antenna is transmitted into the subsurface. Therefore, it is generally desirable to minimize the distance between antenna and ground. However, for landmine and IED detection, ground-coupled systems cannot be used for safety reasons because explosives may detonate through direct contact to the antennas. As a result, GPR measurements for EOD must be air-coupled [Oßberger et al., 2006].

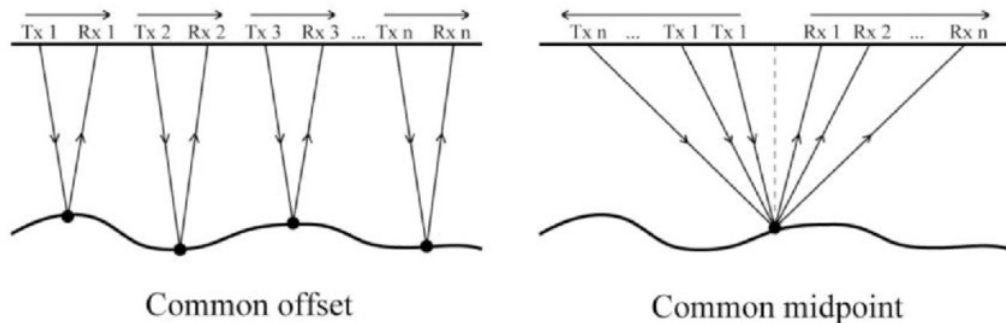


Figure 3-2: Left: Common offset mode, Right: Common midpoint (CMP) mode [Meng et al., 2019].

The transmitter and receiver antennas can also be used in different orientations as shown in Figure 3-3. Altering the orientation of the antennas can significantly improve responses depending on the geometry of the investigated targets due to the fact that typical GPR antennas radiate and receive electromagnetic waves more effectively in certain directions than others. The major part of the energy is emitted parallel to the polarization of the antenna dipoles. In the Broadside-Perpendicular orientation, the antenna dipoles are polarized perpendicular to the measurement direction while in the Broadside-Parallel orientation, the polarization is parallel to the measurement direction. Therefore, the Broadside-Perpendicular and Broadside-Parallel orientations tend to be used for detecting targets oriented parallel to the antenna axis such as pipes and elongated features [Warren, 2009].

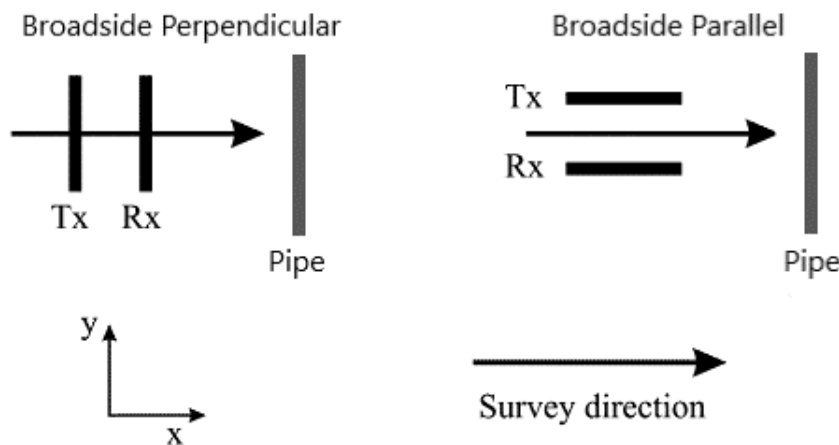


Figure 3-3: GPR antenna orientations, after [Porsani et al., 2010].

3-1-2 Influencing Factors

One main influencing factors affecting GPR performance are losses due to absorption of EM energy. Intrinsic losses are a direct consequence of the soil's dispersing electrical properties. These losses add up to other influencing factors. The characteristics of the GPR system itself is one of the fundamental aspects to be considered. The dynamic range is a factor which refers to the ratio between maximum and minimum signal power a receiver can give a

distinguishable output signal. It governs the maximum depth range where a potential survey target can be detected [Loewer, 2018]. Modern GPR systems have a total system dynamic range above 130 dB [Grimm et al., 2017].

Furthermore, transmission and ground coupling losses between the antenna and the ground commonly occur. Topography changes can cause quick variations in the antenna to ground distance which in return influence antenna-ground coupling. Moreover, antennas may be tilted which changes radiation characteristics. After rainfall events, small water accumulations in form of puddles can build up near the surface causing transmission losses. Additionally, there are energy losses due to the geometrical spreading of the propagating EM wave in the ground. There are further geological characteristics, which cause attenuation. One of these factors is the electrical conductivity σ . Moreover, heterogeneities like stones, debris and roots can cause scattering of EM waves which results in reduced data quality. Local heterogeneities in density and soil moisture need to be taken into account as well [Loewer, 2018].

The ray path of EM waves generally underlies all known optical laws such as Snell's law. In GPR, ground signals can be divided into multiple wave propagation pathways. Furthermore, waves can be grouped into spherical waves and planar wave fronts. Spherical waves propagate through the entire subsurface space at various angles (θ) while planar wave fronts travel at a critical angle θ_{crit} along the interface of two media [Annan, 2009]. The expected GPR wave-propagation pathways are shown in Figure 3-4. The direct wave is traveling through the air directly between transmitter and receiver. The ground wave on the other hand is traveling directly under the surface. Moreover, reflected, critically refracted and ground refracted waves commonly occur as well.

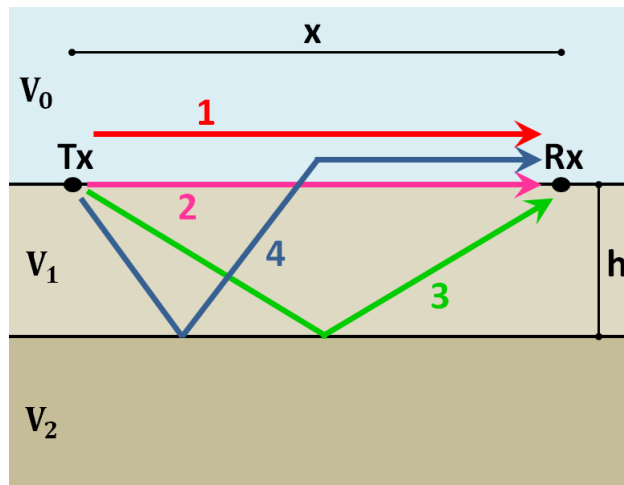


Figure 3-4: Raypath signals measured by a receiver for a 2-layer Earth: 1 = Air Wave; 2 = Direct Wave; 3 = Reflected Wave; 4 = Air Refracted Wave [GeoSci, 2018b].

Scattering is frequency dependent. At very high GPR frequencies in microwave range, the size of the heterogeneities can become in the order of the wavelength. As a consequence, Mie-scattering occurs [Takahashi et al., 2011]. The resonance or anti-resonance of the signal with the scattering object can either lead to strong amplification or attenuation of the reflected signal [Loewer, 2018].

3-1-3 GPR Data Processing

The interpretation of GPR data can be significantly improved by various data processing methods. It is important to keep in mind that if processing techniques are not applied carefully, important features can be removed or even features unrelated to the subsurface's structure may be added into the data [Warren, 2009]. For GPR data processing, multiple software programs are available. In this thesis, the software *ReflexW* (version 8.58) was used. The applied processing steps (see Figure E-1) in this thesis on measured and simulated data are subsequently introduced and briefly described. Further information about GPR data processing can be found in various literature such as [Daniels, 2004] or the *ReflexW* user manual.

The Direct Current (DC) offset shift needs to be estimated and removed from every trace individually. The DC-Shift is estimated by the samples before time-zero (the average of the samples before time-zero). The DC-Shift is subsequently subtracted from the trace. In *ReflexW*, a DC-Shift filter is implemented. The filter acts on each trace independently. This option allows the subtraction of an existing time constant shift. As filter parameter two time values (1.time and 2.time) must be entered. Within this time range the mean is calculated for each trace which is subsequently subtracted from all samples of each trace. Therefore it has to be ensured that the mean value in the corresponding time range complies with the shift to be eliminated.

A band-pass filter attenuates very low and very high frequencies but retains a middle range band of frequencies which contains the relevant subsurface information. Band-pass filtering is used to enhance edges by suppressing low frequencies while reducing the noise at the same time by attenuating high frequencies. There are various forms of bandpass-filters. One commonly used form which is also applied here is the cos-taper. The frequency windows must be selected cautiously to prevent the loss of data while removing as much noise as possible. Furthermore, selecting the wrong time window may cause structures to occur which do not represent the real subsurface signals.

The next phase is static correction which aims to moving the entire trace up (or down) in time to correct the initial time to the same level of the ground's surface. Thermal drift, electronic instability, cable length differences and variations in antenna air gap can cause 'jumps' in the air/ground wavelet first arrival time. The time zero offset is corrected by using the static correction tool in *ReflexW*. The first signal is being picked and subsequently, every first signal shifted to time zero.

In the next step, a divergence compensation was applied to compensate for geometrical divergence losses. A compensation of the geometrical divergence losses is applied proportional to the traces times. This compensation was designed to compensate for spherical losses of a 3D point source which is the nearest approximation of a 3D antenna *ReflexW* offers.

Lastly, the processed radargrams were adjusted to uniform lengths in both, measured distance and two-way traveltimes. The *removerange* command cut the measurement line's distance down where the radargram does not contain any relevant information. The same procedure was repeated for the two-way traveltimes with the *timecut* function to cut out unnecessary parts of the radargram. Lastly, the radargrams plot settings were adjusted and the final radargrams exported.

3-2 gprMax

This Section will give a short introduction to the open source FDTD software *gprMax*. A more detailed summary is given in [Warren et al., 2016], [Warren and Giannopoulos, 2016] as well as the *gprMax* User Guide and the official website.

3-2-1 General Information

gprMax is an open-source software which simulates electromagnetic wave propagation for the numerical modelling of GPR. *gprMax* is fundamentally based on solving Maxwell's equations in 3D using the FDTD method Transverse Electromagnetic (TEM) mode. The software is mainly written in *Python 3* with performance critical parts written in *Cython*.

gprMax also includes multiple user models, packages and libraries. One of these libraries contains antenna models including a model for the 1.5 GHz GSSI antenna which is used for all antenna simulations performed in this thesis. Moreover, a *Python* script for the production of radiation patterns is provided as well.

3-2-2 gprMax Input Files and Modelling Setup

To perform simulations in *gprMax*, an environment needs to be constructed. *gprMax* uses text based input files to specify the modelling setups. The *gprMax* input file commands are introduced by a # symbol. These input commands define all relevant input parameters, such as the domain size, source type, source position, discretization, time window et cetera. All dimensional values are given in SI units. In Figure 3-5, a minimal example of a *gprMax* input script is shown.

The spatial discretization Δx , Δy and Δz and time steps t play a significant role since the smaller they are the closer the FDTD model is to a real representation of the problem. As mentioned in eq. 2-58, the discretization should be at least ten times smaller than the smallest wavelength of the propagating electromagnetic fields. Note that in general low-loss media wavelengths are much smaller compared to free space. Another relevant parameter is the time window. It must be chosen sufficiently large according to the expected travel times between Tx and Rx. On the other hand, higher discretizations and longer time windows also increase the need of computational resources. Thus, the time window and discretization need to be chosen according to the computational resources available as well as the desired resolution.

The relevant subsurface's (di-)electrical properties must be defined via material definitions. Realistic soil models, heterogeneous objects (such as plates or cylinders) and rough surfaces but also dielectric smoothing can be implemented into the model. There are multiple source types which can be implemented, including the infinitesimal Hertzian Dipole. Such a dipole requires the definition of a wavelet. The Ricker Wavelet which is the second derivative of the Gaussian function is one of the most commonly applied wavelets in GPR modelling. Advanced usage, like loading antenna models is possible with python code snippets which are begun with `#PYTHON` and ended with `#END PYTHON`. In these snippets, all commands need to be written in Python format.

gprMax uses [PML ABCs](#) based on a recursive integration approach to the Complex Frequency Shifted ([CFS](#)) PML [Giannopoulos, 2012]. The [ABCs](#) employed in *gprMax* will perform well if all sources and targets are kept at least 15 cells away. Additionally, free space should be always included above a source for at least 15-20 cells in [GPR](#) models.

```
#title: B-scan from a metal cylinder buried in a dielectric half-space with a GSSI 1.5GHz 'like' antenna
#domain: 0.480 0.148 0.235
#dx_dy_dz: 0.001 0.001 0.001
#time_window: 6e-9

#material: 6 0 1 0 half_space

#box: 0 0 0 0.480 0.148 0.170 half_space
#cylinder: 0.240 0 0.080 0.240 0.148 0.080 0.010 pec

#python:
from user_libs.antennas.GSSI import antenna_like_GSSI_1500
antenna_like_GSSI_1500(0.105 + current_model_run * 0.005, 0.074, 0.170, 0.001)
#end_python:

geometry_view: 0 0 0 0.480 0.148 0.235 0.001 0.001 0.001 cylinder_GSSI_1500 n
```

Figure 3-5: Minimal example of a *gprMax* input script for a 3D model of a buried cylinder buried in a half space and the implementation of a 1.5GHz GSSI antenna.

gprMax produces an output files using the widely supported HDF5 format. It is also possible to store geometric data in the Visualization ToolKit ([VTK](#)) format by defining snapshots of an area in the model. The widely used [VTK](#) reader *Paraview* can be used to view geometric data and process snapshots.

gprMax is only capable of building up horizontal models. Moreover, antennas can only be deployed horizontally. As a result, it is only possible to simulate an ideal scenario where the antenna is in optimal position to the ground. However, the influence on antenna inclination ought to be investigated. As a direct response to this issue regarding the model implementation, [LIAG](#) developed an input script which tilts the model relative to the antenna in the desired angles. The tilts of the model is equivalent to a tilt of the antenna. It must be considered that the tilt of the model also results in the need to adjust the antenna movement to the tilting operations to move the antenna along the interface. In the following Chapter, the modelling setup of such inclined models is further explained and illustrated in sketches.

Chapter 4

Field and Modelling Data Collection

In this Chapter, the field data collection and the modelling setups in *gprMax* are described. The setup of both, the field measurements as well as the numerical simulations need to be carefully documented to attain reliable data for future evaluation. In the Section 4-1, the field data collection is described including the measurements in air and on a sandy soil. Section 4-2 focuses on the *gprMax* modelling setup for the investigation of radiation patterns as well as the implementation of the field measurement's setup for a comparison between measurements and simulations.

4-1 Field Data Collection

Field measurements need to be performed accurately under well predefined conditions. Thus, the field measurements need to be properly documented as well to outline potential influential factors which might affect measured results. The following Section describes the field measurements done in this thesis in detail.

4-1-1 Air Measurements

For the measurements, a 1.5 GHZ GSSI antenna produced by the company *Mala* was used. The antenna is of the bow tie antenna type. The receiver is positioned directly next to the transmitter. The antenna is shielded. In Figure 4-1, the inner parts of the antenna are shown.

One part of measurements was performed in air as medium. To prevent unwanted ground reflections, the measurements setup was turned upside down with the antenna radiating upwards. The entire setup consists of foamed Polystyrene, which consists to over 98% of air. Therefore, the medium does not affect the measurements and can be viewed like air. Previous test measurements performed at [LIAG](#) already proved this assumption. The distance between antenna and reflector was set after pre-measurements, to see at which minimal distance Crosstalk and reflection amplitudes are not overlapping. This was performed in a

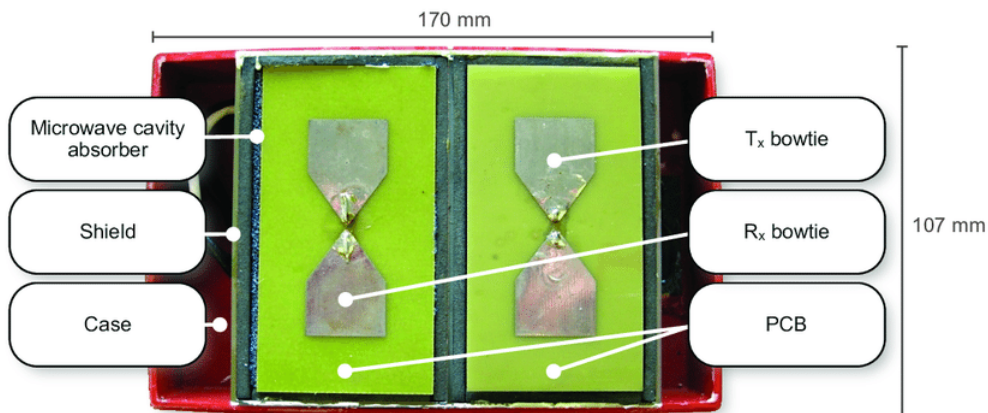


Figure 4-1: Bowtie GSSI antenna [Warren, 2009].

simple *gprMax* simulation. It is important for subsequent processing steps to ensure that the Crosstalk can be properly separated from the reflection to extract the reflection signal.

In the measurements, a metal pipe was used as reflector. First, the antenna was kept at a constant and horizontal position. The pipe was re-positioned continuously in 5 cm increments for each measurement interval in horizontal direction while the vertical distance (i.e. height) over the antenna remained constant at 99.5 cm. A sketch of the measurement setup is shown in Figure 4-2.

To attain information about the dependencies at different angles, two additional measurements were performed. One measurement was performed in Broadside-Perpendicular and the second one in Broadside-Parallel antenna configuration. During these measurements, the pipe was kept stationary while the inclination of the antenna was changed in 5° increments starting from 30° to 120°. In Figure 4-2, the measurement setup is sketched. For each angle, one measurement was performed. The acquired data were then processed and their E-field amplitudes plotted into a polar plot.

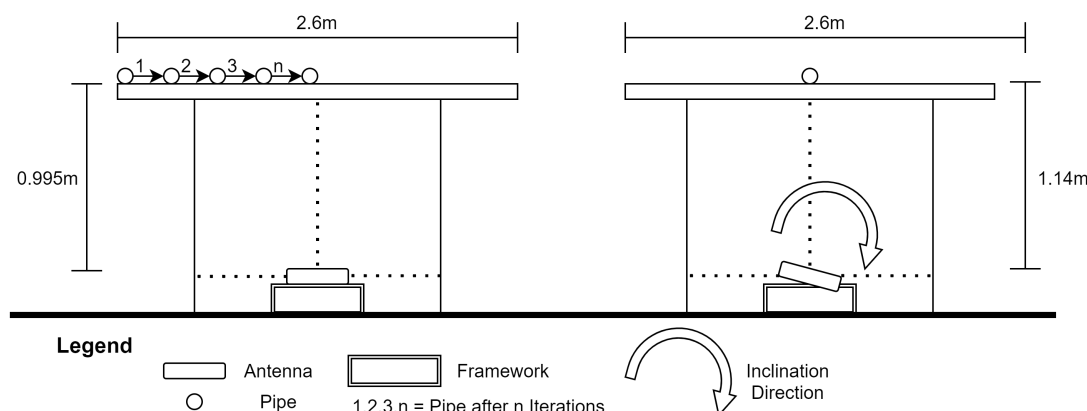


Figure 4-2: Foamed Polystyrene measurement setup, Left: Reflector moved, Right: Inclinations changed.

4-1-2 Measurements on Sand

The second part of the measurement campaign was performed on a sandy subsurface. In Figure 4-3, the measurement setup is illustrated. An even hill of fine grain sand was bulked to a height of approximately 1 m. Below the sand bulk, a floor of concrete was located. The sand was very fine grained and shows very low soil moisture. The relative permittivity of the sand was measured in the laboratory measurements as well. The area covered by the sand bulk was 2 x 3.5 m. In 55 cm depth to the surface, a metal pipe was buried in the center and perpendicular to the measurement line. The pipe had a length of 49 cm and a radius of 1 cm. A synthetic tarp was deployed on the sand hill to stabilize it against sliding due to the sand's low cohesion.

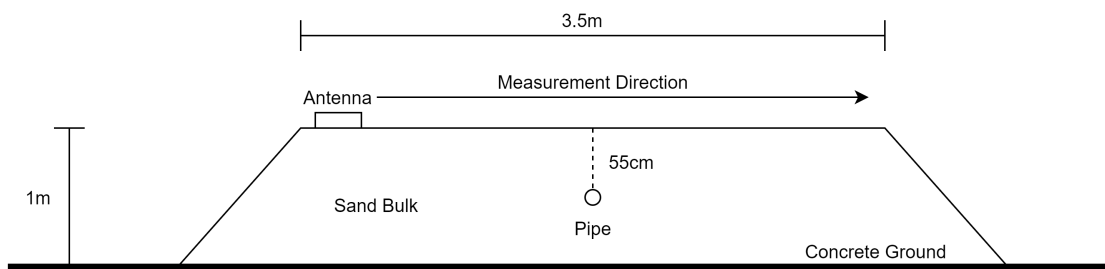


Figure 4-3: Measurement setup of the measurements on sand.

Again, the 1.5 GHz GSSI antenna was used for the measurements. The measurements were performed in various configurations. Firstly, the measurements were performed at Broadside-Perpendicular and Broadside-Parallel configuration for every measurement setup. In addition to horizontal measurements, inclinations of 15° and 30° were measured as well. Furthermore, the inclination was set parallel as well as perpendicular to the measurement direction. Lastly, different elevations from the antenna to the sand in horizontal antenna position were measured. The antennas were set at 8 cm and 13 cm height above ground. In Table 4-1 and 4-2, all measured configurations are summarized.

Table 4-1: Listing of the inclined measurements (Inline = Inclination parallel to measurement direction, Crossline = Inclination perpendicular to measurement direction).

Antenna Orientation	Inclination	Direction
Broadside-Perpendicular	15°	Inline Crossline
Broadside-Perpendicular	30°	Inline Crossline
Broadside-Parallel	15°	Inline Crossline
Broadside-Parallel	30°	Inline Crossline

Table 4-2: Listing of the horizontal measurements.

Antenna Orientation	Elevation
Broadside-Perpendicular	0 cm
	8 cm
	13 cm
Broadside-Parallel	0 cm
	8 cm
	13 cm

4-2 gprMax Modelling Data Collection

The radiation characteristics of the infinitesimal Hertzian Dipole and the 1.5 GHz GSSI antenna (see Figure 4-5) are investigated by acquiring radiation patterns from **FDTD** simulations in *gprMax*. Moreover, the **GPR** field measurement's setups were implemented into *gprMax* to run simulations analogously to the field measurements to compare field results with the numerical ones. In the following Sections, the *gprMax* modelling setups for each field of investigation are presented.

4-2-1 Radiation Patterns

To produce radiation patterns, a 3D model needs to be set up for both, the Hertzian Dipole measurements as well as the antenna measurements. The antenna model is by definition three-dimensional which makes a 3D model imperative. For the Hertzian Dipole, *gprMax* has the option of running 2D Transverse Magnetic (**TM**) simulations. However, there is no implementation for Transverse Electric (**TE**) measurements. Thus, also the Hertzian Dipole measurements needed to be run in **TEM** mode to consistently perform measurements for E-Planes and H-Planes. A sketch of the model setups is given in Figure 4-4. The models for both sources consist of two half spaces. The upper half-space is meant to represent air with a relative permittivity $\epsilon_r = 1$, while the lower half space is meant to represent the subsurface. The subsurfaces relative permittivity was set to 1, 4 and 16 where at $\epsilon_r = 1$ the half space scenario changes into the full space scenario. The domain boundaries were surrounded by 10 energy absorbing **PML** cells to ensure that no boundary reflections occur. The source was set at different heights above the interface (0, 2, 7 and 15 cm).

As a first source, an infinitesimal Hertzian Dipole was used. A Ricker Wavelet with a frequency of 1.5 GHz was implemented. The source was horizontally deployed on the air-soil interface. 200 receivers were deployed in a constant radius concentrically according to the coordinate system in Figure 2-3 to measure the energy radiation from the dipole used for the plotting the radiation patterns. To plot the E-Plane ($\phi = 0^\circ$) in the model, the polarization of the dipole had to be set along the X-axis. For the H-Plane, the dipole polarization must be changed from $\phi = 0^\circ$ to $\phi = 90^\circ$. To achieve this 90° shift in *gprMax*, the polarization of the Hertzian Dipole was changed from X to Y-direction. Otherwise, the model setup and execution remained unchanged. The discretization of the simulations was set to 2 mm for every measurement. The results were compared to the analytical solutions from [Smith, 1984].

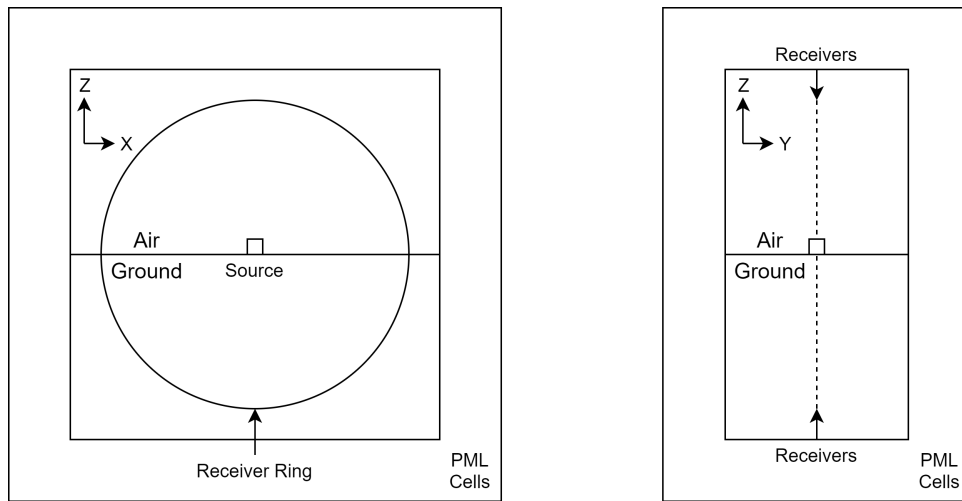


Figure 4-4: Sketch of the radiation pattern's measurement setup.

A similar setup was built up for the antenna radiation patterns. Instead of the Hertzian Dipole, the 1.5 GHz GSSI antenna model was implemented. The excitation source of the antenna was positioned where previously the Hertzian Dipole was positioned. Figure 4-5 shows the model of the implemented GSSI Antenna. Due to the spatial extensions of the antenna (while the Hertzian Dipole is a point source), a domain had to be set up between the **PML** cells having at least the size of the antenna. The domain size of both models is kept equal. Also, the discretization for the antenna was set to 2 mm as well. The same antenna heights above the interface as for the Hertzian Dipole were investigated.

As briefly mentioned previously, the receiver ring was positioned according to Smith's coordinate system. Thus, the center was set at the interface. Moreover, it must be ensured that the receivers have a minimal distance of 15 cells to the **PML** cells to prevent potential interference between receivers and **PML** cells. For a discretization of 0.002 m, a minimal distance of 0.03 m must be kept to the **PML** cells.

The far-field is tested iteratively, where the radii are successively increased. Multiple receiver radii can be investigated in one simulation. Based on the far field investigations, the radii for the final far-field radiation patterns are determined. In Table 4-3, an overview of the radiation pattern models is given. As can easily be seen in the parameter table, all models use lossless media.

Table 4-3: Radiation pattern model parameters.

Model	ϵ_r [-]	μ_r [-]	σ [S/m]	Elevations [cm]	Discretization [m]
Full Space	1	1	0	0	0.002
Half Space 1	4	1	0	0, 2, 7, 15	0.002
Half Space 2	16	1	0	0, 2, 7, 15	0.002

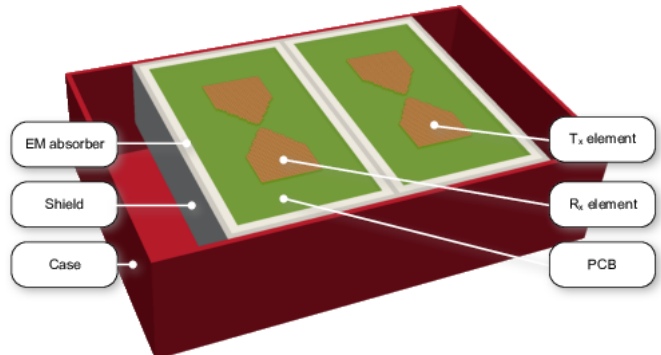


Figure 4-5: FDTD mesh of geometry of a GSSI 1.5 GHz antenna [Warren, 2009].

4-2-2 Air Measurements

For the measurements in air, the field setup was transformed into *gprMax*. The B-Scan mode of *gprMax* was used to simulate each step of the simulation. A relative permittivity of $\epsilon_r = 1$ was defined as well as a relative permeability of $\mu_r = 1$ and $\sigma = 0$. The implemented pipe was represented by a cylinder whose long side was positioned perpendicular to the movement direction. The cylinder was defined as perfect electrical conductor. The domain boundaries were covered by PML cells similar to the radiation patterns models to prevent boundary reflections. A sketch of the measurement setups is given in Figure 4-6.

In the first part of the air measurements, the 1.5 GHz GSSI antenna was set at a constant position while the implemented pipe was moved 5 cm per iteration. The only difference between the field measurement's setup and the simulated *gprMax* environment is the turning of the field setup which is not necessary in *gprMax* due to the PML cells preventing any unwanted reflections from the ground.

In the second group of simulations, the antenna was not successively inclined like in the field measurements. The simulations change the cylinder positions relative to the antenna while the antenna remains stationary. The cylinder always remains at a constant distance (the same as in the field measurements) while the angle between the horizontal plane of the antenna and the cylinder was successively increased. As a result, the cylinder wanders radially along a circle for each iteration. The angles of the cylinder relative to the antenna are identical to the field measurements angles and thus, the simulation results are comparable to the field measurements. In conclusion, the *gprMax* model setup is analog to the field setup in terms of inclinations and distances despite the differences in both setups.

4-2-3 Sand Measurements

Also the field measurements on sand were implemented in *gprMax*. The length of the measurement line for the horizontal measurements was set at 2.5 m to ensure that the reflector is covered by the measurements while the domain size was kept at a minimum for computational reasons. The buried pipe was implemented similar to the air measurements as a cylinder and perfect electrical conductor. The sands dielectric permittivity was defined according to the findings of the laboratory measurements of sand samples taken in the field which yielded an ϵ_r of $\approx 2.45 - 2.6$. Thus, the ϵ_r value for the simulations was chosen on these findings and set

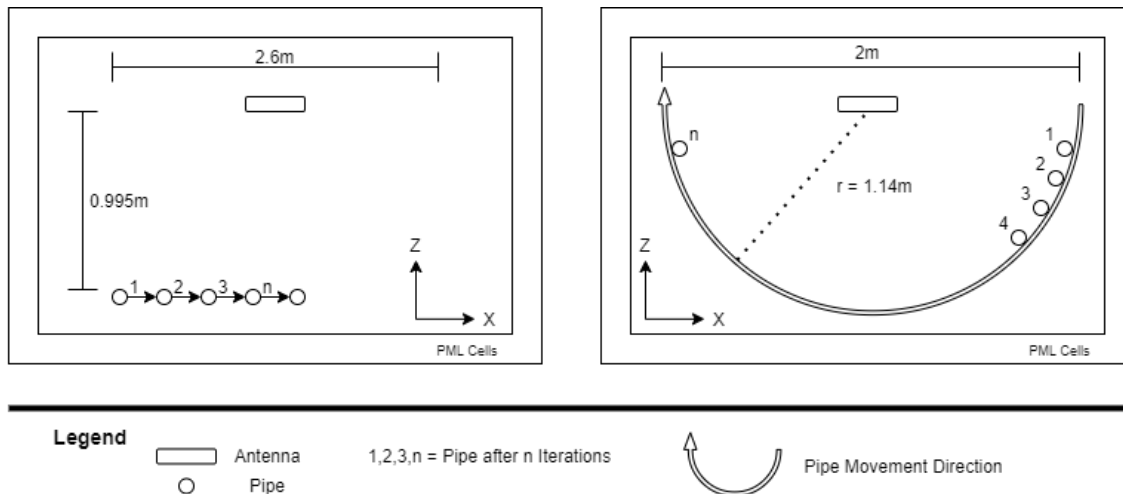


Figure 4-6: Sketch of the air measurements, Left: Reflector moved horizontally, Right: Reflector moved in constant radius.

to 2.5, a value well in the middle of the measured range. μ_r and σ were kept at 1 and 0 respectively which also means that the model is lossless and the subsurface homogeneous again. The pipe depth is 55 cm and the position of the pipe is in the center of the measurement line. Moreover, there is additional domain space implemented to ensure that the antenna remains inside the domain enclosed by the PML cells. Moreover the minimum distance of each implemented object to the PML cells of 15 cells was incorporated as well. This model is used for the measurements where the antenna is kept horizontal. B-Scans with an increment of 2 cm are measured which means that in total 126 iterations are necessary to sample the entire measurement line. The horizontal measurements were performed at the same antenna configurations and elevations as in the field measurements. In Figure 4-7, the setup for the horizontal measurements is shown.

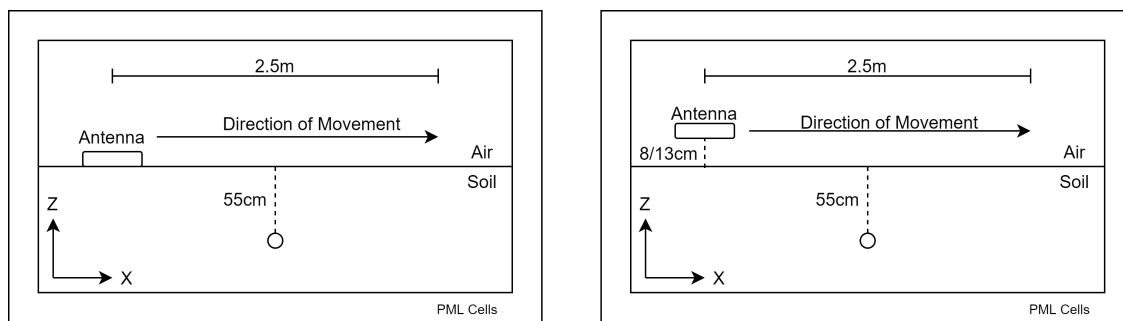


Figure 4-7: Sketch of the horizontal sand measurement *gprMax* modelling Setups Left: No elevation, Right: With elevation.

Lastly, the field measurements where the antenna is inclined must be simulated in different models. *gprMax* is not capable of inclining antenna models. Thus, the horizontal model must be skewed according to the desired antenna inclination while the antenna itself remains horizontally positioned. The initial model needs to be skewed twice to simulate antenna inclinations parallel and perpendicular to. In Figure 4-8, the skewed models are illustrated. To

simulate an antenna inclination parallel to the measurement direction, the model must be skewed 'inline' which means along the X-axis as shown in Figure 4-8. To simulate an inclination perpendicular to measurement direction however, the model must be skewed 'crossline' along the Y-axis.

The skewed models are shorter than the horizontal models. Thus, the measured lines including the number of simulated iterations is lower as well. In Table 4-4, the number of iterations and the total length of the measurement line is summarized for each *gprMax* modelling setup. The iteration increments for the skewed models are kept at the same 2 cm as for the horizontal models.

Skewing the model also leads to the necessity to adapt the increment steps in the 'inline' model because they are not moving at constant Z-position in X-direction anymore as shown in Figure 4-8. The steps now include a Z-axis component. However, the horizontal increments of 2 cm are directly related to the new increments by basic trigonometric relations. As shown in Figure 4-8, the new increments can be represented by the legs of a right angled triangle while the old increment of 2 cm in total can be represented by the triangle's hypotenuse.

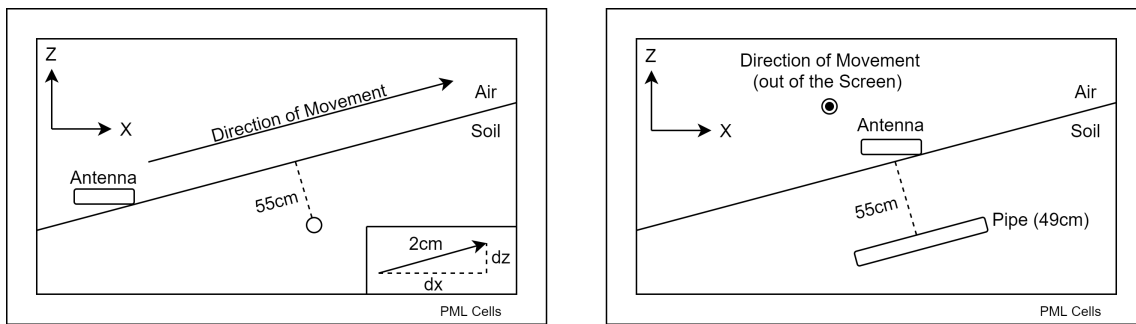


Figure 4-8: Sketch of the inclined *gprMax* sand measurements. Left: Inline, Right: Crossline.

Table 4-4: Model parameters of the *gprMax* simulations on sand.

Model	Traces	Profile Length [m]
Horizontal (0-13 cm)	126	2.5
Inclined Inline 15°	78	1.54
Inclined Inline 30°	87	1.72
Inclined Crossline 15° and 30°	98	1.94

Chapter 5

Results and Discussion

In this chapter, the results of all simulations and field measurements are presented and discussed. In Section 5-1, the Radiation Patterns are shown. Derived analytical solutions of the Hertzian Dipole are given which were subsequently used to compare them to numerical solutions in full and half space. In Section 5-2, the results of the measurements in air are presented including the measurements where the reflector was moved constantly and where the antenna inclination was varied. In Section 5-3, the sand measurement's results separated in horizontal and inclined measurements are shown. Due to the large number of diagrams, plots and radograms, only a fraction of them is shown in this Chapter.

5-1 Radiation Patterns

In the first Section the results of the investigations of the radiation patterns are presented and discussed. Moreover, it was investigated at which radius the far-field is reached. After that, the radiation patterns of the Hertzian Dipole and the 1.5 GHz GSSI antenna are presented for the full and half space directly on ground. Lastly, the effect of subsurface changes and source elevation are presented. All values were normalized by their respective maxima for better comparison.

5-1-1 Far-Field Investigation

Before the far-field radiation patterns could be produced, the radial distance where the far-field is reached must be determined. As maximal radius of investigation, 2.8 m were used. This radius marks the computational limitation which prohibits further increase of radii. For the full space, the far-field was reached at very low radii for both, the E-Plane as well as the H-plane. This observation applies for the antenna as well as the Hertzian Dipole. Only minor changes were observed in the antenna H-Plane pattern while the E-Plane is already stationary as can be seen in Figure 5-1. The slight change of the antenna's H-Plane pattern may be related to the three-dimensional character of the antenna itself, especially its asymmetric

shielding in this orientation relative to the source excitation point. The shielding focusing the energy into the subsurface. Because the shielding is not axially symmetric, the energy is not focused perfectly symmetric as well. Thus, the changes are related to the antenna geometry itself rather than physical reasons in the changes of the far-field. In conclusion, for the full space, the far-field is reached well below 10λ . Figure 5-2 shows that for $\epsilon_r = 4$, the far-field is reached at 2.5 m while at 2.8 m barely any changes could be observed. Far-field investigations for $\epsilon_r = 16$ (see Appendix A) indicate a far-field reached at 0.9 m.

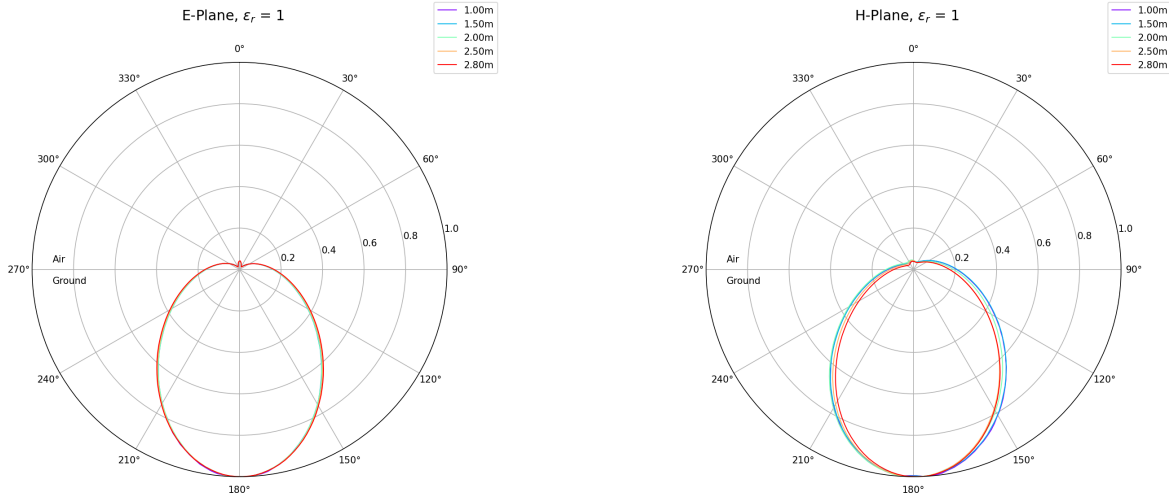


Figure 5-1: Antenna radiation patterns for far-field investigations in full space.

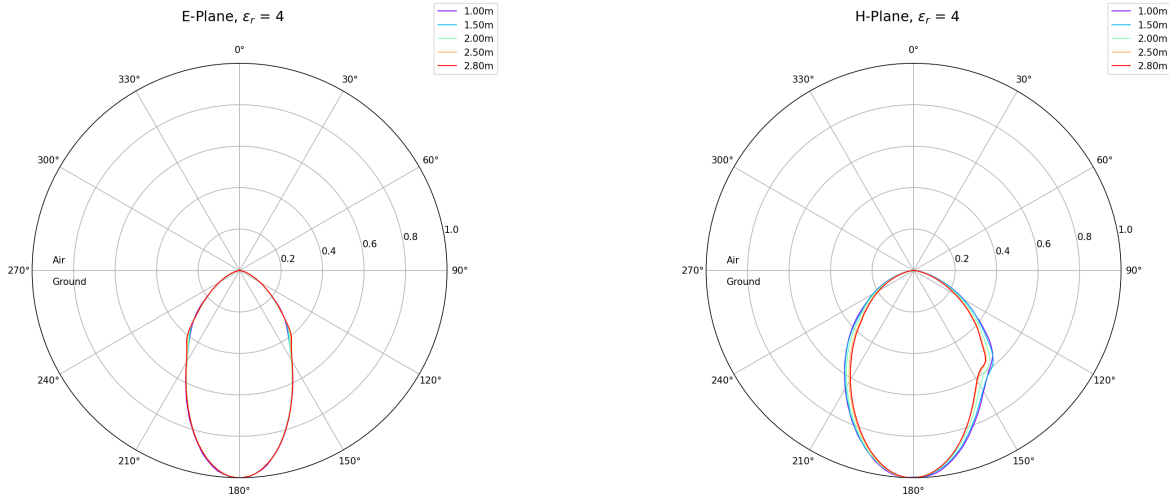


Figure 5-2: Antenna radiation patterns for far-field investigations in half space.

For the Hertzian Dipole as shown in Appendix Chapter A, there are some minor changes in the lobes left. However, computational limitations and only slight variations justify the assumption that at 2.5 m, the far-field is also reached there for $\epsilon_r = 4$ and 0.9 m for $\epsilon_r = 16$. For both source, these distances are well over the 10λ assumption. This observations was already made by [Warren, 2009] which confirms these observations. In conclusion, for the far-field radiation patterns, a radius of 2.5 m was used for each simulation to ensure uniformity.

5-1-2 Hertzian Dipole Analytical Solutions

An example of the E-Plane and H-Plane radiation patterns for media at $h = 0$ cm is given in Figure 5-3. For $h = 0$ cm, the upper half-space of both planes resemble a single lobe. As ϵ_r and therefore the refraction index n increases, the lobe in the upper half space shrinks. For $n > 1$, the power radiated into the subsurface is always greater. In the subsurface, the E-Plane shows three lobes, whereas in H-Plane, the pattern shows two maxima located symmetrically around the minimum located at $\theta = \pi$. In the E-Plane, the sidelobes show a more dominant behavior as ϵ_r increases. A higher directivity can be observed with increasing ϵ_r . Analytical solutions of the infinitesimal dipole positioned directly on the air-ground interface were also derived by [Engheta et al., 1983]. These patterns for this special case ($h = 0$ cm) are equivalent validating the approach of [Smith, 1984].

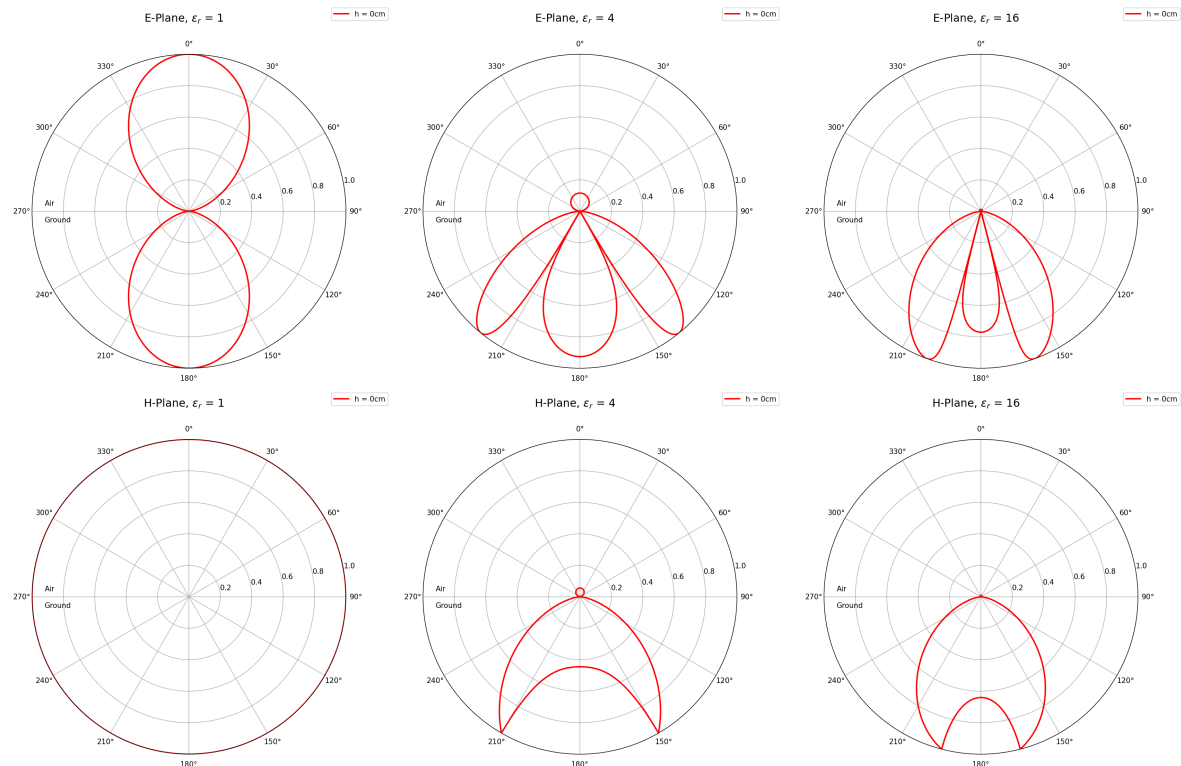


Figure 5-3: Analytical solutions at $h = 0$ cm for different ϵ_r values.

Figure 5-4 shows the patterns on and above ground for $\epsilon_r = 4$. In the E-Plane, the sidelobes decrease with increasing height until only the central main lobe remains. Meanwhile, the magnitude of the patterns in the air increases with height indicating an increasing loss of energy into the air. The H-Plane patterns show an increasing spikiness at increasing elevation. The magnitude in air increases as well. The spike is located at the critical angles location. Globally, it can be observed that at the half-width of the beam at $\theta_{crit} = \sin^{-1}(k_{12})$ changes of the lobes characteristics occurs for both, the E-Plane as well as the H-Plane on and above the interface. In conclusion, the horizontal electric dipole produces a beam into the half-space below the antenna when the dipole is located in the air above the subsurface.

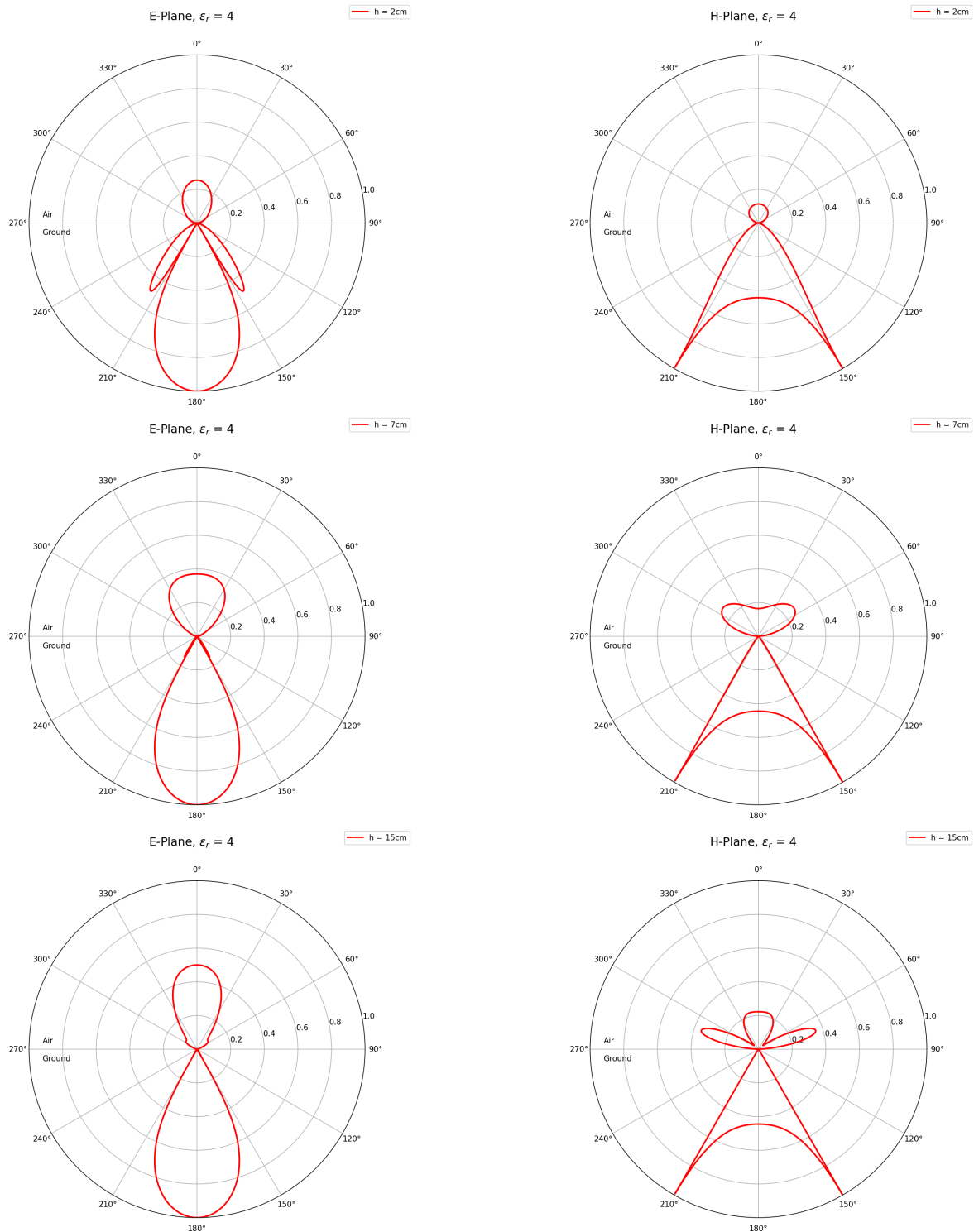


Figure 5-4: Analytical solutions at $\epsilon_r = 4$ for different heights h (top: 2 cm, middle: 7 cm, bottom: 15 cm).

5-1-3 Hertzian Dipole: Comparison between Analytical and Numerical Solutions

In this Section, the previously derived analytical solutions are compared to the numerical results from *gprMax* for the Hertzian Dipole. Main variations between analytical and numerical solutions are pointed out and potential reasons discussed.

Full Space

The radiation patterns calculated by the derived solutions of the Poynting vector (eq. 2-45) were plotted against the numerical *gprMax* solutions. For the full space ($\epsilon_r = 1$), no variations between the analytical and numerical solutions can be observed as can be seen in Figure 5-5. Both, the E-plane as well as the H-Plane match well. These observations are in accord to the validations performed by [Warren et al., 2016] which are also shown on the *gprMax* website where the analytical solutions of free space also match the modelling solutions.

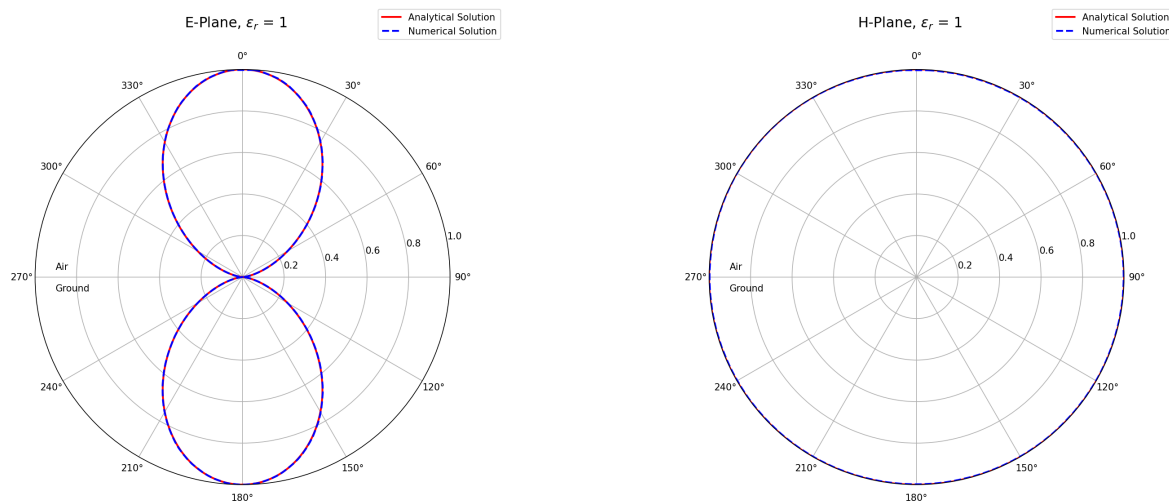


Figure 5-5: Radiation Patterns of the Hertzian Dipole in full space.

Half Space

Unlike in the full space, the half space simulations show clear variations. In the lower half space in Figure 5-6 and 5-7, variations can be observed especially at the edges of the patterns. However, in all patterns, the highest magnitudes are measured in the subsurface which is in accord to the analytical solutions. For the E-Plane, the analytical solution shows three distinct lobes which are correctly reproduced by the simulations. However, the narrow gaps between the lobes are only partly reproduced. The shape and position of the three lobes correlate with the analytical solution but the shape and magnitude of the lobes vary significantly. In Figure 5-6 and 5-7, the sidelobes are smaller in thickness and magnitude. In both figures, it can be observed that the central part between the sidelobes is poorer resolved than the other areas of the radiation patterns. At the tips of the sidelobes, distinct kinks pointing away from the center (180° line) are observed. These kinks do not exist in the analytical solutions.

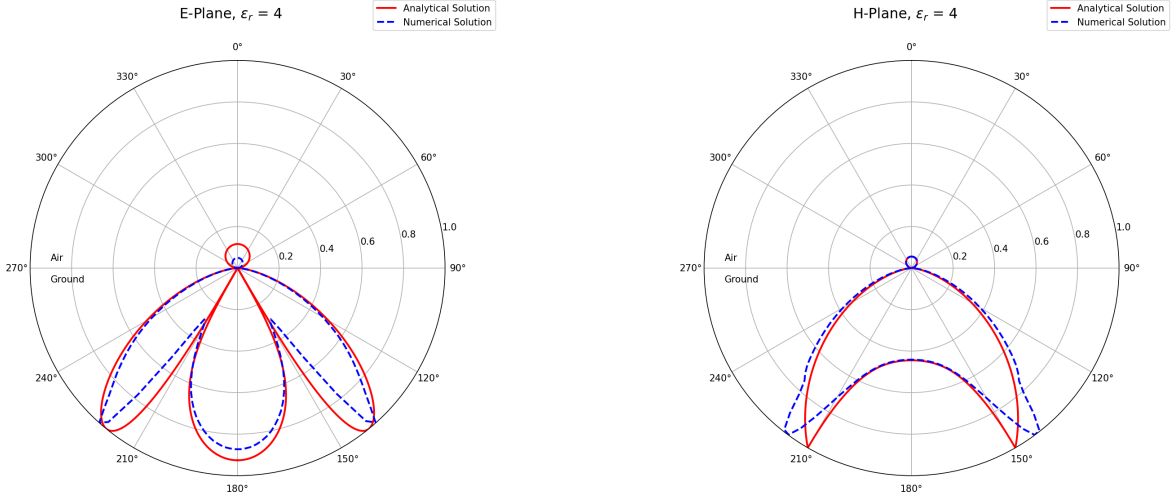


Figure 5-6: Radiation patterns of the Hertzian Dipole on a half space, $\epsilon_r = 4$.

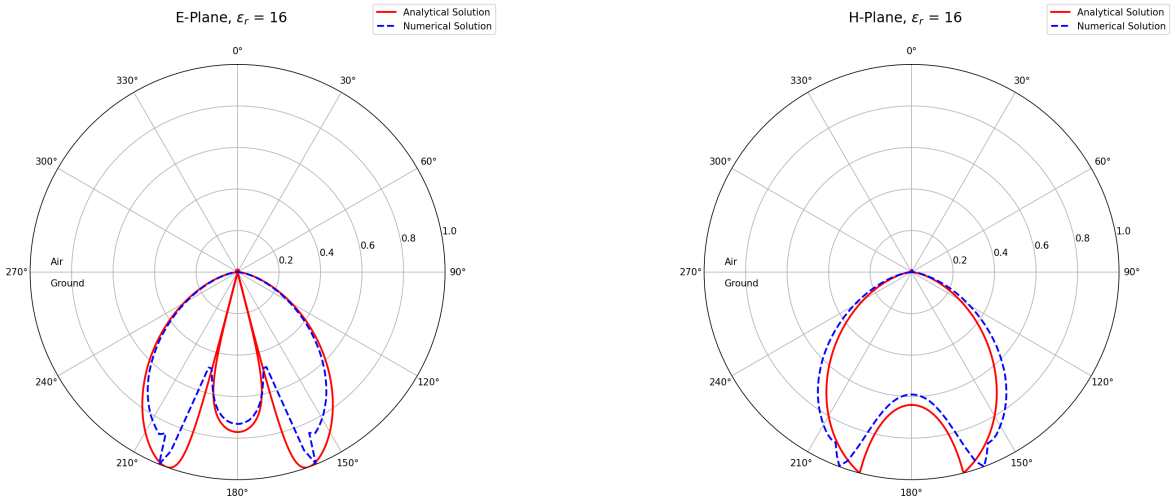


Figure 5-7: Radiation patterns of the Hertzian Dipole on a half space, $\epsilon_r = 16$.

The H-Planes show a higher correlation to the analytical solutions. Similar to the E-Plane, there are distinct kinks at the edges of the highest amplitudes which are not in accord to analytical solutions. Nonetheless, the numerical solutions match the analytical solutions in most parts of the patterns. The models in Figure 5-6 and 5-7 show a slight widening of the pattern which is wider than the critical angle.

To ensure that the model used for the radiation patterns, the H-Planes were also calculated for the 2D TM mode. As shown in Figure 5-8, the 2D TM mode shows similar patterns which implies that the model in 3D works correctly and deviations from the analytical solutions are not related to errors in the modelling setup. The same procedure was repeated for the simulations where the source was elevated where no major deviations were observed.

One of the major reasons of the variations between analytical and numerical solutions may lie in near-field effects which are not properly resolved. The analytical solutions, which are far-field solutions, do not include the effect of the near-field which plays a major role in the

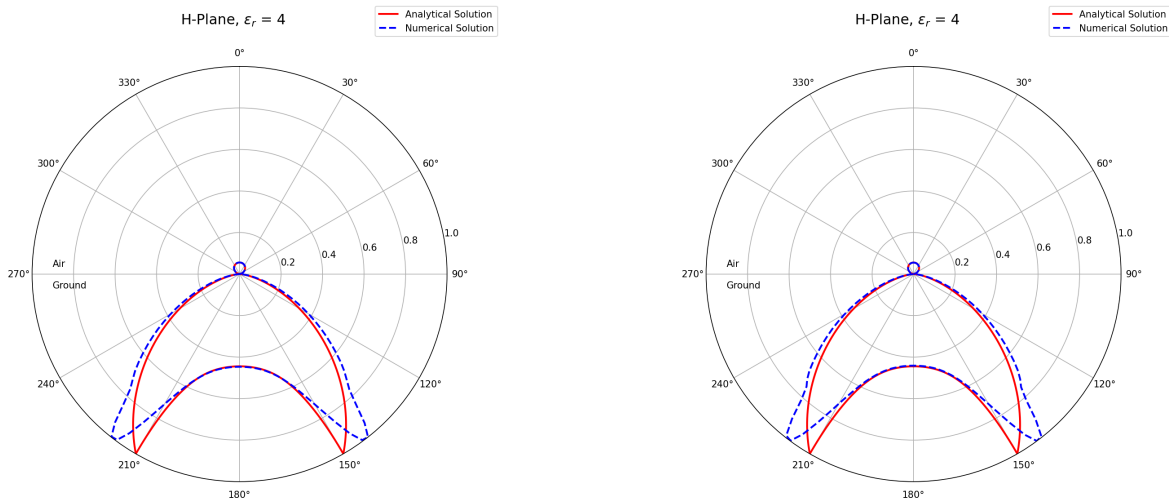


Figure 5-8: H-Plane radiation patterns of the 2D TM (left) and 3D TEM Model (right).

formation of EM waves in the subsurface. In the near-field, interactions with the surrounding subsurface occur affecting charges and currents. Such effects can be capacitance and inductive effects which can lead to the storage and deflection of energy for example. In conclusion, near-field effects influence the subsequent formation of the far-field which in turn influences the shape of the far-field patterns. On the other hand, near-field effects do not play any major role in the full space scenario because the free space does not have any significant (di)-electric properties which could be related to relevant near-field interactions. As a result, the full space numerical result perfectly matches the analytical solution.

5-1-4 Antenna Radiation Patterns

A major aspect of the antennas radiation characteristics lies in the influence of shielding. Shieldings are designed to minimize the air emitted part of the energy to focus energy into the subsurface. These effects are of high importance for real field measurements because real antennas are used while the Hertzian Dipole is a purely theoretical construction. Thus, the antenna radiation characteristics are of increased importance to consider in field measurements. In this Section, the radiation patterns of the 1.5 GHz GSSI antenna are presented and major differences to the Hertzian Dipole pointed out.

Full Space

In the antenna radiation patterns in free space, which are shown in Figure 5-9, the most obvious change to the observation to the Hertz patterns is its directive energy distribution. The energy is mostly focused into the bottom areas. This is a direct consequence of the antenna shielding. It can therefore be said that the shielding successfully focuses energy into the subsurface. Barely any energy is emitted into upper parts. The E-Plane shows symmetrical behaviour while the H-Plane is asymmetrical. This asymmetric behaviour can be explained by the geometry of the shielding itself as already pointed out in the far-field investigations. While in E-Plane orientation the casing of the shielding is axially symmetric

to the transmitter position. However, the H-Plane is slightly set off to the casing's mirror plane. Therefore, the casing of the shielding focuses the energy unevenly resulting in the H-Plane's asymmetric behaviour.

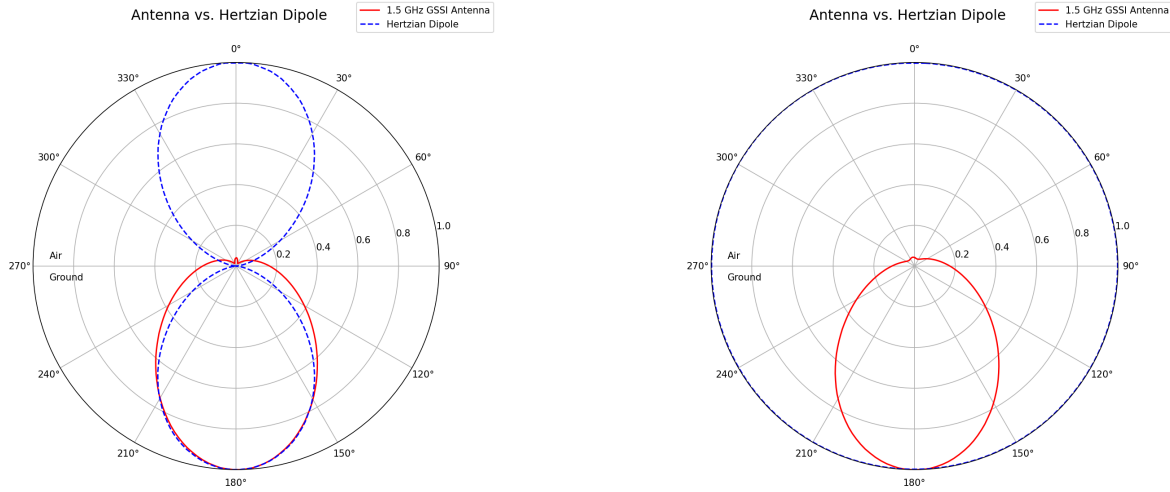


Figure 5-9: Radiation patterns of the 1.5 GHz GSSI antenna in full space.

Half Space

After the antenna simulations in full space, half space simulations were performed to simulate realistic subsurface scenarios. As shown in Figure 5-10 and 5-11 it can be observed that almost no energy is emitted into the air when the antenna is located directly on the ground. Unlike for the Hertzian Dipole, the E-Plane does not show any sidelobes, but only a big major main lobe. The E-Plane has its maximum directly below the antenna. The H-Plane on the other hand is slightly skewed similar to the full space scenario which was explained in the previous Section. At far-field distances, the maximum is directly below antenna as for the E-Field. Compared to the Hertzian Dipole, no distinct peaks or kinks can be observed.

5-1-5 Influence of Subsurface

The applied ϵ_r values for the subsurface significantly influence radiation patterns for both, the Hertzian Dipole as well as the antenna patterns. Increased ϵ_r values increase the critical reflection angle (see eq. 2-30) directly resulting from the higher difference between the wavenumbers of both media as mentioned in Section 2-3 which in turn narrows down the radiation patterns. In Figure 5-10 and 5-11, this trend is shown for both sources.

A higher directivity towards the areas directly below the sources also influences the magnitude of the antenna's H-Plane. Higher ϵ_r values lead to less pronounced skewing as shown in Figure 5-11. Lastly, higher ϵ_r values result into lower velocities and therefore lower wavelengths (see eq. 2-13 and 2-26). As mentioned in eq. 2-58, the spatial discretization should be at least ten times smaller than the smallest wavelength to prevent high numerical dispersion. It is an important factor to consider if areas with increased ϵ_r values are supposed to be simulated.

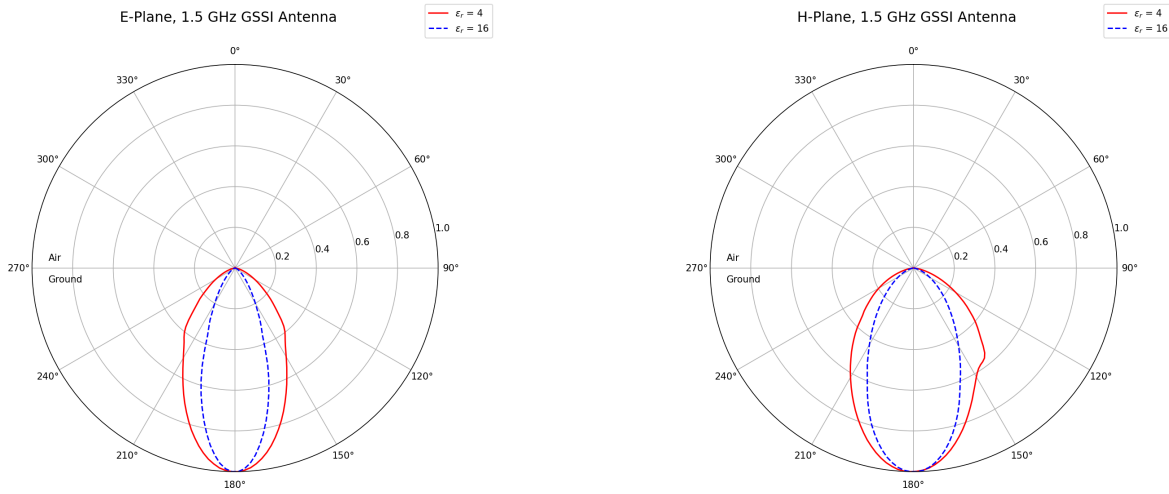


Figure 5-10: Radiation patterns of the 1.5 GHz GSSI antenna for $\epsilon_r = 4$ and $\epsilon_r = 16$ ($h = 0$).

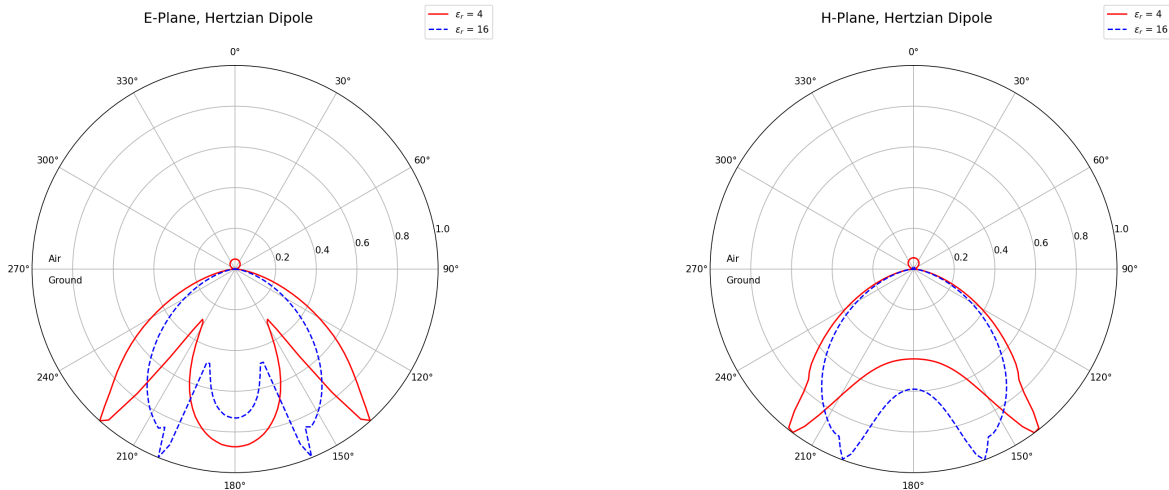


Figure 5-11: Radiation patterns of the Hertzian Dipole for $\epsilon_r = 4$ and $\epsilon_r = 16$ ($h = 0$).

If the dispersion error exceeds acceptable error ranges, the spatial discretization needs to be increased. However, as a consequence, more computational resources would be needed.

5-1-6 Influence of Elevation

In Figure 5-12, the radiation patterns of the Hertzian Dipole of various elevations are shown. When it is positioned above the surface, more energy is emitted into the air as already shown in the analytical solutions due to poorer antenna-ground coupling. Similarly, the numerical results of the Hertzian Dipole's E-Plane show a main lobe focused directly under source. It can be observed sidelobes completely disappeared already at low elevations (7 cm). The air part in the E-Plane Patterns is lower in the simulations compared to the analytical solutions. The numerical H-Plane solutions completely fail to reproduce the sharp spikes in the analytical solutions. This observations has already be made by [Diamanti and Annan, 2013].

For the H-Planes, the air part is increased in simulations compared to the analytical solutions which is an opposite trend to the E-Planes. Nonetheless, the general form of the air component matches the analytical solution. The deviations may have the same reasons as previously discussed in the scenario where the antenna was positioned directly on the interface. Near-field effects may not be considered in the analytical solutions. For the antenna patterns in Figure 5-13, the shielding improves emission into subsurface. The shielding effectively minimizes the air component significantly. The elevation effects are much stronger for the unshielded Hertzian Dipole. The E-Plane remains symmetric while the H-Field of the radiation patterns is asymmetric again. Although not as pronounced as at the Hertzian Dipole, an increase of directivity can also be observed in the antenna patterns with increasing elevation.

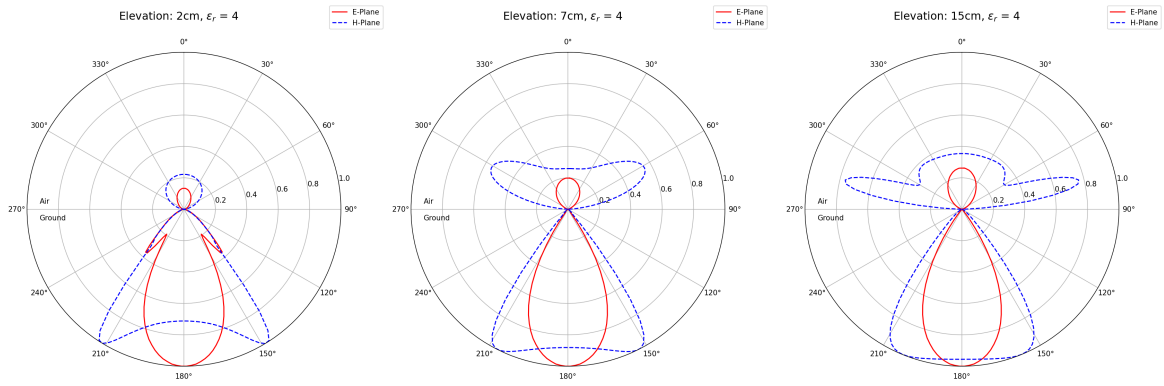


Figure 5-12: Radiation patterns of the Hertzian Dipole at various elevations (2, 7 and 15cm).

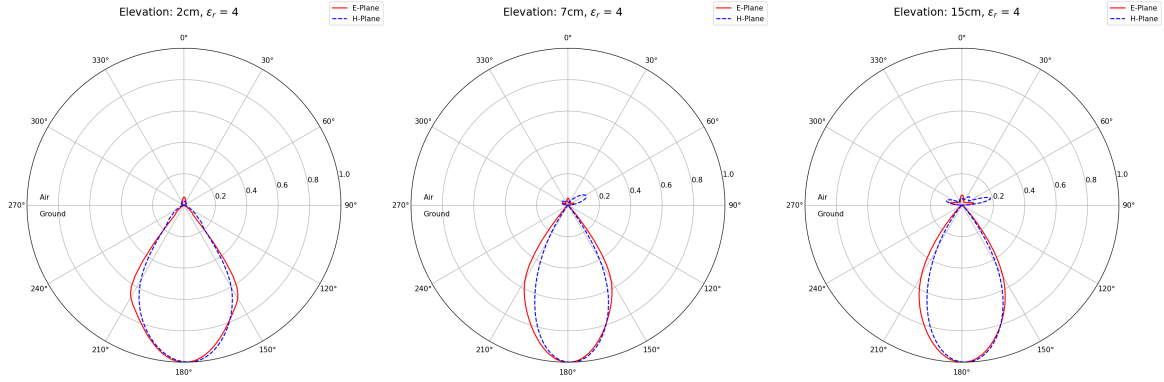


Figure 5-13: Radiation patterns of the antenna at various elevations (2, 7 and 15 cm).

5-2 Air Measurements

The measurements in air are the first part of the field measurement campaign. In this Section, the measurement's results are presented and subsequently discussed. In the first part, the results and plausibility of the measurements are investigated, where the reflector was moved. In the second part, the effect of antenna inclination was investigated. The field measurements were compared to its respective equivalent *gprMax* simulations.

5-2-1 Part 1: Movement of the Reflector

The measured and simulated radargrams are shown in Figure 5-14. Both radargrams show a distinct hyperbolic shape. The hyperbolas are symmetric. Moreover, both hyperbolas indicate a reflector depth at approximately 1.0 m which is in accord to 0.995 m measured in the field and subsequently implemented into the *gprMax* model. Furthermore, the hyperbolas match a medium velocity of 0.3 m/ns which is in accord to air. The amplitudes of both, the measured and the simulated data are comparable.

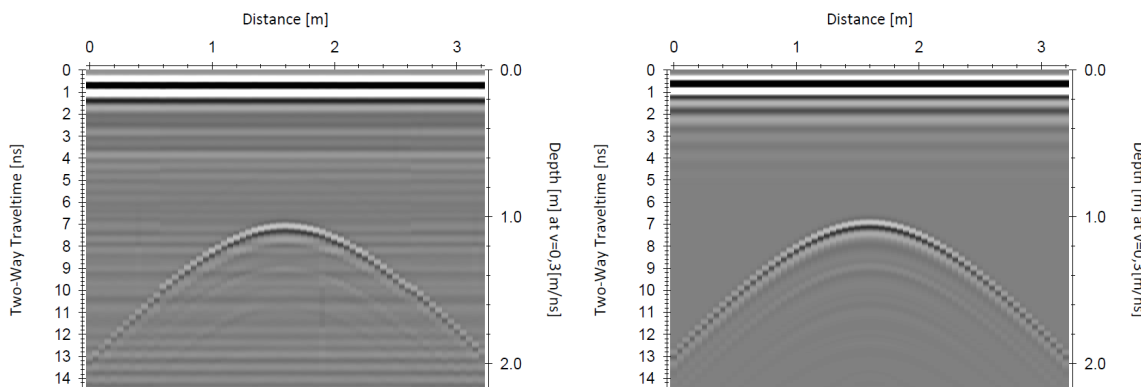


Figure 5-14: Radargrams where the reflector was shifted, Left: Field data, Right: Synthetic data.

However, there are differences between field data and simulated data. There is ringing in the field measurements. In addition, slight variations between the neighbouring traveltimes can be observed in the field measurements. Multiple radargrams from three different separate measurements were merged. Generally, these three parts fit. However little offsets between the individual components are visible, especially in the left part of the radargram where a minor offset exists. Such minor errors may be related to inaccuracies in the positioning of the pipe. Despite these minor errors however, both radargrams show similar trends. No influence of the foamed Polystyrene can be observed. Thus, it can be assumed that the measurement setup does influence the radargrams as well as the following inclination measurements. The first part of the air measurements is only a secondary part of the measurement campaign where it was briefly tested if *gprMax* is capable of resolving the reflection hyperbola and to proof that the foamed Polystyrene does not affect the measurements. The test was successful and the results served their purpose. They are not used for further investigations.

5-2-2 Part 2: Effect of Antenna Inclination

The maximal amplitudes of the measured and simulated data is shown in the polar plots in Figure 5-15 for both antenna orientations. In both orientations, a clear correlation between inclination and energy distribution can be observed. The inclination angle dependence clearly shows that in both antenna orientations, a horizontal antenna position provides the strongest signal. This observation applies for field measurements, as well as the *gprMax* simulations. This observation is also in accord to the radiation patterns from Section 5-1 which also have its maximum directly below the antenna.

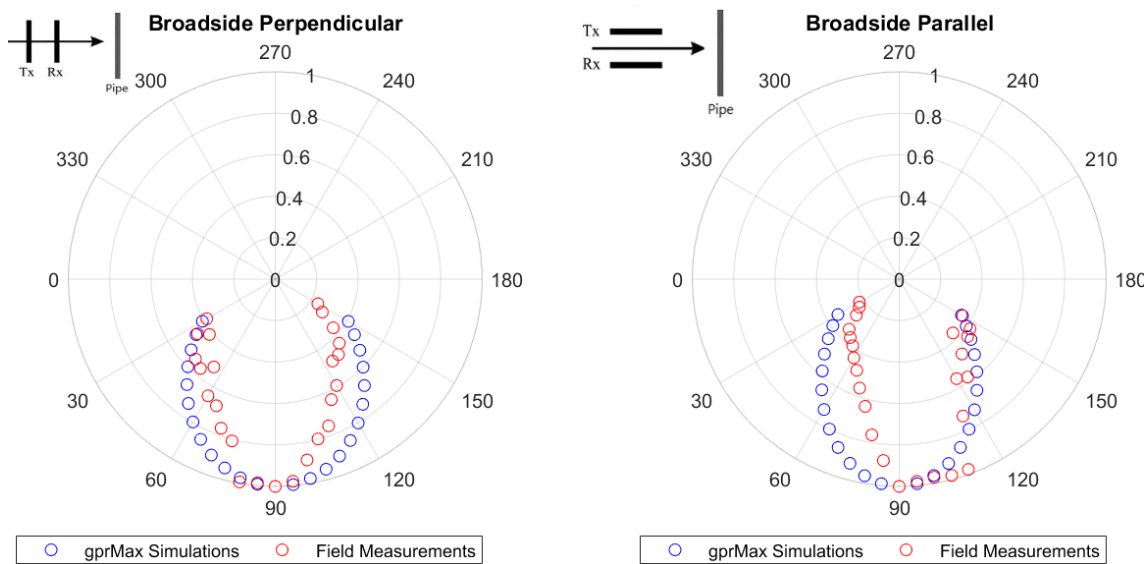


Figure 5-15: Polar plots showing amplitudes at various inclinations from field and synthetic data.

However, there are variations between both, the antenna orientations and the field data to the simulated ones. In terms of orientations, both show a decreasing magnitude at increasing inclinations. However this decrease is slightly stronger in the Broadside-Parallel orientation. This effect can be explained by the polarization characteristics of the antenna. The energy of an antenna is emitted selectively. Most of it is emitted parallel do the antenna's dipole orientation. Thus, more energy can potentially be reflected at an object which is orientated parallel to the antenna dipoles. Therefore, the geometry of the reflector is important as well. A pipe is an elongated feature. When the antenna dipoles are orientated parallel to the pipe, the optimal scenario is given where a maximum of energy is reflected by the pipe even if the antenna is skewed. On the other hand, skewing the antenna in a Broadside-Parallel orientation, where the pipe orientated perpendicular to the antenna dipoles is the worst scenario with a higher loss of energy. Only a fraction of the antenna's energy is emitted in this polarization. Thus, the pipe cannot be measured as efficiently compared to inclinations in the Broadside-Perpendicular orientation. Less energy is reflected by the pipe. Therefore, polarization of the antenna dipoles is relevant to measure reflectors. These observations are expected in the measurements on sand in Section 5-3 too.

The second major observation is the difference between the field and the simulated data. For both orientations, the simulated data show a very smooth and continuous change. The field data on the other hand show a certain plateau at low inclinations. While the antenna remains relatively horizontal, the amplitudes remain similarly strong. After a certain inclination however, a steep sudden decrease of amplitude can be observed which is in sharp contrast to the smooth changes of the simulated data. Part of these variations might be a direct result of the limited precision of the field measurement's inclination adjustments. Errors in inclination angles could have resulted in errors in the respective measurements. Even though human adjustment errors cannot be excluded, it is unlikely that those solely contribute to the observed differences. It is very likely that the observed trends are a direct result of the antenna itself. Thus, it can definitely be said that in general, similar trends can be observed and that *gprMax* models can be used to simulate realistic, inclination dependent scenarios.

5-3 Sand Measurements

In this Section, a more realistic scenario with sand as subsurface material is investigated. The influence of antenna orientation and elevation, as well as inclination parallel and perpendicular to measurement direction was measured and evaluated. Furthermore, the field measurement's setup was transferred into *gprMax* models and subsequently compared to its field measurement equivalent. The Envelopes of field and synthetic data were picked for each hyperbola. Subsequently, the picks belonging to its respective hyperbola arm were plotted against each other to identify asymmetric behaviour. Lastly, quantitative investigations were also included where Cross-Correlations between equivalent traces of the hyperbola's arms were performed to look for potential spatial variations of energy distributions.

5-3-1 Part 1: Horizontal Measurements at various Elevations

In the first part of the sand measurements, the antenna remained horizontally orientated. Here, the effect of antenna orientation and elevation above ground are investigated. Variations between these parameters as well as between field and synthetic data are investigated and discussed.

Main Features

After processing and plotting of the field data, the radargrams were investigated for structures. Exemplary, the main structures observed are marked in the radargrams in Figure 5-16. There are typical structures visible such as the crosstalk. Moreover, a reflection is clearly visible in the radargram which is related to the concrete ground. This feature is continuously measured in every trace. It can also be observed that there are variations in the two-way traveltime. Especially at the end of the measurements line, the two-way traveltime is decreased. This is caused by variations of the sand bulk thickness showing that despite all efforts, no perfectly horizontal surface could be built. However, these topographic differences are not severe.

One major reflection hyperbola can be observed at the position where the pipe was buried. The velocity of the subsurface was determined according to this hyperbola. A velocity of

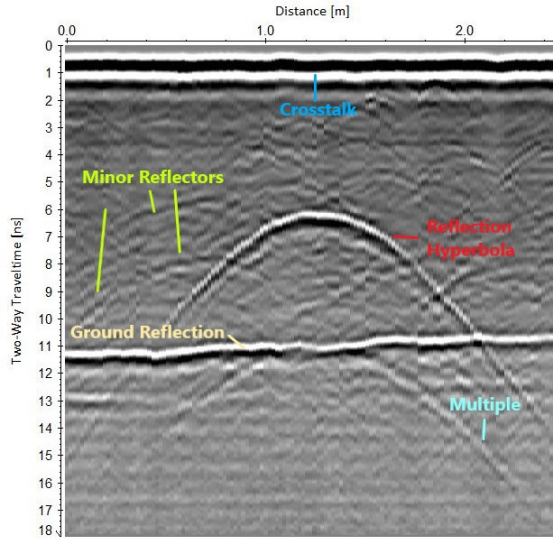


Figure 5-16: Field data radrogram showing main features.

0.186 m/ns was determined. Thus, it can be assumed that the sand has a low permittivity and low water saturation. Laboratory measurements of the sand gave a low ϵ_r of $\approx 2.45 - 2.6$ ($\mu_r = \text{const.}$) which is in accord to eq. 2-13, where such an ϵ_r value provides an only slightly different velocity of ≈ 0.19 m/ns. According to this equation, the field measurement's hyperbola velocity relates to a ϵ_r of 2.6. This is further proving the data's validity. The reflector depth was determined at 55 cm which is in accord to the measured depth in the field. Furthermore, multiples can be observed on some measurements, especially the measurements in Broadside-Perpendicular orientation. Lastly, the field measurements also show various single minor reflectors in the radargrams caused by rocks which are impurities in the sand bulk. They also cause minor reflection hyperbolas, which show similar velocity characteristics as the main pipe reflection.

The numerical measurements generally match the field measurements. However, they are slightly different. Firstly, no ground reflection and no minor reflectors are visible because the PML cells prevent any ground reflection while the subsurface was defined as perfectly homogeneous. Thus, the synthetic data are much cleaner due to the absence of noise and interfering objects. Lastly, the *gprMax* simulations show a better resolution than the field data. This observation is a direct consequence of the measurements setup because the subsurface was defined as perfectly homogeneous and lossless. As a direct consequence, no intrinsic or scattering attenuation occurs in such a model. However, such losses naturally occur in the subsurface. Thus, the synthetic data that did not experience any energy losses shows a greatly increases resolution compared to the field data. In conclusion, field and synthetic data provide a similar outcome while the field data shows higher variations and energy losses due to external and inherent factors which are affecting the measurements. An investigation of the subsurface velocity shows that the analytical solution based on eq. 2-13 matches the estimated velocity in *ReflexW* of 0.19 m/ns.

The Envelopes of the reflection hyperbolas were picked. The picks were split in half into two groups, one for each hyperbola arm. These two groups, which resemble the two hyper-

bola arms, were plotted on top of each other to investigate potential variations between both hyperbola arms, especially to find out if both hyperbola arms are symmetric. The picked envelopes for the Broadside-Perpendicular orientation are shown in Figure 5-17. Both hyperbola arms are identical. The envelopes of both arms increase the nearer the traces are located around the hyperbola apex. Moreover, it can be seen, as already observed in the radargrams, that the field data is much smoother due to the absence of noise, attenuation or scattering. Nonetheless, the symmetric behaviour can also clearly be observed in the much noisier field data.

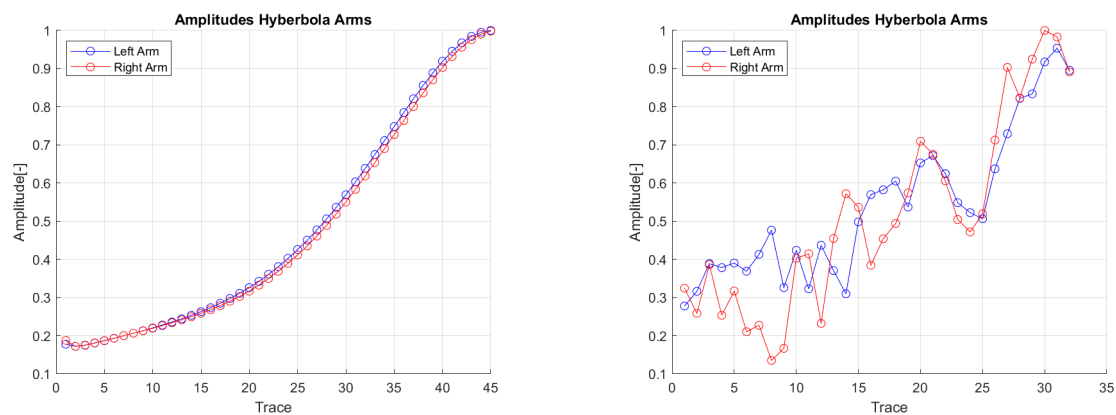


Figure 5-17: Envelopes of synthetic (left) and field data (right) of the horizontal Broadside-Perpendicular measurements ($h = 0 \text{ cm}$).

In addition to the investigations of the Envelopes, Cross-Correlations were also performed between the hyperbola arms to investigate them for similarity. The traces of the picks whose Envelopes were previously plotted on top of each other were cross correlated to investigate them for similarity. Subsequently the Cross-Correlation values were plotted as shown in Appendix Chapter D. Moreover a mean value of all Cross-Correlations was calculated for each measurement. In Table 5-3, the mean of the Cross-Correlation coefficient of each of the hyperbola's arms trace pair is shown. It can be observed that the Cross-Correlation of the synthetic data is around 1 which means that both hyperbola arms are perfectly similar. The field data on the other hand still show very high values, however the noise on the traces diminishes the degree of correlation. Nonetheless, the Cross-Correlation further validates the similarity of both hyperbola arms and therefore a symmetric behaviour.

Influence of Antenna Orientation

The observation are similar to the air measurements in Section 5-2 in terms of antenna orientation. In regard to the pipe reflector, Broadside-Perpendicular shows stronger amplitudes. In proportion, Boradside-Parallel only shows 80% of Broadside-Perpendicular's amplitudes in *gprMax* while the field measurements show generally higher amplitudes as shown in Table 5-1 which summarized the results. This observation is likely related to the presence of noise which may interfere with the energy reflected by the pipe amplifying or attenuating the amount of reflected energy in measured in both antenna orientations. Moreover, it must be kept in mind that the amplitude of reflection hyperbolas is related to orientation and the geometry

of the reflector. While the pipe shows stronger amplitudes in Broadside-Perpendicular orientation, some of the minor reflectors with deviating geometries show stronger amplitudes in Broadside-Parallel orientation. This may also affect the proportion between both orientations amplitudes in the main hyperbola shown in Table 5-1. Lastly, due to the increased amount of energy in Broadside-Perpendicular orientation, multiples are also better visible in these radargrams. These multiples are not visible in the processed field data radargrams because these areas were removed as they are not containing any relevant subsurface information).

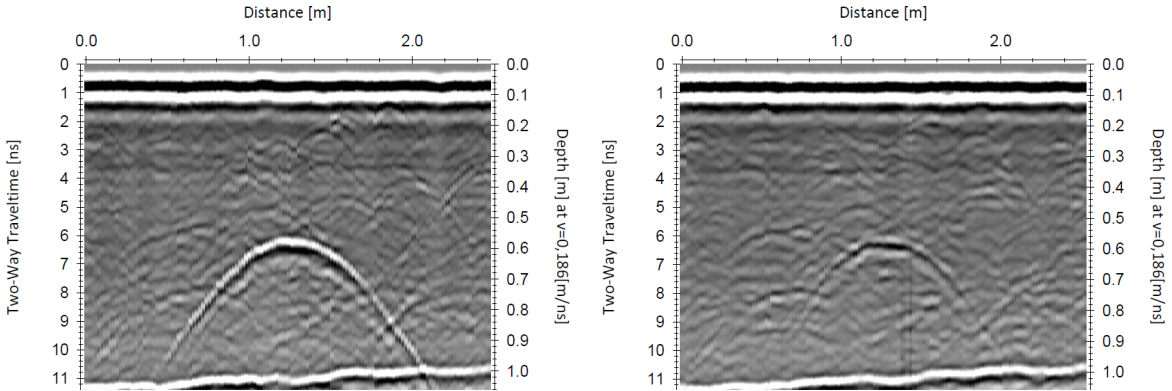


Figure 5-18: Broadside-Perpendicular (left) and Parallel (right), $h = 0$ cm, field data.

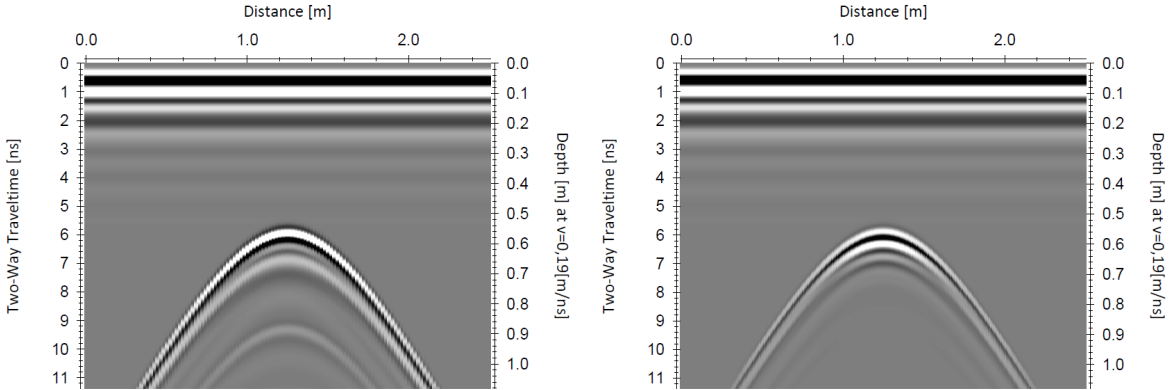


Figure 5-19: Broadside-Perpendicular (left) and Parallel (right), $h = 0$ cm , synthetic data.

Table 5-1: Amplitude proportions between antenna orientations for horizontal measurements.

Elevation	Proportion Perp./Parallel (Field)	Proportion Perp./Parallel (Synthetic)
0 cm	0.90	0.80
8 cm	0.94	0.80
13 cm	0.87	0.80

Similar to the air measurements, antenna polarization play a major again. As already mentioned in the previously, antenna radiate energy selectively. Most of the energy is emitted parallel to the antenna dipole orientation. Therefore, an elongated object which is also orientated parallel to the dipoles reflects a maximum of energy and therefore a better resolution is achieved, especially relative to an object that is orientated perpendicular to the dipoles.

However, the pipe's radius is still relatively high offering enough areas for energy to be reflected. Therefore, the Broadside-Parallel also shows relatively strong reflections despite the fact that the dipoles are aligned perpendicular to the cylinder orientation. However, a decreasing cylinder thickness would likely result into a much poorer resolution of the reflector in this orientation. This observation was already made by [Lualdi and Lombardi, 2014] for example.

Lastly, the envelopes of both antenna orientations are similar and show symmetric behaviour for both, synthetic and field data. In Table 5-1 the Cross-Correlation of both orientations do not indicate any asymmetric behaviour as well. Thus, both orientations have symmetric behaviour validating previous observations. This shows that antenna orientation has no affect on symmetry in this scenario. In conclusion, Broadside-Perpendicular shows better results in this measurement's setup, however results will drastically change if the reflector's geometry and orientation in the subsurface changes which is also indicated by the previously mentioned minor reflectors in the field data.

Influence of Antenna Elevation

The most obvious observation of the measurements where the antenna is elevated is the loss of amplitude. At 13 cm elevation, only 60% of the original amplitude remains in the synthetic data. However, the field data show generally higher amplitudes of approximately 10-15%. This amplitude increase may be caused by the heterogeneities in the sand bulk. Interference effects of the heterogeneities in the subsurface may artificially increase the amplitudes. The results of the amplitude investigations are summarized in Table 5-2.

Table 5-2: Amplitude proportions between antenna elevations for horizontal measurements.

Orientation	0 cm vs. 8 cm		0 cm vs. 13 cm	
	Field	Synthetic	Field	Synthetic
Perp.	0.74	0.60	0.60	0.50
Paralel	0.78	0.60	0.59	0.50

The observation of lower amplitudes is independent of the antenna orientation. At constant orientation, the loss of amplitude remains the same. The radargrams in Figure 5-20 show exemplarily the variations between 0 and 13 cm. In the radargrams where the antenna is elevated, an air reflection can be observed which already indicated that less energy is emitted into the subsurface. Due to a decrease of emitted energy into the ground, the hyperbolas are not as well resolved as in the measurements where the antenna is located directly on the ground. In addition, the velocity is increased from 0.186 to 0.2 m/ns in the field data and from 0.19 to 0.204 in the synthetic data. This increase is a direct consequence of the insertion of air as a high velocity layer increasing the mean velocity. Moreover, a higher object depth is the direct consequence which correlates to the respective antenna elevation. In addition, the velocities were also calculated via the layers slownesses s_1 and s_2 [s/m] which are the reciprocal of velocity v [m/s] and the layers respective portion h_1 and h_2 [m] of the entire thickness between antenna and reflector h_{1+2} . The slowness based on the subsurface's and the air velocity were performed according to the following equation:

$$s_{total} = \frac{1}{v_n} = \frac{h_1}{h_{1+2}} s_1 + \frac{h_2}{h_{1+2}} s_2. \quad (5-1)$$

The acquired slownesses or velocities correlate well with the measured velocities in *ReflexW*. The results of the velocity investigations are summarized in Table 5-3. The hyperbola itself remains symmetric which is proven by Envelope and Cross-Correlation investigations as shown in the plots Appendix Chapter D. It can be concluded that antenna elevation alone does not affect hyperbola symmetry.

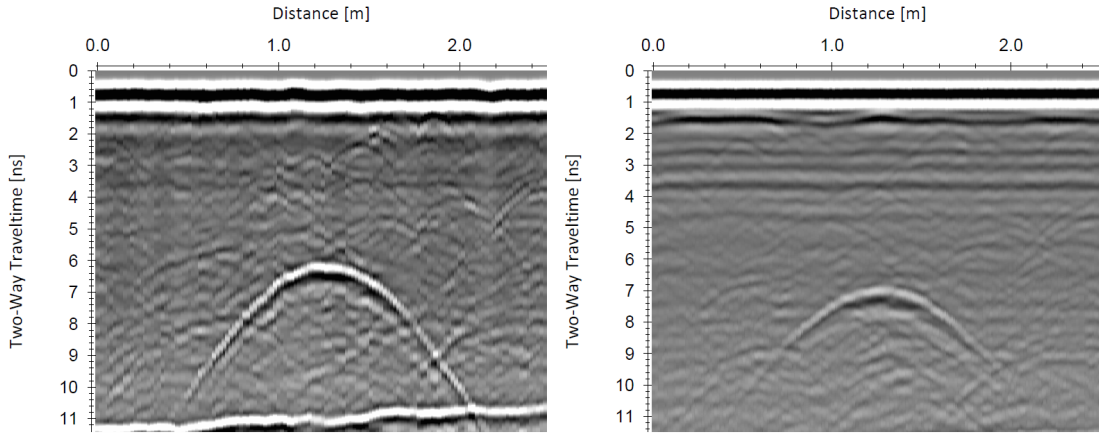


Figure 5-20: Field data of horizontal measurements at 0 cm (left) and 13 cm (right).

Table 5-3: Summarized results of the horizontal and elevation measurements.

Field Data	Elevation	Orientation	v [m/ns]	Cross-Correlation
	0 cm	Broadside-Perpendicular	0.186	0.798
		Broadside-Parallel	0.186	0.808
	8 cm	Broadside-Perpendicular	0.195	0.820
		Broadside-Parallel	0.195	0.770
	13 cm	Broadside-Perpendicular	0.2	0.813
		Broadside-Parallel	0.2	0.790
gprMax Data	Elevation	Orientation	v [m/ns]	Cross-Correlation
	0 cm	Broadside-Perpendicular	0.19	1
		Broadside-Parallel	0.19	1
	8 cm	Broadside-Perpendicular	0.2	1
		Broadside-Parallel	0.2	1
	13 cm	Broadside-Perpendicular	0.204	1
		Broadside-Parallel	0.204	1

5-3-2 Part 2: Measurements at various Inclinations

In the second part of the measurements on sand, the effects of antenna inclination are investigated. A comparison between inclination angles and direction is discussed. Moreover, the effects on the reflection hyperbolas are investigated.

Influence of Inclination Angle

The influence of the inclination angle is evident in all radargrams which include inclinations. First, higher inclination angles decrease amplitudes. Moreover, there is a slight velocity increase due to the insertion of air between antenna and ground. Similar to the horizontal measurements, the synthetic *gprMax* data are much cleaner than the field data. The hyperbola shape depends on inclination direction which is further shown in the following Section. The hyperbola's outer parts are not as well resolved in field data as in the synthetic *gprMax* data which is observable in both inclination directions. Generally the Broadside-Parallel orientation appears to be more affected. This observation is similar to the observations made in the horizontal measurements where it is assumed that the field data is poorer resolved due to attenuation in the subsurface.

Influence of Inclination Direction

It is highly important for the measurements, in which direction the antenna is inclined. In the Inline measurements, where the antenna is inclined parallel to the measurement direction, the reflection hyperbolas show asymmetric behaviour. Therefore, no velocity estimation could be done in *ReflexW*. The hyperbola arms show very different amplitudes. Higher inclinations increase this effect. At 30°, the field data were barely pickable because the reflection was below noise level. In the inline radargram shown in Figure 5-21, left arm is much weaker resolved. In comparison to the synthetic data, the field data is poorer resolved again. As already mentioned previously, this observation is related to attenuation in the field data while the subsurface of the synthetic data is per model definition lossless.

In Figure 5-22, the envelopes of the Inline measurements hyperbola arms are shown. A clear shift of the hyperbola apex can be observed, especially in the noiseless *gprMax* data. The Cross-Correlation value shown in Table 5-4 indicate variations in the amplitudes as well. However, the Cross-Correlation values are only slightly decreased. This observation may be related to the presence of noise. The noise appears to have a smoothing effect. In the horizontal measurements, where the Cross-Correlation is supposed to be maximal, noise diminishes the correlation coefficients. On the other hand, traces where the reflection amplitudes are relatively weak, especially at the outer parts of the hyperbolas, the noise has a higher influence on the correlation coefficient than the reflection itself due to its higher presence relative to the reflection energy. Thus, it tends to overprint the amplitudes affecting the correlation coefficients making the correlation to appear higher. In the noiseless synthetic data on the other hand, a relatively low Cross-Correlation at the outer parts of the hyperbole can be observed which increases towards the central traces as shown for example, in Figure D-7 in the Appendix.

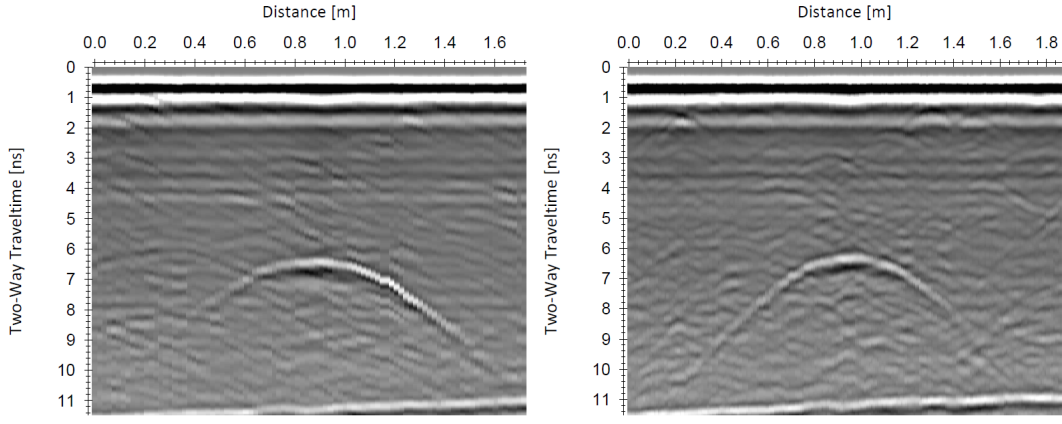


Figure 5-21: Field data of the 30° inclination measurements, Left: Inline, Right: Crossline.

In the Crossline measurements, the reflection hyperbola remains symmetric. However, the amplitudes are weaker compared to the horizontal measurements, an observation which was already made in the comparison of antenna elevation (see Figure 5-20). And analogously, this is related to a slight elevation of the antennas above ground as a direct result of the tilt. The elevation caused by the inclination however is much smaller compared to the horizontal measurements. Thus, the velocity increase is smaller. It can be observed that the antenna orientation influence velocities because the distance between transmitter and receiver to air can change due to the antenna geometry. In the Broadside-Parallel orientation the distance of the transmitter and receiver to the ground is increased and therefore, the velocities slightly higher than in Broadside-Perpendicular orientation. Therefore, in the Broadside-Parallel orientation slightly higher velocities can be observed. Cross-Correlations of amplitudes and envelopes also indicate symmetric behaviour as shown in Table 5-4 and Figure 5-23. Their behaviour is similar to the measurements in horizontal position.

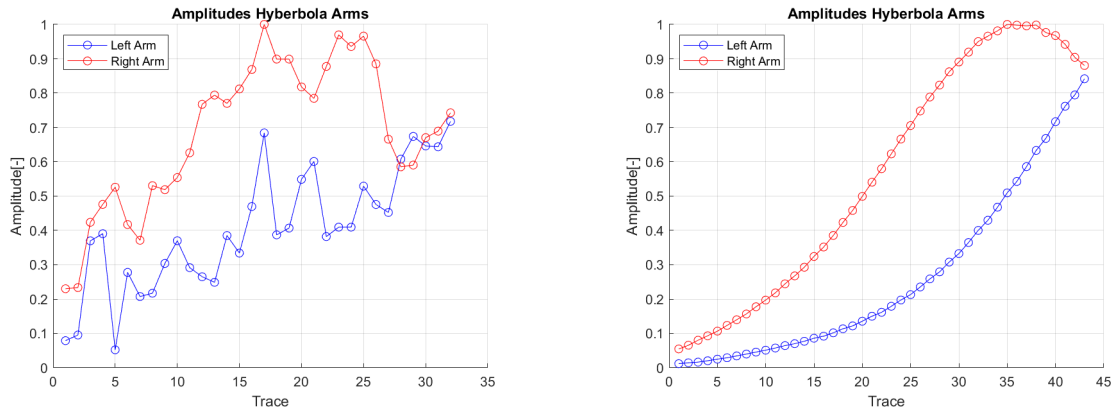


Figure 5-22: Envelopes of the 30° Inline measurements (Broadside-Perpendicular), Left: Field data, Right: Synthetic data.

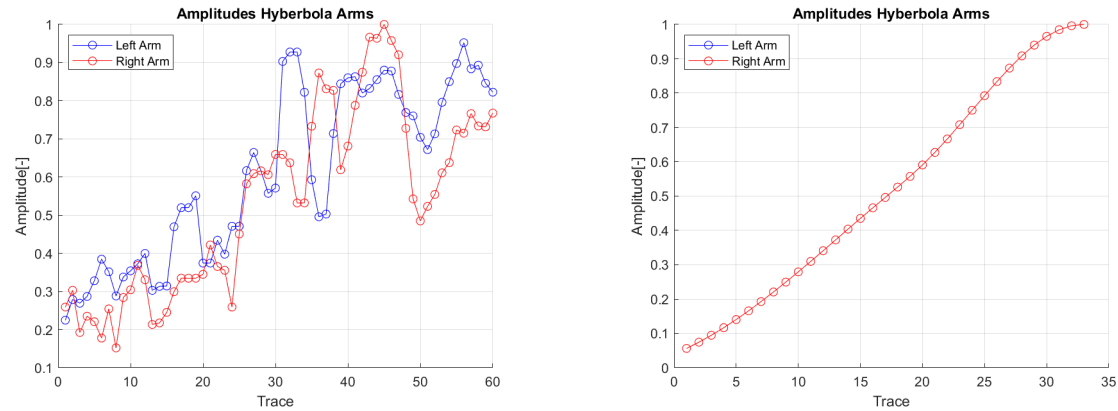


Figure 5-23: Envelopes of the 30° Crossline Measurements (Broadside-Perpendicular), Left: Field data, Right: Synthetic data.

Table 5-4: Summarized results of the inclination measurements.

Field Data	Inclination	Orientation	v [m/ns]	Cross-Correlation
Inline	15°	Broadside-Perpendicular	-	0.718
		Broadside-Parallel	-	0.761
Inline	30°	Broadside-Perpendicular	-	0.764
		Broadside-Parallel	-	0.726
Crossline	15°	Broadside-Perpendicular	0.188	0.770
		Broadside-Parallel	0.189	0.798
Crossline	30°	Broadside-Perpendicular	0.190	0.821
		Broadside-Parallel	0.191	0.786
gprMax Data	Inclination	Orientation	v [m/ns]	Cross-Correlation
Inline	15°	Broadside-Perpendicular	-	0.968
		Broadside-Parallel	-	0.977
Inline	30°	Broadside-Perpendicular	-	0.839
		Broadside-Parallel	-	0.828
Crossline	15°	Broadside-Perpendicular	0.198	1
		Broadside-Parallel	0.2	1
Crossline	30°	Broadside-Perpendicular	0.2	1
		Broadside-Parallel	0.204	1

Chapter 6

Conclusion and Outlook

The main objective of this research was the investigation of the radiation characteristics of **GPR** antennas at varying degrees of inclination and elevation, factors which are commonly occurring and governing factors in field measurements but are barely investigated yet. This thesis ought to provide more insight on the influence these factors via field measurements in controlled environments and numerical **FDTD** simulations in *gprMax*. A comparison of field and synthetic data is used to study the accuracy of numerical simulations of various scenarios involving the detection of buried objects.

To answer these questions, radiation patterns of the Hertzian Dipole and the 1.5 GHz GSSI Antenna were acquired in *gprMax* and compared to analytical solutions. Moreover, field measurements were performed in air and sand at various inclination directions, angles and elevations. These field setups were subsequently implemented into *gprMax* and the numerical results compared to the field data. In the air measurements, the amplitudes measured at various inclinations were measured and variations between field and numerical results discussed. For the measurements in sand, envelopes were picked and Cross-Correlations applied to investigate the shape of the reflection hyperbola. Moreover, velocity investigations were performed.

The investigation radiation patterns show that for the Hertzian Dipole in full space, the numerical solutions match the analytical solution. However, numerical patterns show variations to analytical solutions in half-space. These variations are probably related to near-field effects which were not incorporated into analytical solutions. There are clear variations between patterns of the Hertzian Dipole and the 1.5 GHz GSSI Antenna Model. These variations are mainly caused by the antenna's shielding which focuses most of the energy into the subsurface. For both sources, elevations decrease the amount of energy transmitted into the ground.

gprMax simulations and field measurements show similar results. Globally, numerical measurements show higher amplitudes which is related to the predefined lossless behaviour of the subsurface. The field data show higher variations due to the presence of noise and heterogeneities in the subsurface. These are responsible for intrinsic attenuation and scattering of **EM** waves. The inclination angle as well as inclination direction affect measurements. Inclinations in measurement line result in asymmetric reflection hyperbolas while inclinations

perpendicular to measurement direction only results into decreased amplitudes. Higher elevations, but also inclinations in general decrease amplitudes due to poorer ground coupling which results into increasing energy emissions into the air. The best results are achieved with no inclination and direct antenna-ground contact. Moreover, the antenna configuration influences the measurements too which however heavily depends the reflector's geometry.

All things considered, *gprMax* can provide good results which are comparable to the measured field data. The simulations can be performed relatively fast with access to computational resources which makes *gprMax* a handy and time efficient tool to simulate real life scenarios that also involve landmines and [IEDs](#). However, the simulations results rely on accurate subsurface information to provide useful results. Thus, acquiring subsurface characteristics from areas of interest (e.g. typical soils in conflict areas) are necessary as input data.

By understanding the radiation characteristics of [GPR](#) antennas, survey techniques can potentially be improved in order to detect targets more efficiently. Despite the findings presented in this work however, more research is needed. The findings of this research are solely based on a very simplified reflector geometry, homogeneous, lossless subsurfaces and ideal relations between reflector and antenna orientations. Therefore, future research needs to add an extra level of model complexity. Simulations with other soils, more sophisticated reflectors geometries and antennas are relevant for the development of more realistic models.

For future investigations, it would be sensible to add a lossy and inhomogeneous subsurface. The introduction of noise and heterogeneties are great improvements for more realistic subsurface investigations. Investigations of other targets geometries ([IEDs](#), landmines, explosives etc.) are the logical next step. Moreover, reflectors may also be buried in other non-horizontal positions. In addition, the effect of subsurface disturbances around buried objects due to digging for example may be incorporated as well. Furthermore, including topography and vegetation would further increase the level of realism. Lastly, other antenna orientations such as the cross-side and end-fire orientation could potentially be used for investigations. Other antenna orientations may improve detectability of buried reflectors depending of their geometry.

Bibliography

- [Annan, 2009] Annan, P. (2009). *Chapter 1. Electromagnetic Principles of Ground Penetrating Radar*, pages 1–40.
- [Balanis, 1989] Balanis, C. A. (1989). *Advanced Engineering Electromagnetics*. John Wiley and Sons, New York.
- [Benedetto et al., 2016] Benedetto, A., Tosti, F., Bianchini Ciampoli, L., and D’Amico, F. (2016). An overview of ground-penetrating radar signal processing techniques for road inspections. *Signal Processing*, 132.
- [Billings, 2004] Billings, S. (2004). Discrimination and classification of buried unexploded ordnance using magnetometry. *Geoscience and Remote Sensing, IEEE Transactions on*, 42:1241 – 1251.
- [Brunzell, 1999] Brunzell, H. (1999). Detection of shallowly buried objects using impulse radar. *Geoscience and Remote Sensing, IEEE Transactions on*, 37:875 – 886.
- [BSSA, 2021] BSSA (2021). Magnetic properties of austenitic stainless steels. Link: https://bssa.org.uk/bssa_articles/magnetic-properties-of-austenitic-stainless-steels/, retrieved: 2011-08-03.
- [Chen et al., 2004] Chen, L., Ong, C., Neo, C., Varadan, V., and Varadan, V. (2004). *Microwave Electronics: Measurement and Materials Characterization*. Wiley.
- [Chung, 2001] Chung, D. (2001). Applied materials science : Applications of engineering materials in structural, electronics, thermal, and other industries / d.d.l. chung.
- [Cirillo et al., 2001] Cirillo, L., Brown, C., and Zoubir, A. (2001). Polynomial phase signal based detection of buried landmines using ground penetrating radar. In *Proceedings of the 11th IEEE Signal Processing Workshop on Statistical Signal Processing (Cat. No.01TH8563)*, pages 166–169.
- [Daniels, 2004] Daniels, D. (2004). *Ground Penetrating Radar, 2nd Edition*. Institution of Electrical Engineers, UK.

- [Daniels, 2006] Daniels, D. (2006). A review of gpr for landmine detection. *Sensing and Imaging*, 7:90–123.
- [Das, 2006] Das, Y. (2006). Effects of soil electromagnetic properties on metal detectors. *Geoscience and Remote Sensing, IEEE Transactions on*, 44:1444 – 1453.
- [DHS, 2006] DHS (2006). Improvised explosive devices, a fact sheet from the national academies and the department of homeland security. Link: https://www.dhs.gov/xlibrary/assets/prep_ied_fact_sheet.pdf, retrieved: 2021-09-03.
- [Diamanti and Annan, 2013] Diamanti, N. and Annan, P. (2013). Characterizing the energy distribution around gpr antennas. *Journal of Applied Geophysics*, 99:83–90.
- [Diamanti et al., 2012] Diamanti, N., Annan, P., and J.D., R. (2012). Quantifying gpr responses. *2012 14th International Conference on Ground Penetrating Radar, GPR 2012*.
- [Engheta et al., 1983] Engheta, N., Papas, C., and Elachi, C. (1983). Radiation patterns of interfacial dipole antennas. *Radio Science*, 17.
- [Foounten, 2018] Foounten, I. (2018). Explosive remnants of war in post revolution libya un photo. Link: <https://www.undispatch.com/podcast-big-data-can-teach-us-terrorism/>, retrieved: 2021-09-03.
- [Gedney, 2011] Gedney, S. (2011). Introduction to the finite-difference time-domain (fdtd) method for electromagnetics. *Synthesis Lectures on Computational Electromagnetics*, 6.
- [GeoSci, 2018a] GeoSci (2015-2018a). Dielectric permittivity. Link: https://em.geosci.xyz/content/physical_properties/dielectric_permittivity/index.html, retrieved: 2011-08-03.
- [GeoSci, 2018b] GeoSci (2015-2018b). Ground penetrating radar. Link: https://em.geosci.xyz/content/geophysical_surveys/gpr/index.html#gpr-index, retrieved: 2011-08-03.
- [GeoSci, 2018c] GeoSci (2015-2018c). Typical values for rocks and other materials. Link: https://em.geosci.xyz/content/physical_properties/dielectric_permittivity/dielectric_permittivity_values.html#dielectric-permittivity-values, retrieved: 2011-08-03.
- [Giannakis et al., 2019] Giannakis, I., Giannopoulos, A., and Warren, C. (2019). Realistic FDTD GPR antenna models optimized using a novel linear/nonlinear full-waveform inversion. *IEEE Trans. Geosci. Remote. Sens.*, 57(3):1768–1778.
- [Giannopoulos, 2012] Giannopoulos, A. (2012). Unsplit implementation of higher order pmls. *IEEE Transactions on Antennas and Propagation*, 60(3):1479–1485.
- [Glisson, 1989] Glisson, A. (1989). Advanced engineering electromagnetics, by constantine a. balanis [book review]. *IEEE Antennas and Propagation Magazine - IEEE ANTENNAS PROPAG MAG*, 31.
- [Greiner, 1998] Greiner, W. (1998). *Classical Electrodynamics*. Springer.

- [Grimm et al., 2017] Grimm, R., Stillman, D., Dinwiddie, C., McGinnis, R., and Sandberg, S. (2017). On conductive ground: 'analysis of bistatic sounding of the deep subsurface with ground penetrating radar – experimental validation' by v ciarletti et al. *Planetary and Space Science*, 139:51–56.
- [Guelle et al., 2003] Guelle, D., Smith, A., Lewis, A., and Bloodworth, T. (2003). *Metal Detector Handbook for Humanitarian Demining*. Office for Official Publications of the European Communities.
- [Hildebrand, 1968] Hildebrand, F. (1968). Finite - difference equations and simulations.
- [Hussein and Waller, 2000] Hussein, E. and Waller, E. (2000). Landmine detection: the problem and the challenge. *Applied Radiation and Isotopes*, 53(4):557–563.
- [ICBL-CMC, 2019] ICBL-CMC (2019). *Landmine Monitor 2019, 21st Annual Edition*. International Campaign to Ban Landmines – Cluster Munition Coalition (ICBL-CMC).
- [ICBL-CMC, 2020] ICBL-CMC (2020). *Landmine Monitor 2020, 22nd Annual Edition*. International Campaign to Ban Landmines – Cluster Munition Coalition (ICBL-CMC).
- [IEEE, 1983] IEEE (1983). Ieee standard definitions of terms for antennas. *IEEE Std 145-1983*, pages 1–31.
- [ISSF, 2021] ISSF (2021). Stainless steel in figures 2021. Link: https://www.worldstainless.org/files/issf/non-image-files/PDF/ISSF_Stainless_Steel_in_Figures_2021_English_public_version.pdf, retrieved: 2011-08-03.
- [Jol, 2009] Jol, H. (2009). *Ground Penetrating Radar: Theory and Applications*, page 524. Elsevier.
- [Kara and Gebrehiwot, 2009] Kara, H. and Gebrehiwot, E. (2009). Economics of landmines and demining. Master's thesis, Naval Postgraduate School.
- [Kasban et al., 2010] Kasban, H., Zahran, O., Elaraby, S., Kordy, M., and Abd El-Samie, F. (2010). A comparative study of landmine detection techniques. *Sensing and Imaging: An International Journal*, 11:89–112.
- [Knödel et al., 2007] Knödel, K., Lange, G., and Voigt, H.-J. (2007). *Environmental Geology: Handbook of Field Methods and Case Studies*. Bundesanstalt für Geowissenschaften Rohstoffe (BGR).
- [Kovac, 2001] Kovac, J. (2001). The big bang: A history of explosives (brown, g.i.). *Journal of Chemical Education*, 78(1):36.
- [Kunz and Luebbers, 1993] Kunz, K. and Luebbers, R. J. (1993). *The Finite Difference Time Domain Method for Electromagnetics*. CRC Press.
- [Lazzi et al., 1998] Lazzi, G., Patnaik, S., Furse, C., and Gandhi, O. (1998). Comparison of fdtd computed and measured radiation patterns of commercial mobile telephones in presence of the human head. *Antennas and Propagation, IEEE Transactions on*, 46:943 – 944.

- [LIAG, 2013] LIAG (2013). Soil influence on sensor-based landmine detection. Link: <https://www.leibniz-liag.de/en/research/projects/terminated-projects-third-party-funded-soil-influence-on-sensor-based-landmine-detection.html.html>, retrieved: 2021-09-03.
- [LIAG, 2021] LIAG (2021). Counter-ied 3 project. Link: <https://www.leibniz-liag.de/en/research/projects/third-party-funded-projects/counter-ied-2-1.html>, retrieved: 2021-09-03.
- [Loewer, 2018] Loewer, M. (2018). *On the frequency-dependence of electrical soil properties and their influence on ground-penetrating radar*. Doctoral thesis, Technische Universität Berlin, Berlin.
- [Loewer et al., 2015] Loewer, M., Igel, J., and Wagner, N. (2015). Spectral decomposition of soil electrical and dielectric losses and prediction of in situ gpr performance. *Selected Topics in Applied Earth Observations and Remote Sensing, IEEE Journal of*, PP:1–9.
- [Lopera and Milisavljevic, 2007] Lopera, O. and Milisavljevic, N. (2007). Prediction of the effects of soil and target properties on the antipersonnel landmine detection performance of ground-penetrating radar: A colombian case study. *Journal of Applied Geophysics*, 63:13–23.
- [Lualdi and Lombardi, 2014] Lualdi, M. and Lombardi, F. (2014). Significance of gpr polarisation for improving target detection and characterisation. *Nondestructive Testing and Evaluation*, 29.
- [Mansoor, 2018] Mansoor, P. (2018). Improvised explosive device. Link: <https://www.britannica.com/technology/improvised-explosive-device>, retrieved: 2021-09-03.
- [Meng et al., 2019] Meng, X., Xu, Y., Xiao, L., Dang, Y., Zhu, P., Tang, C., Zhang, X., Liu, B., Gou, S., and Yue, Z. (2019). Ground-penetrating radar measurements of subsurface structures of lacustrine sediments in the qaidam basin (nw china): Possible implications for future in-situ radar experiments on mars. *Icarus*, 338:113576.
- [Muhammad and Umar, 2013] Muhammad, U. and Umar, S. (2013). Experimental performance investigations and evaluation of base metals thermocouples.
- [Okman, 2005] Okman, O. (2005). *Free Forming OF Locally Induction Heated Specimens*. PhD thesis.
- [Olhoeft, 1998] Olhoeft, G. (1998). Electrical, magnetic, and geometric properties that determine ground penetrating radar performance. pages 177–182.
- [Olhoeft, 2003] Olhoeft, G. (2003). Electromagnetic field and material properties in ground penetrating radar. pages 144 – 147.
- [Oßberger et al., 2006] Oßberger, G., Thomas, B., Schimbäck, E., Pfeil, R., Stelzer, A., and Weigel, R. (2006). Adaptive ground clutter removal algorithm for ground penetrating radar applications in harsh environments. *Sensing and Imaging*, 7:71–89.

- [O'Neill, 2017] O'Neill, K. (2017). Discrimination of subsurface unexploded ordnance. *SPIE Newsroom*.
- [Pasion, 2007] Pasion, L. (2007). *Inversion of time domain electromagnetic data for the detection of unexploded ordnance*. PhD thesis, University of British Columbia.
- [Poljak and Cvetković, 2019] Poljak, D. and Cvetković, M. (2019). *Human Interaction with Electromagnetic Fields*. Academic Press.
- [Porsani et al., 2010] Porsani, J. L., Slob, E., Lima, R. S., and Leite, D. N. (2010). Comparing detection and location performance of perpendicular and parallel broadside gpr antenna orientations. *Journal of Applied Geophysics*, 70(1):1–8.
- [Poynting, 1884] Poynting, J. H. (1884). On the transfer of energy in the electromagnetic field. *Philosophical Transactions of the Royal Society of London*, 175:343–361.
- [Smith, 1984] Smith, G. (1984). Directive properties of antennas for transmission into a material half-space. *Antennas and Propagation, IEEE Transactions on*, 32:232 – 246.
- [Smith, 2007] Smith, M. (2007). A chinese type 59 metallic anti-tank mine main battle tank on display at the beijing military museum. Link: https://de.wikipedia.org/wiki/Datei:Type_59_anti-tank_mine.jpg, retrieved: 2021-09-03.
- [Stadler and Igel, 2018] Stadler, S. and Igel, J. (2018). A numerical study on using guided gpr waves along metallic cylinders in boreholes for permittivity sounding. *17th International Conference on Ground Penetrating Radar (GPR)*, pages 1–4.
- [Taflove, 1995] Taflove, A. (1995). *Computation Electrodynamics—The Finite-Difference Time-Domain Method*. Artech House Publishers.
- [Taflove and Brodwin, 1975] Taflove, A. and Brodwin, M. (1975). Numerical solution of steady-state electromagnetic scattering problems using the time-dependent maxwell's equations. *IEEE Transactions on Microwave Theory and Techniques*, 23(8):623–630.
- [Takahashi et al., 2011] Takahashi, K., Preetz, H., and Igel, J. (2011). Soil properties and performance of landmine detection by metal detector and ground-penetrating radar — soil characterisation and its verification by a field test. *Journal of Applied Geophysics - J APPL GEOPHYS*, 73:368–377.
- [Tesfamariam, 2013] Tesfamariam, G. T. (2013). *Signal Processing Techniques for Landmine Detection Using Impulse Ground Penetrating Radar (ImGPR)*. PhD thesis, TU Darmstadt.
- [Walsh, 1991] Walsh, F. (1991). Electrode reactions in metal finishing. *Transactions of the Institute of Metal Finishing*, 69:107–111.
- [Warren, 2009] Warren, C. (2009). *Numerical modelling of high-frequency ground-penetrating radar antennas*. PhD thesis, The University of Edinburgh.
- [Warren and Giannopoulos, 2011] Warren, C. and Giannopoulos, A. (2011). Creating finite-difference time-domain models of commercial ground-penetrating radar antennas using taguchi's optimization method. *Geophysics*, 76:G37–G47.

- [Warren and Giannopoulos, 2016] Warren, C. and Giannopoulos, A. (2016). Characterisation of a ground penetrating radar antenna in lossless homogeneous and lossy heterogeneous environments. *Signal Processing*, 132.
- [Warren et al., 2016] Warren, C., Giannopoulos, A., and Giannakis, I. (2016). gprmax: Open source software to simulate electromagnetic wave propagation for ground penetrating radar. *Computer Physics Communications*, 209.
- [Wilson, 2007] Wilson, C. (2007). Improvised explosive devices (IEDs) in Iraq and Afghanistan: Effects and countermeasures. page 7.
- [Wu et al., 2018] Wu, H., Wang, J., Wang, C., and Wang, J. (2018). Soil-water-structure interaction algorithm in smoothed particle hydrodynamics (SPH) with application to deep-penetrating problems. *International Journal of Computational Methods*, 17.
- [Yee, 1966] Yee, K. (1966). Numerical solution of initial boundary value problem involving Maxwell's equations in isotropic media. *IEEE Trans. Antennas and Propagation*, AP-14:302–307.

Appendix A

Additional Radiation Patterns

A-1 Far Field Patterns

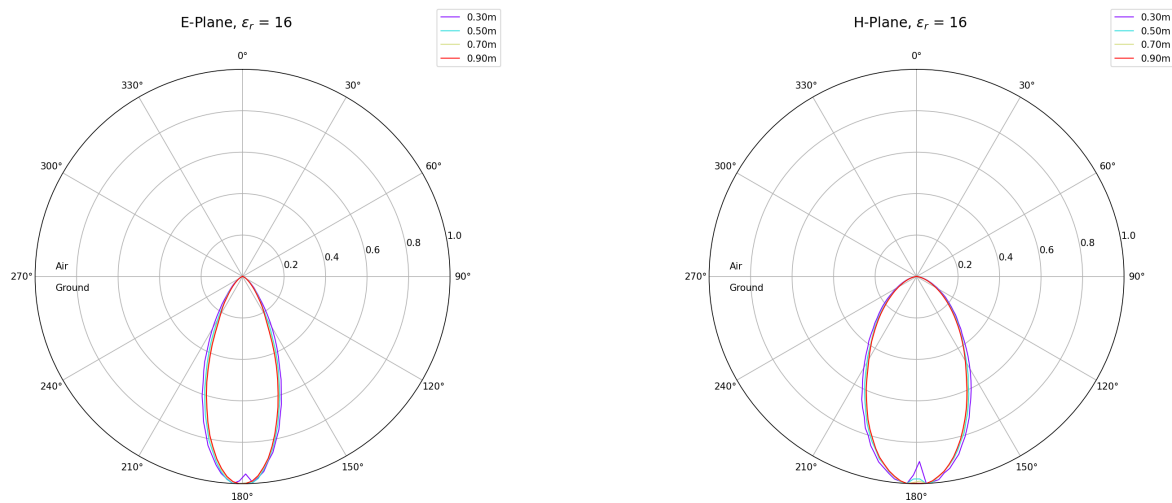


Figure A-1: Antenna radiation patterns for far-field investigations in half space ($\epsilon_r = 16$).

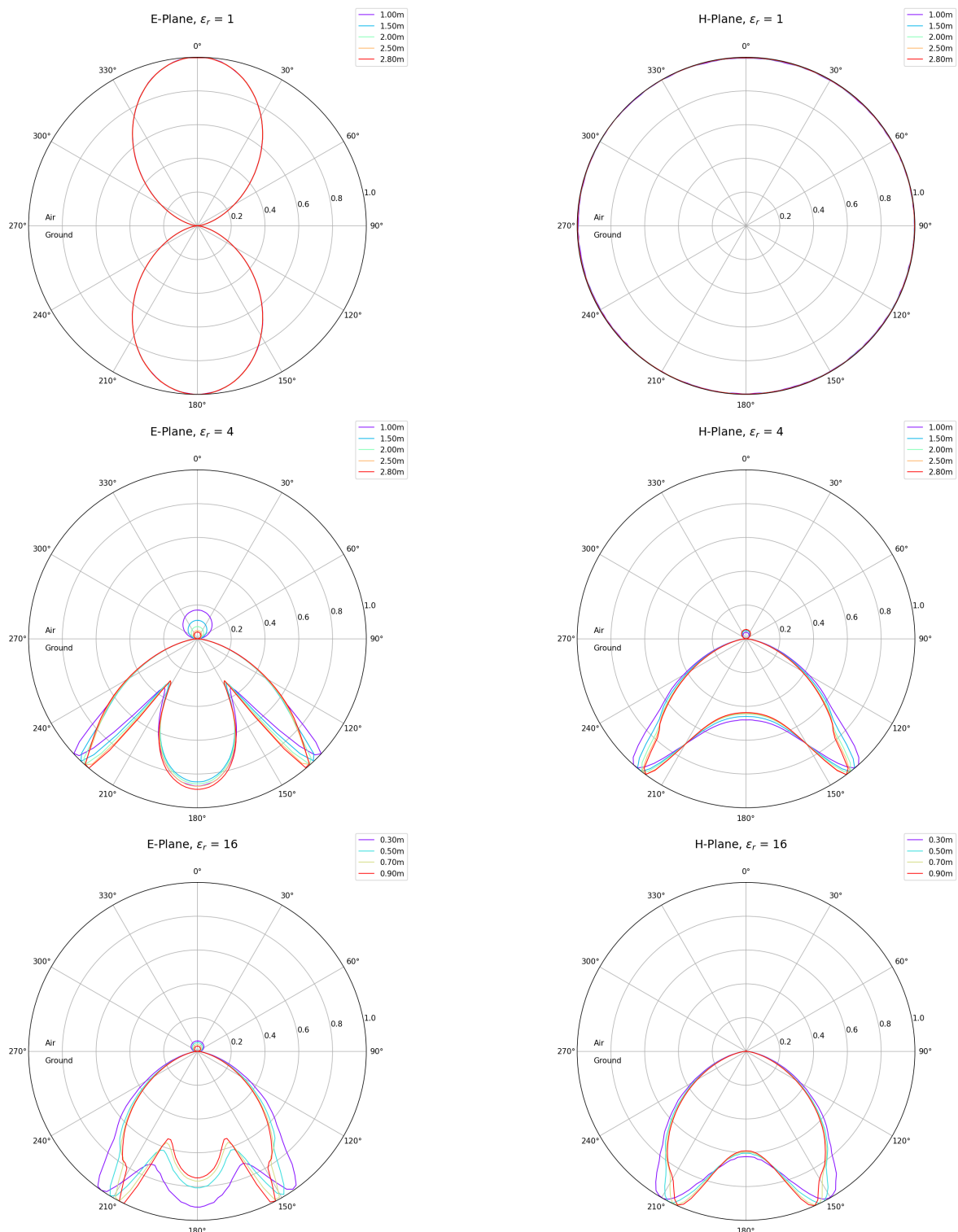


Figure A-2: Antenna radiation patterns for far-field investigations in half space (top: $\epsilon_r = 1$, middle: $\epsilon_r = 4$, bottom: $\epsilon_r = 16$).

A-2 Hertzian Dipole Patterns

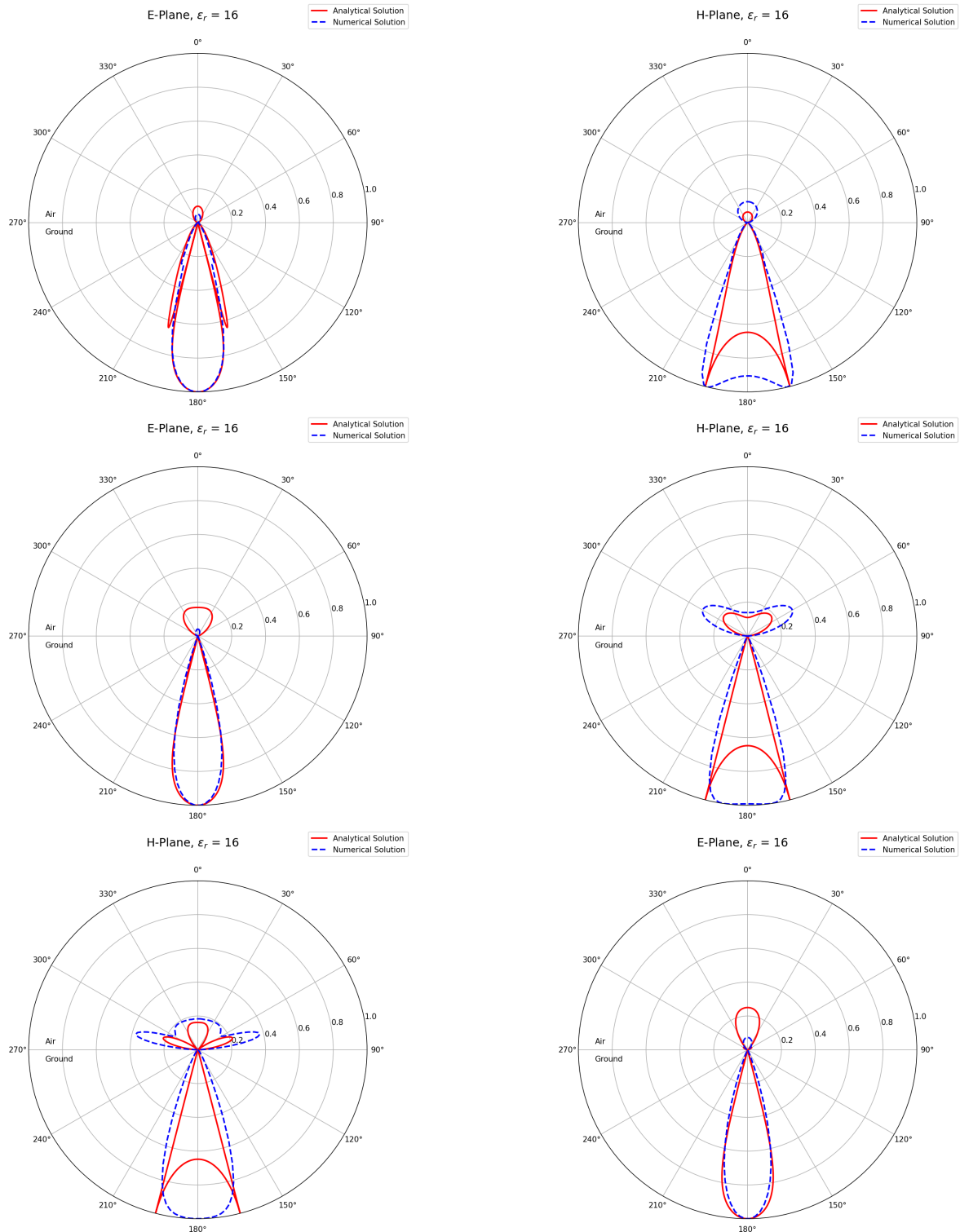


Figure A-3: Hertzian Dipole (elevated), $\epsilon_r = 16$ (top: 2 cm, middle: 7 cm, bottom: 15 cm).

A-3 Antenna Patterns

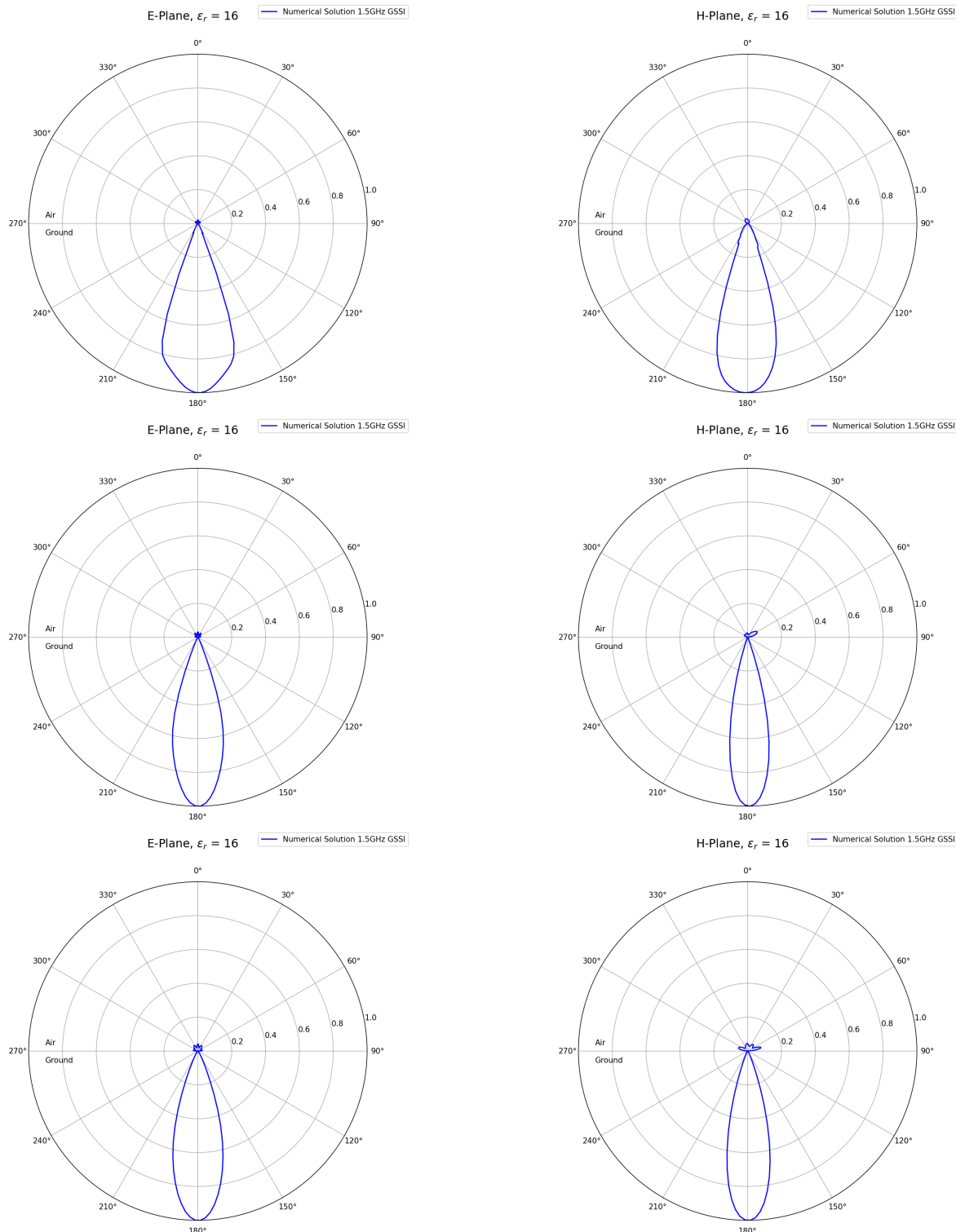


Figure A-4: Antenna patterns (elevated), $\epsilon_r = 16$ (top: 2 cm, middle: 7 cm, bottom: 15 cm).

Appendix B

Additional Radargrams

B-1 Horizontal Measurements

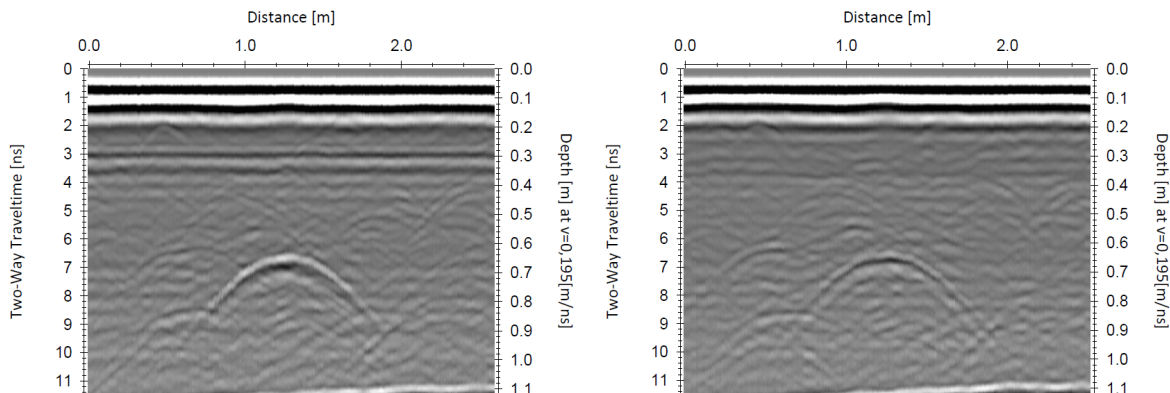


Figure B-1: Broadside-Perpendicular (left) and Parallel (right), $h = 8\text{ cm}$, field data.

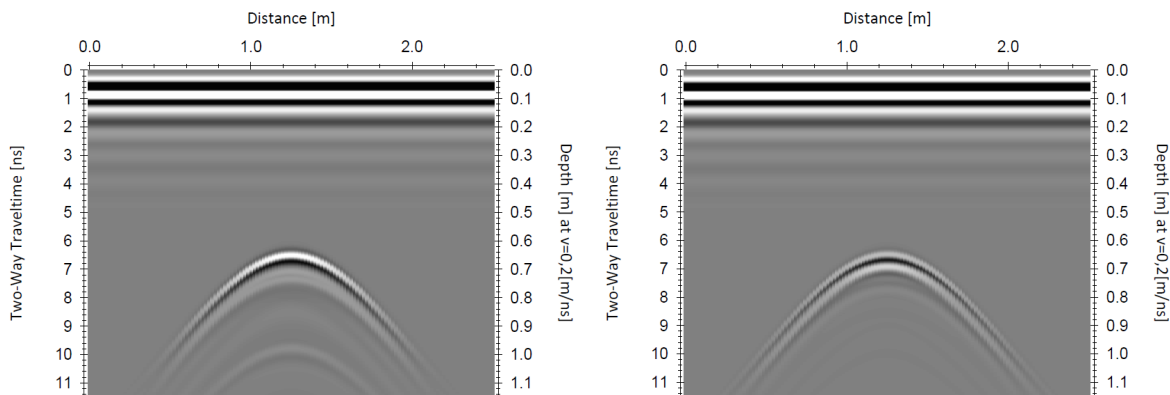


Figure B-2: Broadside-Perpendicular (left) and Parallel (right), $h = 8\text{ cm}$, synthetic data.

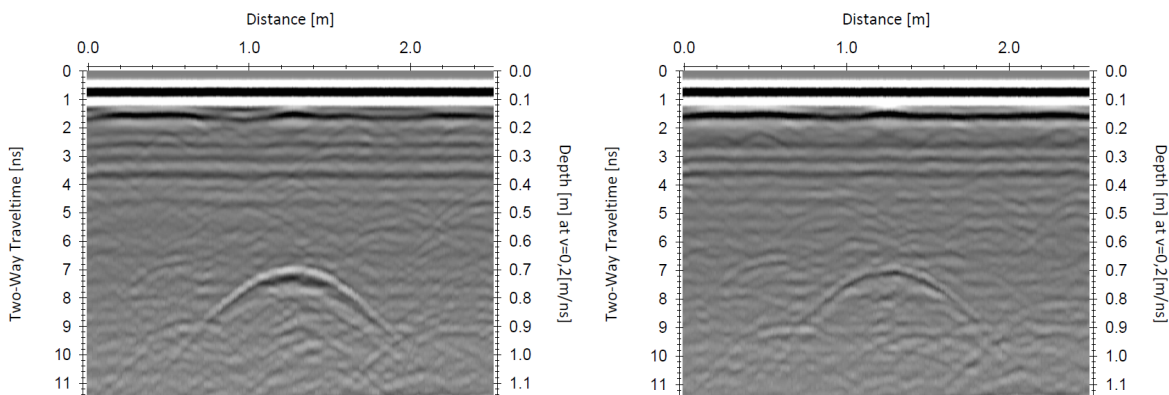


Figure B-3: Broadside-Perpendicular (left) and Parallel (right), $h = 13$ cm, field data.

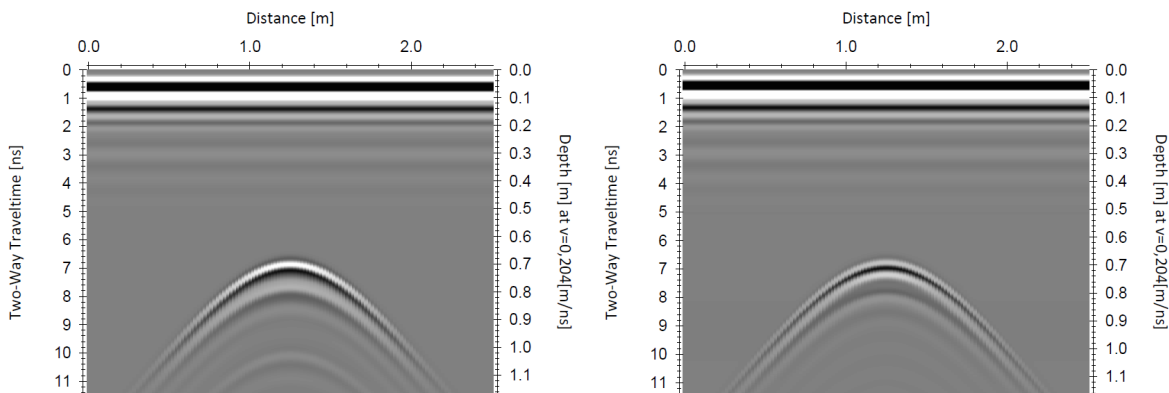


Figure B-4: Broadside-Perpendicular (left) and Parallel (right), $h = 13$ cm, synthetic data.

B-2 Inclination Measurements

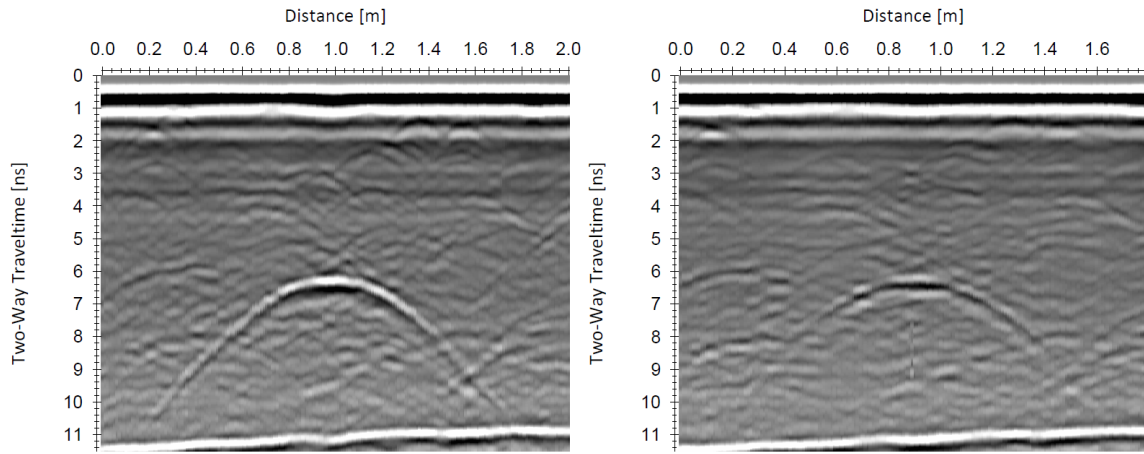


Figure B-5: Broadside-Perpendicular (left) and Parallel (right), 15°, Crossline, field data.

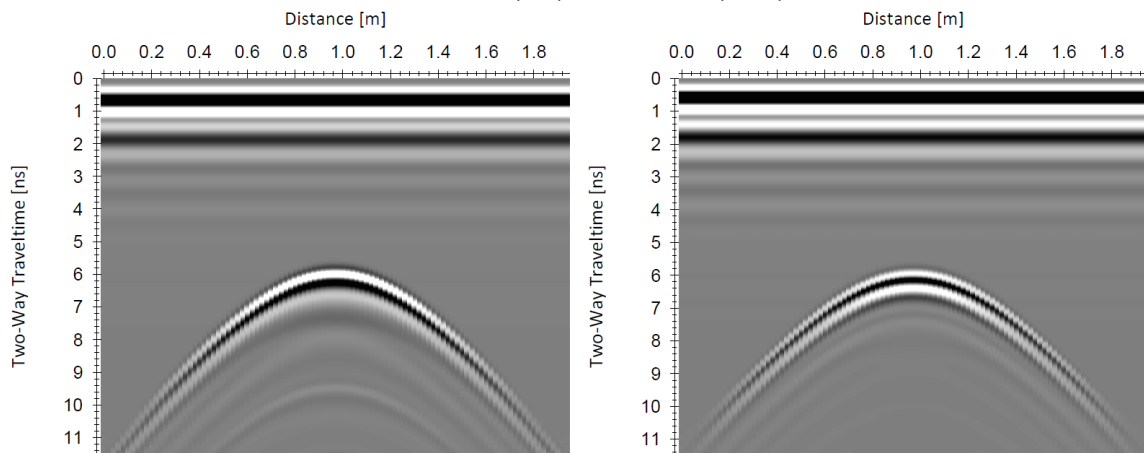


Figure B-6: Broadside-Perpendicular (left) and Parallel (right), 15°, Crossline, synthetic data.

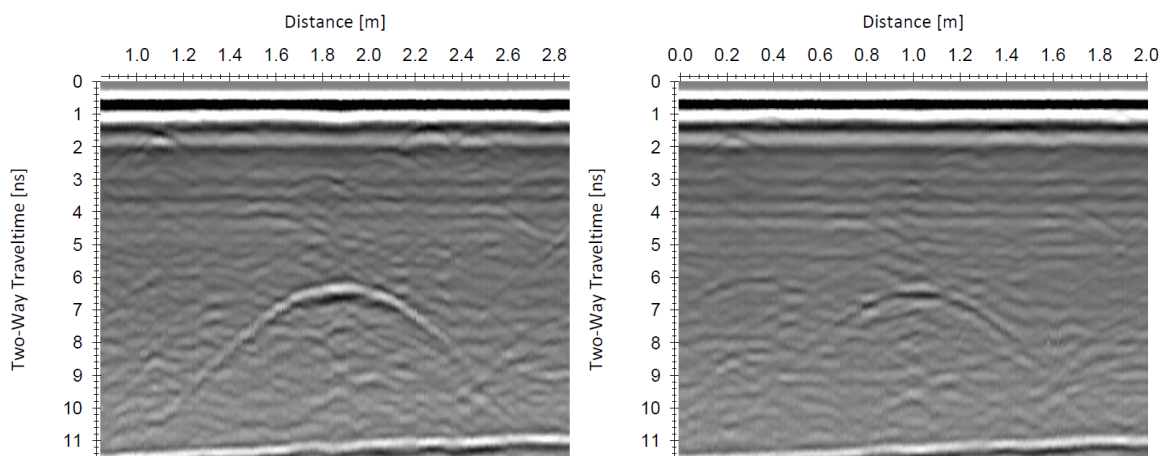


Figure B-7: Broadside-Perpendicular (left) and Parallel (right), 30° , Crossline, field data.

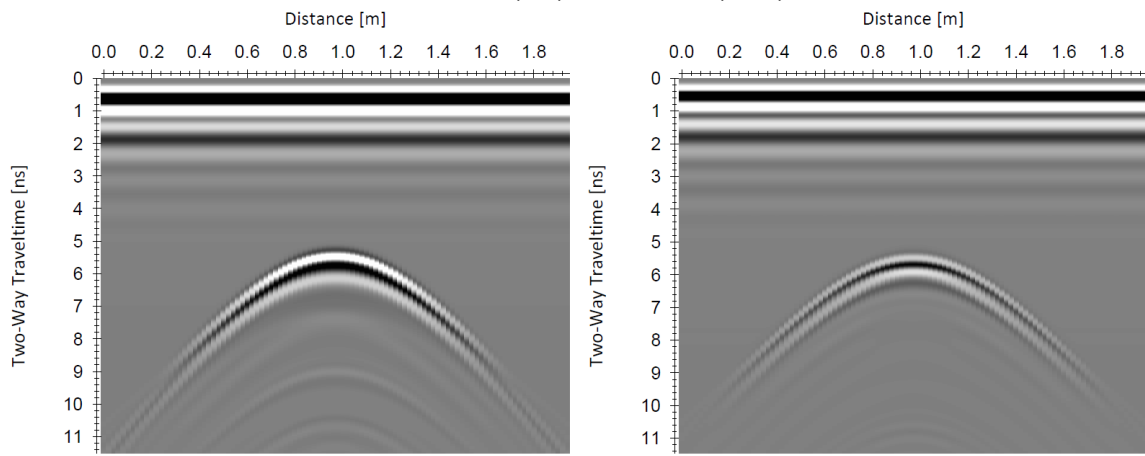


Figure B-8: Broadside-Perpendicular (left) and Parallel (right), 30° , Crossline, synthetic data.

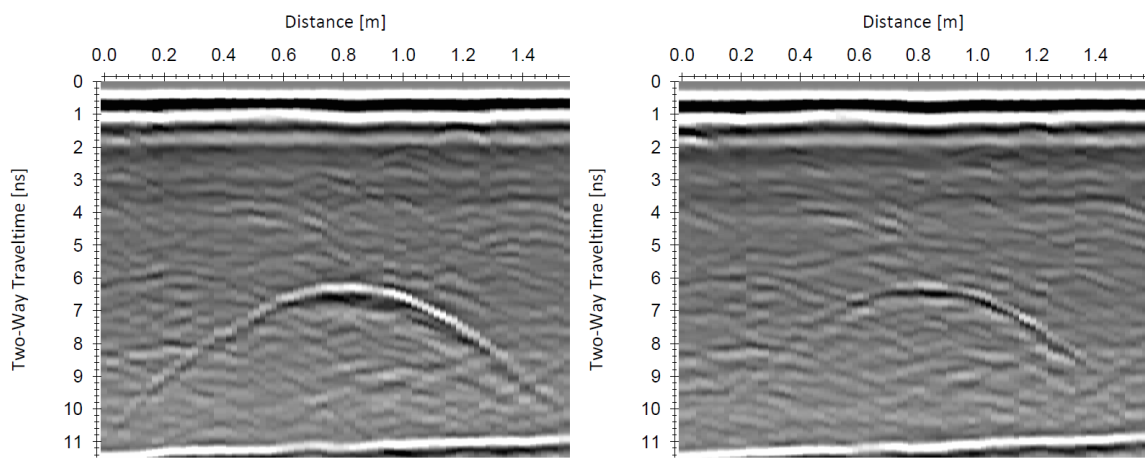


Figure B-9: Broadside-Perpendicular (left) and Parallel (right), 15° , Inline, field data.

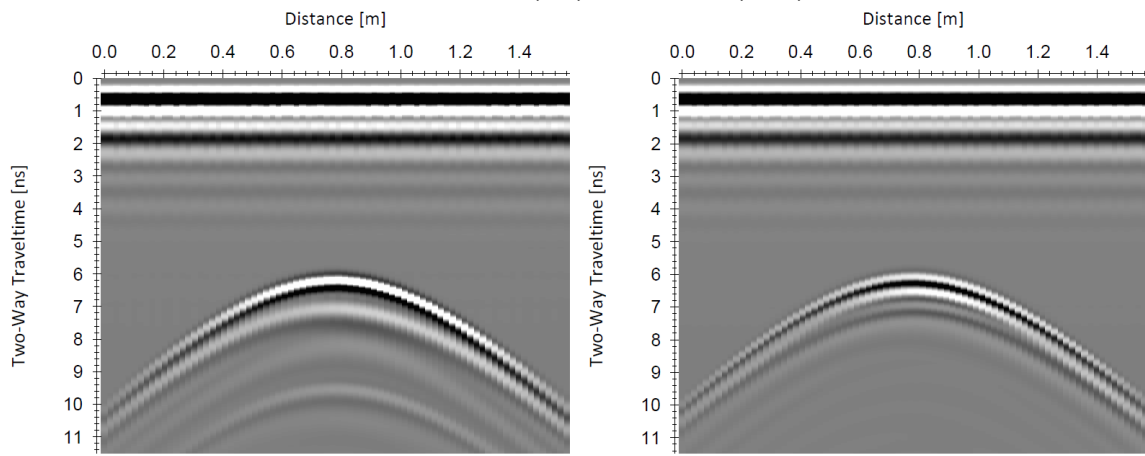


Figure B-10: Broadside-Perpendicular (left) and Parallel (right), 15° , Inline, synthetic data.

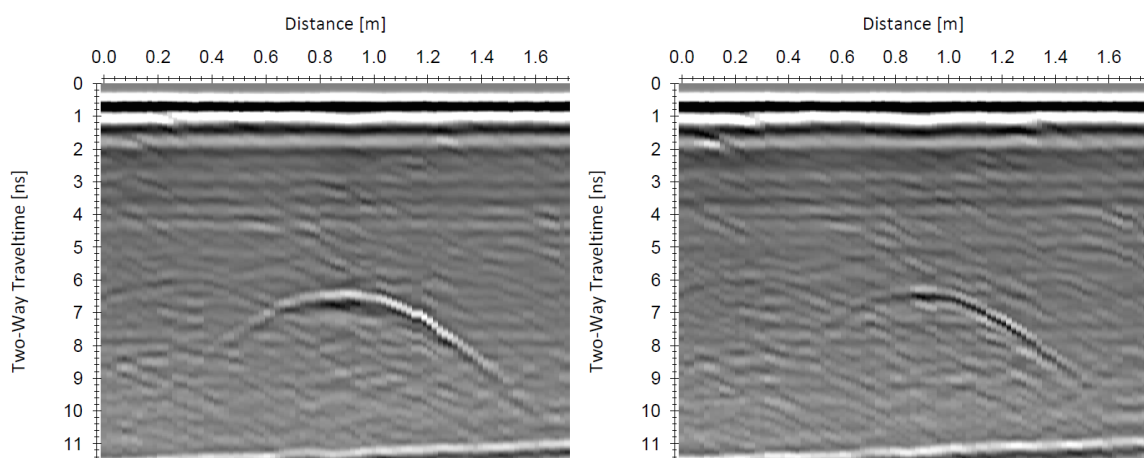


Figure B-11: Broadside-Perpendicular (left) and Parallel (right), 30° , Inline, field data.

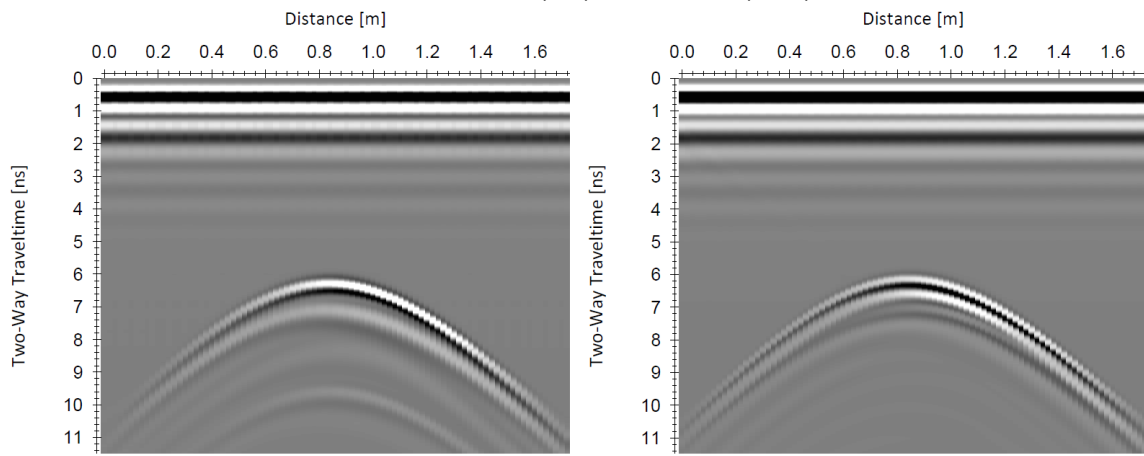


Figure B-12: Broadside-Perpendicular (left) and Parallel (right), 30° , Inline, synthetic data.

Appendix C

Envelope Plots

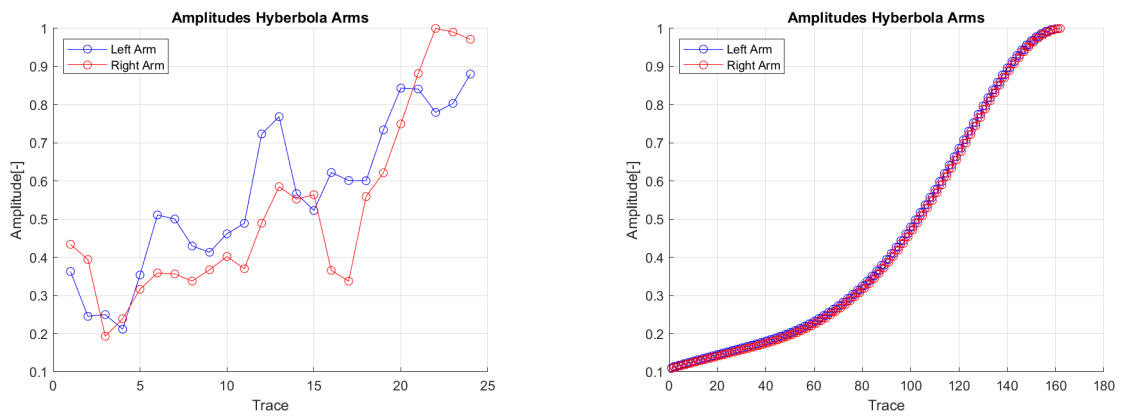


Figure C-1: Envelopes of field (left) and synthetic data (right) of the horizontal Broadside-Parallel measurements ($h = 0$ cm).

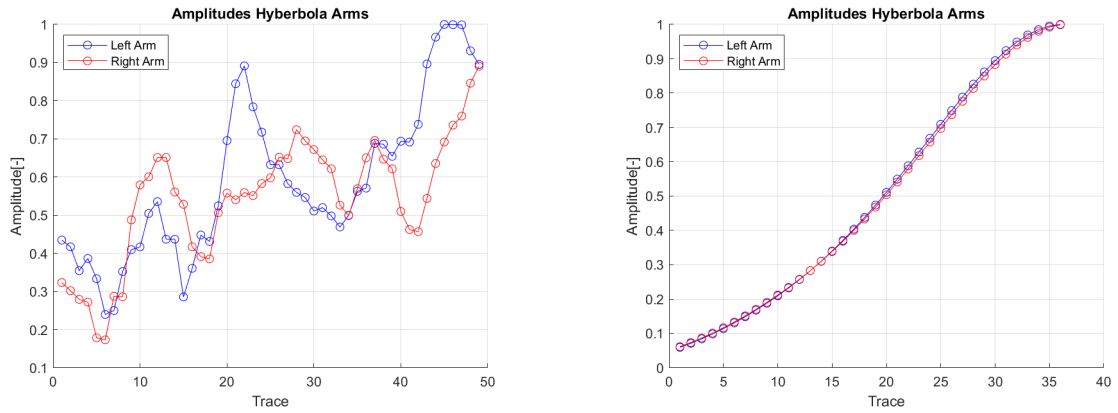


Figure C-2: Envelopes of field (left) and synthetic data (right) of the horizontal Broadside-Perpendicular measurements ($h = 8$ cm).

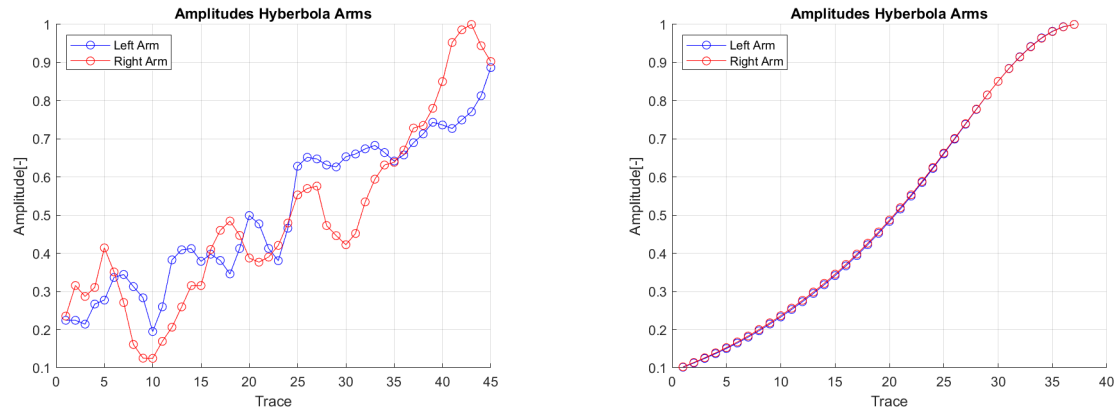


Figure C-3: Envelopes of field (left) and synthetic data (right) of the horizontal Broadside-Parallel measurements ($h = 8 \text{ cm}$).

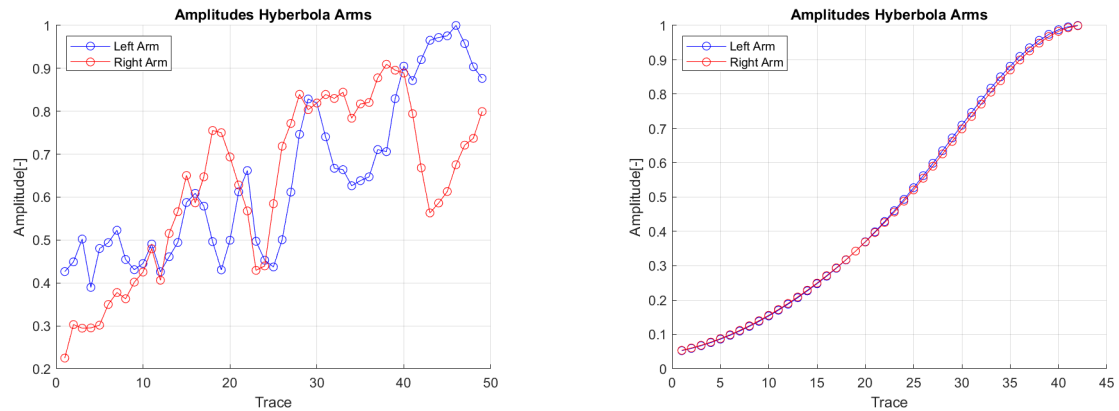


Figure C-4: Envelopes of field (left) and synthetic data (right) of the horizontal Broadside-Perpendicular measurements ($h = 13 \text{ cm}$).

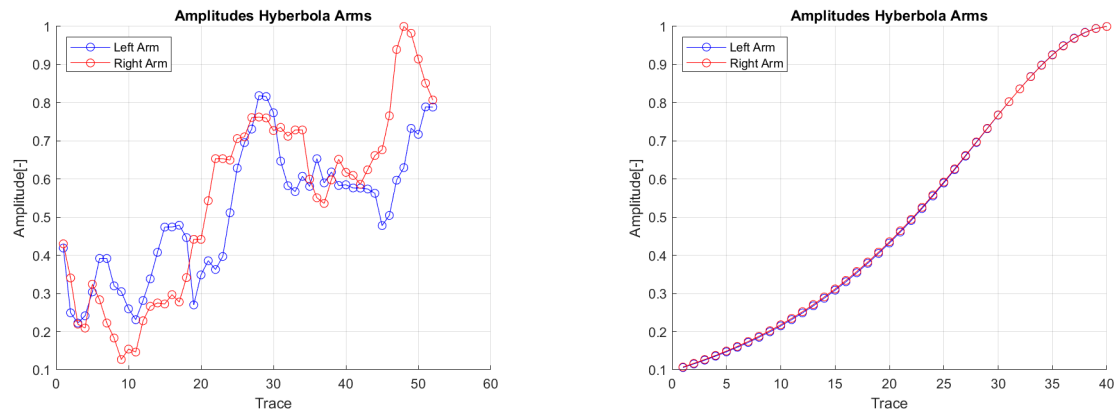


Figure C-5: Envelopes of field (left) and synthetic data (right) of the horizontal Broadside-Parallel measurements ($h = 13 \text{ cm}$).

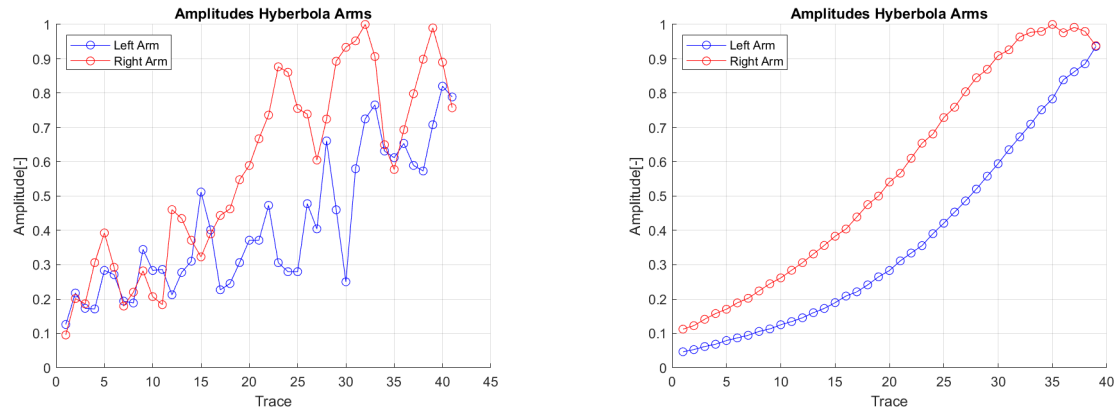


Figure C-6: Envelopes of the 15° Inline measurements (Broadside-Perpendicular), Left: Field data, Right: Synthetic data.

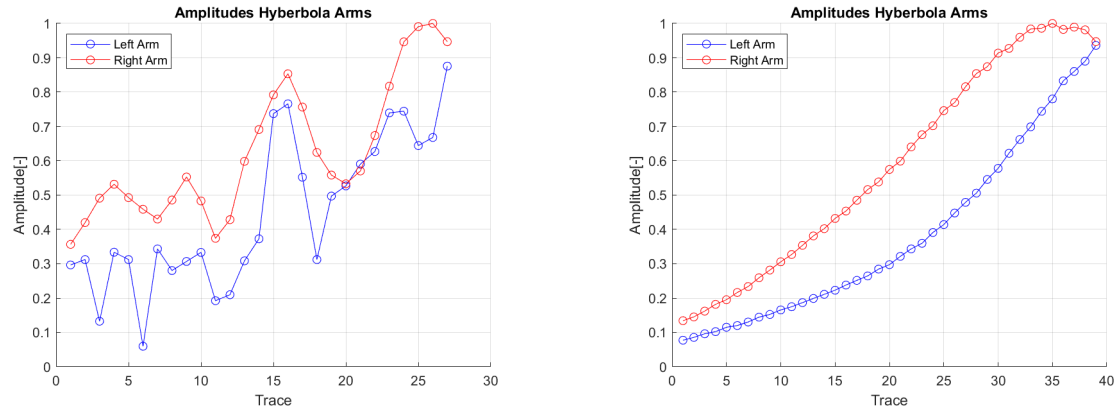


Figure C-7: Envelopes of the 15° Inline measurements (Broadside-Parallel), Left: Field data, Right: Synthetic data.

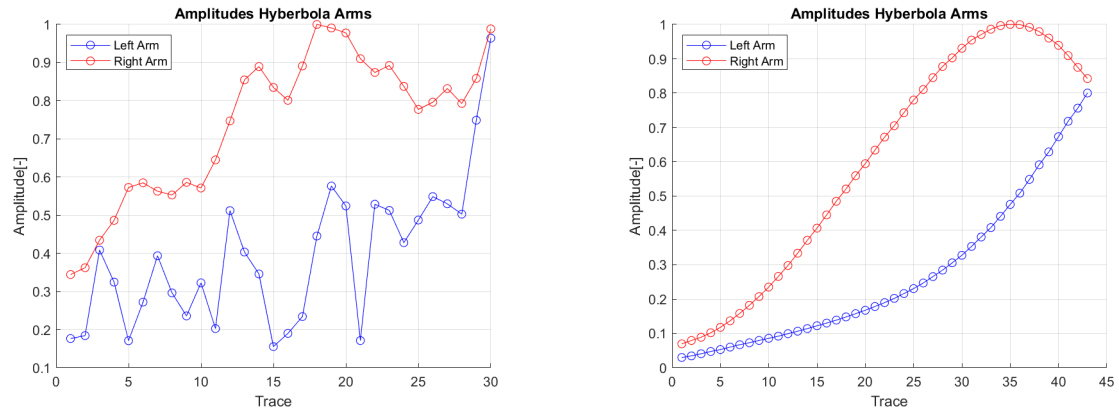


Figure C-8: Envelopes of the 30° Inline measurements (Broadside-Parallel), Left: Field data, Right: Synthetic data.

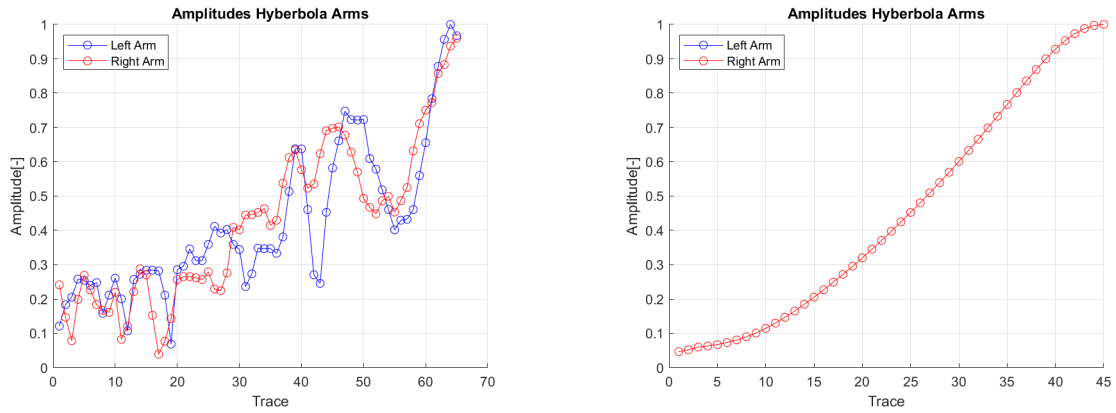


Figure C-9: Envelopes of the 15° Crossline measurements (Broadside-Perpendicular), Left: Field data, Right: Synthetic data.

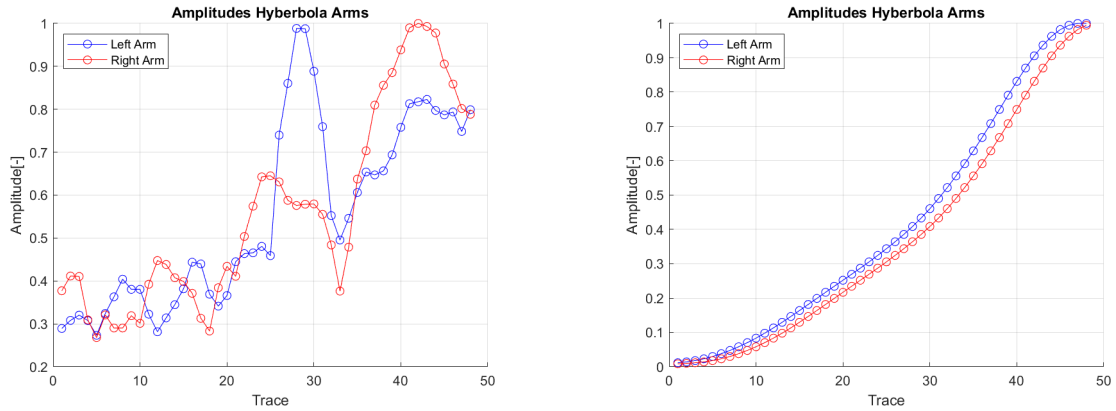


Figure C-10: Envelopes of the 15° Crossline measurements (Broadside-Parallel), Left: Field data, Right: Synthetic data.

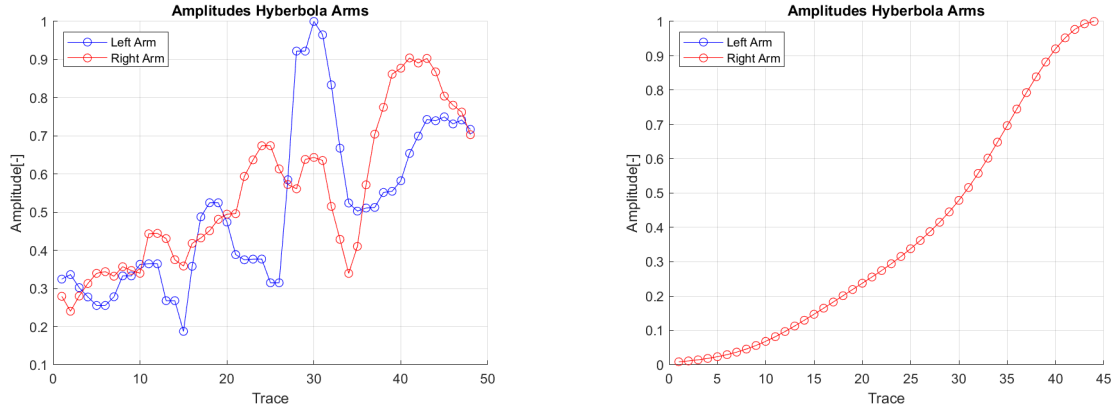


Figure C-11: Envelopes of the 30° Crossline measurements (Broadside-Parallel), Left: Field data, Right: Synthetic data.

Appendix D

Cross-Correlation Plots

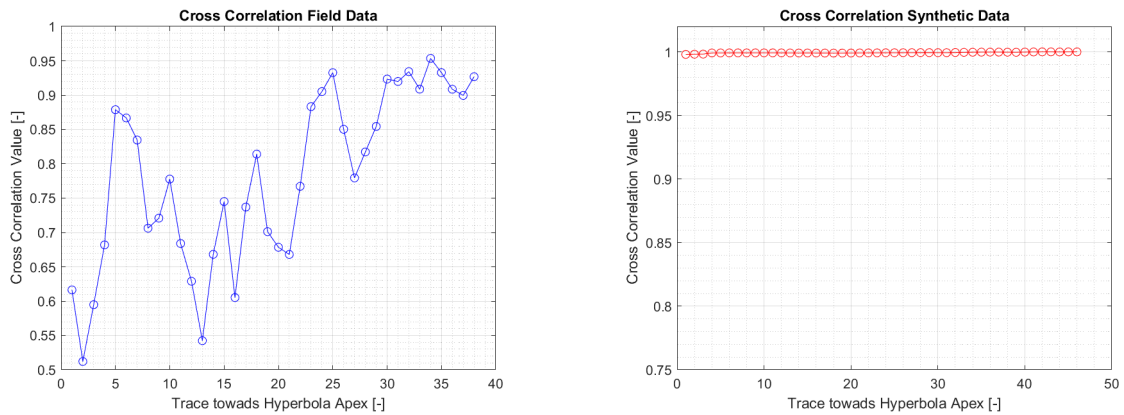


Figure D-1: Cross-Correlations, horizontal measurement ($h = 0\text{cm}$), Broadside-Perpendicular,
Left: Field data, Right: Synthetic data.

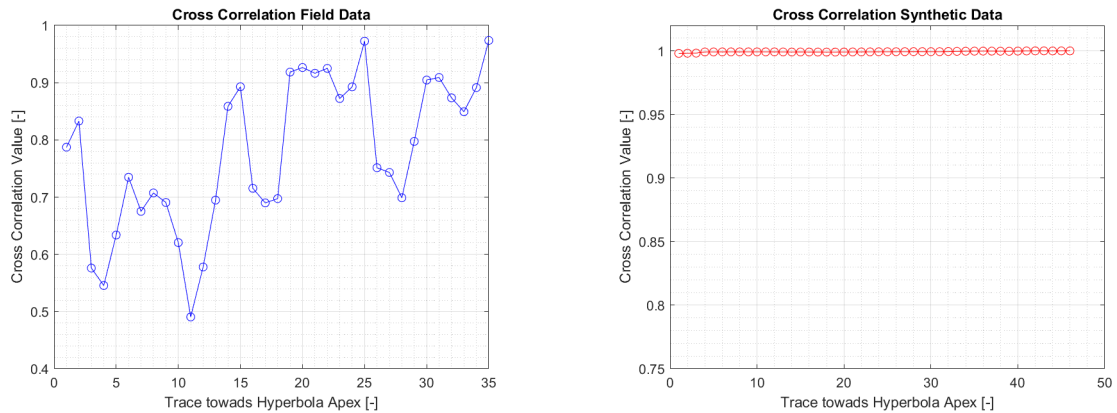


Figure D-2: Cross-Correlations, horizontal Measurement ($h = 0 \text{ cm}$), Broadside-Parallel, Left:
Field data, Right: Synthetic data.

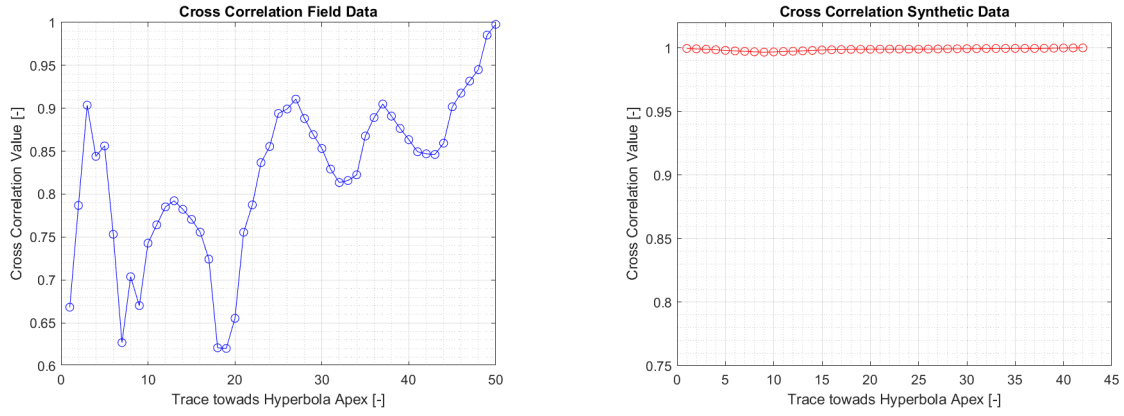


Figure D-3: Cross-Correlations, horizontal measurement ($h = 8 \text{ cm}$), Broadside-Perpendicular,
Left: Field data, Right: Synthetic data.

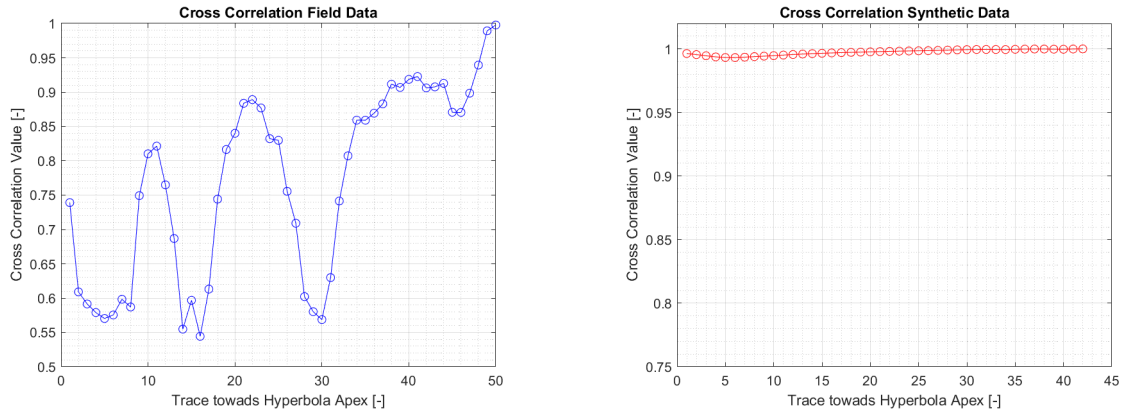


Figure D-4: Cross-Correlations, horizontal measurement ($h = 8 \text{ cm}$), Broadside-Parallel, Left:
Field data, Right: Synthetic data.

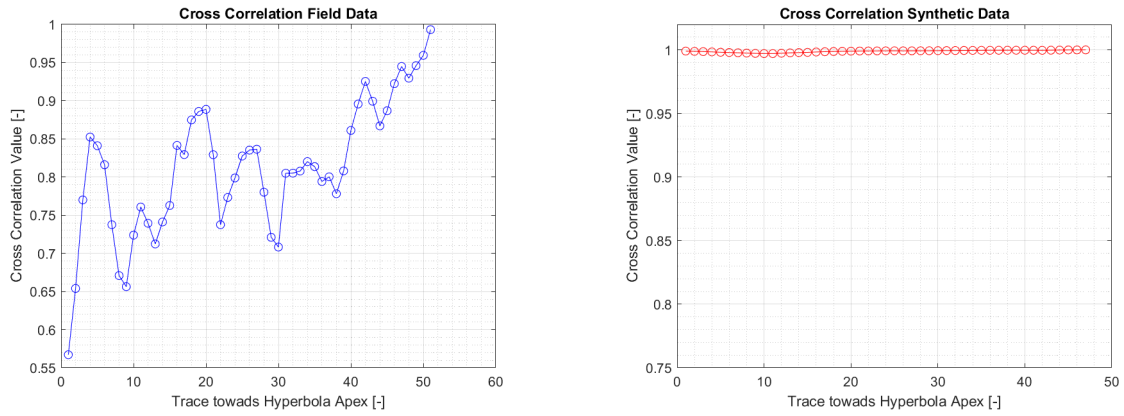


Figure D-5: Cross-Correlations, horizontal measurement ($h = 13 \text{ cm}$), Broadside-Perpendicular,
Left: Field data, Right: Synthetic data.

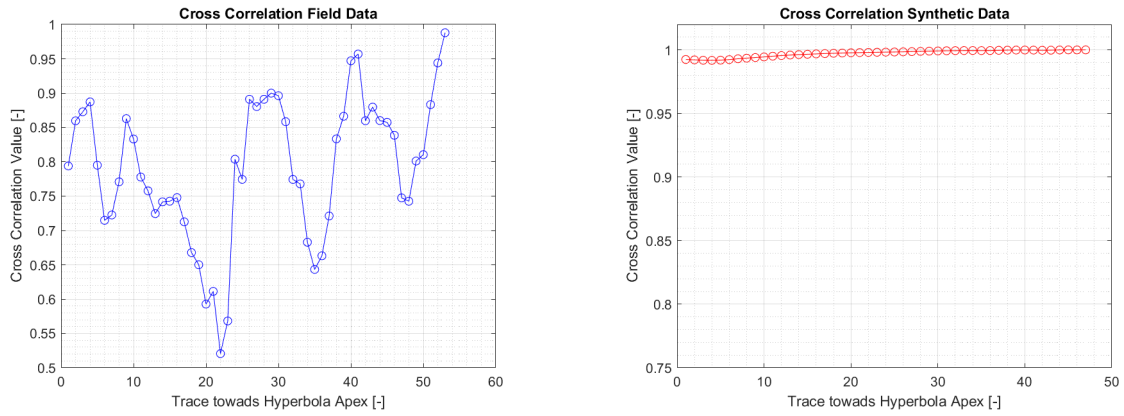


Figure D-6: Cross-Correlations, horizontal measurement ($h = 13 \text{ cm}$), Broadside-Parallel, Left: Field data, Right: Synthetic data.

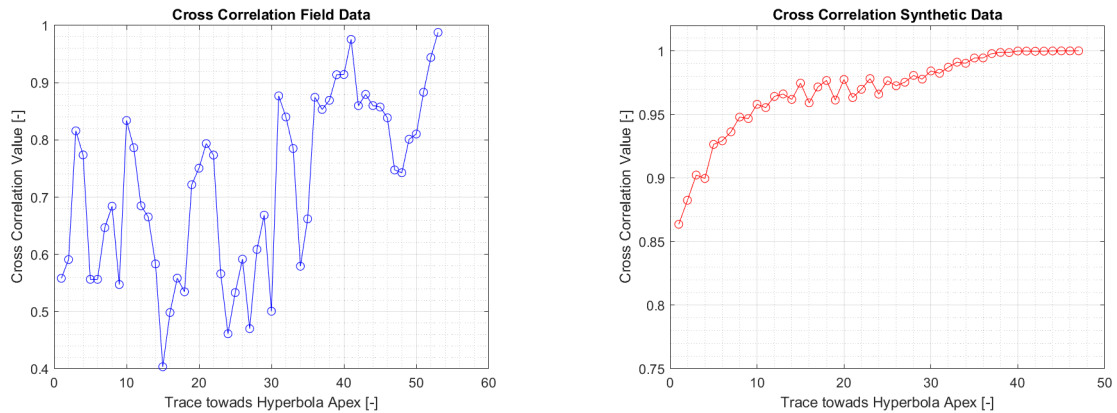


Figure D-7: Cross-Correlation, Inclination: 15° Inline, Broadside-Perpendicular, Left: Field data, Right: Synthetic data.

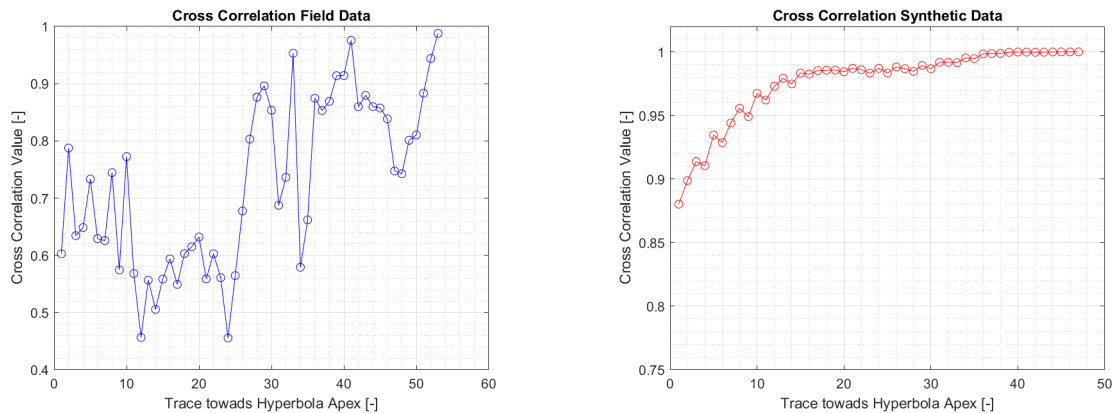


Figure D-8: Cross-Correlation, Inclination: 15° Inline, Broadside-Parallel, Left: Field data, Right: Synthetic data.

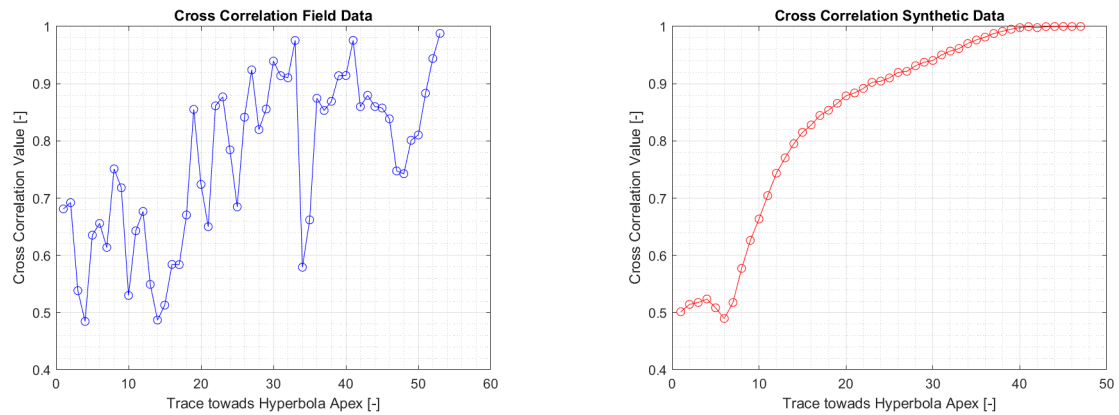


Figure D-9: Cross-Correlation, Inclination: 30° Inline, Broadside-Perpendicular, Left: Field data, Right: Synthetic data.

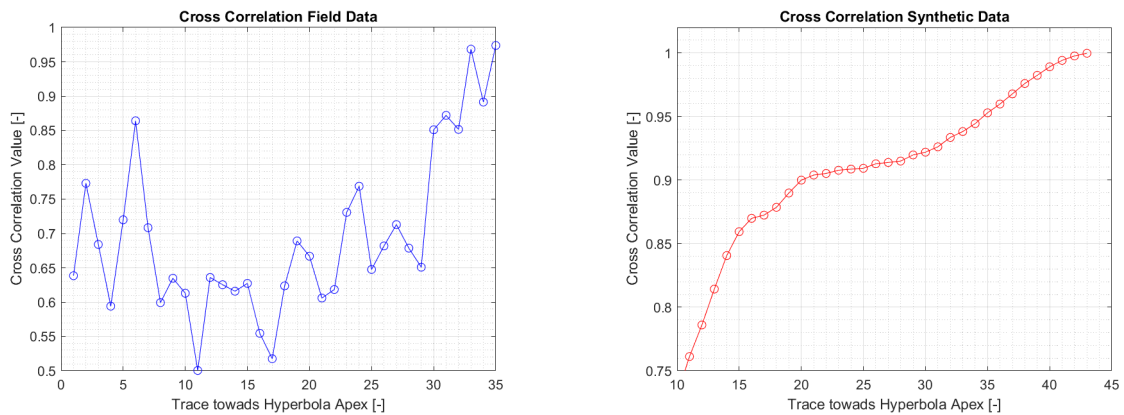


Figure D-10: Cross-Correlation, Inclination: 30° Inline, Broadside-Parallel, Left: Field data, Right: Synthetic data.

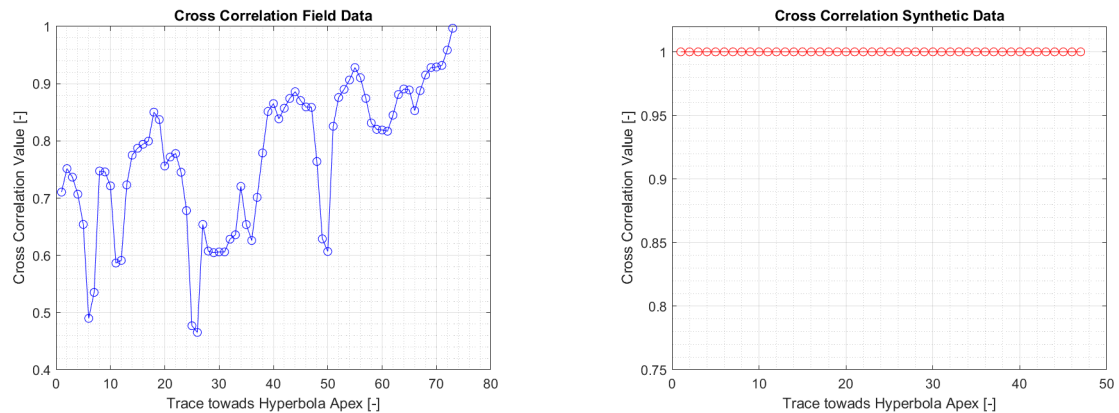


Figure D-11: Cross-Correlation, Inclination: 15° Crossline, Broadside-Perpendicular, Left: Field data, Right: Synthetic data.

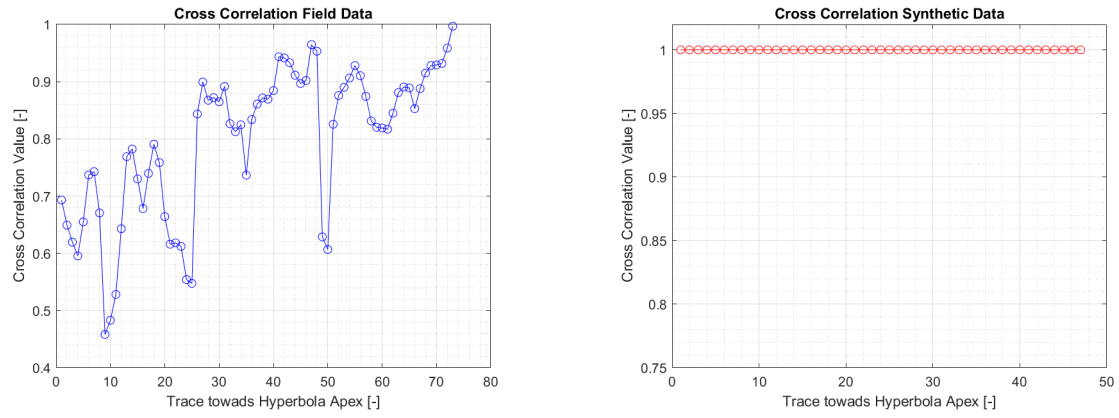


Figure D-12: Cross-Correlation, Inclination: 15° Crossline, Broadside-Parallel, Left: Field data, Right: Synthetic data.

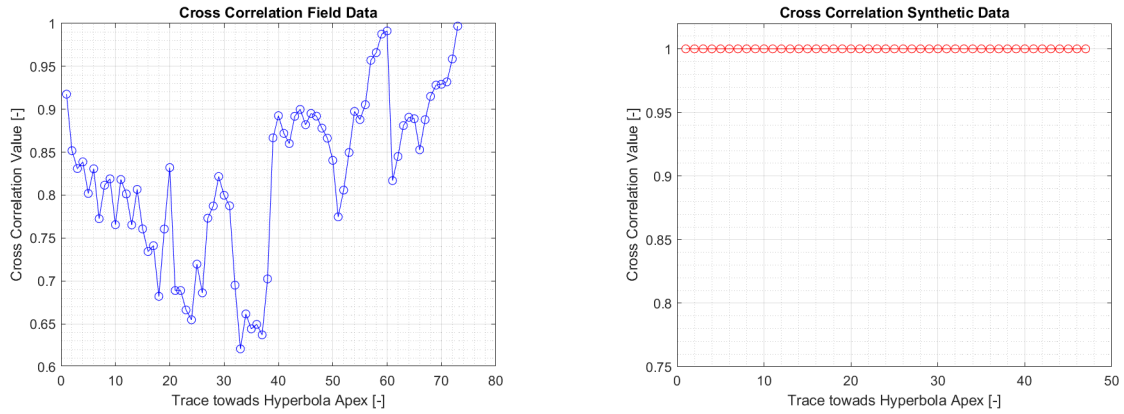


Figure D-13: Cross-Correlation, Inclination: 30° Crossline, Broadside-Perpendicular, Left: Field data, Right: Synthetic data.

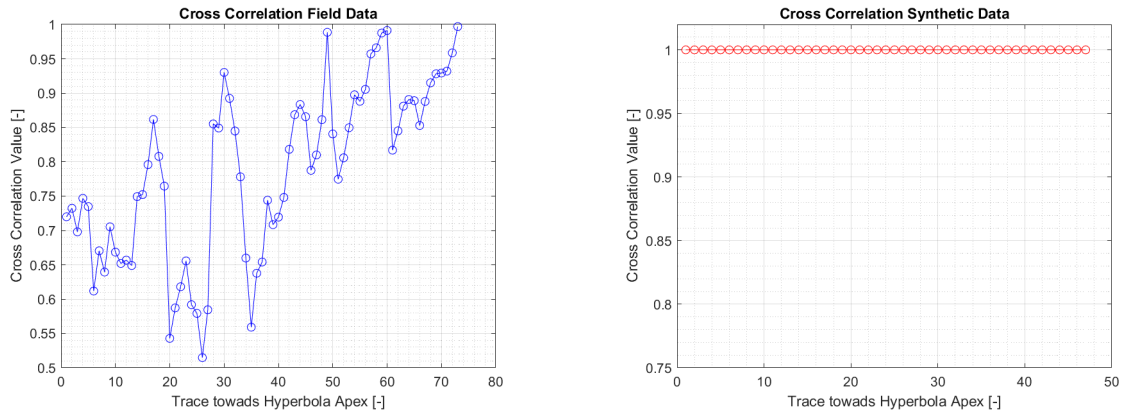


Figure D-14: Cross-Correlation, Inclination: 30° Crossline, Broadside-Parallel, Left: Field data, Right: Synthetic data.

Appendix E

Field Setup and Data Processing

E-1 ReflexW Processing Flowchart



Figure E-1: Flowchart of the general GPR data processing steps for field and synthetic data.

E-2 Photos of Field Measurements



Figure E-2: Photo of the air measurements field setup.



Figure E-3: Photo of the air measurements field setup.

Appendix F

Additional Facts about Explosive Devises

The terminology of explosives is very wide. The huge array of explosive devices made it necessary to discriminate explosive weapons commonly used in armed conflicts. However, many terms are often used analogously next to each other which can be very confusing. To clear up potential confusions, the most relevant terms of explosives are explained in this Chapter. Landmines and [IEDs](#) are specially addressed due to their increased significance for [EOD](#) operations in recent conflict areas.

F-1 Unexploded Ordnance (UXO) and Explosive Remnants of War (ERW)

[UXO](#) is one of the most commonly terms used to describe explosive ordnance which is in focus of [EOD](#). The term refers to munitions that were designed to explode but failed to detonate. A term which incorporates a wider group of explosives is [ERW](#) which incorporates [UXO](#) as well as abandoned explosive ordnance [[ICBL-CMC, 2020](#)]. For example, aircraft bombs which are still commonly found in Europa as a consequence of widespread bombing campaigns fall under the classification of [ERW](#). Landmines however are explicitly excluded from the definition. Nonetheless, landmines resemble a major part of explosive ordnance used in conflict areas. Therefore, landmines are specially addressed in the following section.

F-2 Landmines

Landmines are a wide array of explosive devices which are positioned underground designed to destroy and disable enemy targets. They are easy to manufacture and easy to deploy [[ICBL-CMC, 2019](#)]. One of the main functions of landmines is to deny access to strategically crucial infrastructures such as roads or bridges [[Hussein and Waller, 2000](#)]. Landmines



Figure F-1: Explosive Remnants of War in post revolution Libya [Foounen, 2018].

are often not removed after a conflict [ICBL-CMC, 2019]. All types of mines consist of an explosive, detonator, spring, casing and void. TNT, Tetryl and Comp B are the common explosives in anti-personnel mines [Hussein and Waller, 2000]. Landmines can have different types of trigger mechanisms. Generally, they are triggered by pressure (e.g. driving over or stepping on them) or by handling/disturbing [Kasban et al., 2010]. They usually contain several metal parts. However, there are also landmines with minimal to no metal at all [Takahashi et al., 2011]. Landmines come in different shapes and sizes.

There are two classes of landmines, namely antipersonnel and antivehicle mines. Antipersonnel mines are designed to explode from contact to a person. Antivehicle mines in comparison are larger contain more explosives. They are designed to damage and destroy armored vehicles [ICBL-CMC, 2019]. Normally, antivehicle mines are bigger in size (20-50 cm) compared to antipersonnel mines (6-20 cm). Moreover, they are triggered under higher operating pressure. The material used for landmine construction can vary significantly. There are mines made of wood, metal and plastic [Kasban et al., 2010]. The burial depth has a relationship with the operating pressure. Antivehicle mines are usually buried at a depth of up to 30 cm. Antipersonnel mines are normally buried shallower [Hussein and Waller, 2000].



Figure F-1: Left: Yugoslavian PMA-2 landmine with low metal content [LIAG, 2013], Right: Chinese Type 59 anti-tank mine [Smith, 2007].

F-3 Improvised Explosive Devices (IED)

An [IED](#) is a device placed or produced in an improvised manner. The improvised character of [IEDs](#) is reflected in its huge variety of designs. The composition of an [IED](#) heavily depends on the resources locally available. [IEDs](#) may be constructed of conventional military ordnance, such as an artillery shell, attached to a detonating mechanism. [IEDs](#) may otherwise be made with homemade explosives too. An [IED](#) has five components: an activator, an initiator, a container, a charge (explosive), and a power source (battery). [IEDs](#) are extremely diverse in design and may contain many types of initiators, detonators, and explosive loads [DHS, 2006].

An [IED](#) may be victim-activated or command-detонated. An [IED](#) is therefore not necessarily a landmine but can function as one [ICBL-CMC, 2020]. Various trigger methods are commonly used, including remote control, magnetic triggers, pressure triggers or trip wires [Mansoor, 2018]. In modern conflicts, anti-personnel [IEDs](#) have partially replaced conventional landmines as the main source of injury to pedestrian soldiers and civilians [ICBL-CMC, 2019].

[IEDs](#) are widely used by paramilitary groups in asymmetric unconventional warfare, e.g. by insurgents or guerrillas [Mansoor, 2018]. In the second Iraq War, as well as in Afghanistan, insurgents used [IEDs](#) extensively against U.S.-led forces. Between 2001 and 2007, they have caused over 60 % of all American combat casualties in Iraq and 50% of combat casualties in Afghanistan [Wilson, 2007].



Figure F-2: Typical metallic and non-metallic IEDs [LIAG, 2021]